Observations of shear flows in high-energy-density plasmas

by

Eric C. Harding

A dissertation submitted in partial fulfillment
of the requirements for the degree of
Doctor of Philosophy
(Applied Physics)
in The University of Michigan
2010

Doctoral Committee:

Professor R. Paul Drake, Chair
Professor Werner J A Dahm
Professor Robert Krasny
Professor Georg A Raithel
Research Scientist Bruce A Fryxell

ACKNOWLEDGEMENTS

I would first like to thank my advisor Professor Paul Drake for guiding me through this research. Paul has been my advisor since I was a Freshman in the undergraduate engineering program at the University of Michigan. It was with Paul's generous support that I was able to attend conferences and spend several summers in Washington, D.C. carrying out experiments on the Nike laser. I would also like to thank my parents Gary and Jeanne Harding for their unwavering support from the very beginning. And finally, I must thank my wife Erika for looking after me and putting up with me while I pretended to work hard.

TABLE OF CONTENTS

LIST OF FIGURES

Figure

LIST OF APPENDICES

Appendix

ABSTRACT

Observations of shear flows in high-energy-density plasmas

by

Eric C. Harding

Chair: R. Paul Drake

The research discussed in this thesis represents work toward the demonstration of experimental designs for creating a Kelvin-Helmholtz (KH) unstable shear layer in a high-energy-density (HED) plasma. Such plasmas are formed by irradiating materials with several kilo-Joules of laser light over a few nanoseconds, and are defined as having an internal pressure greater than one-million atmospheres. Similar plasmas exist in laboratory fusion experiments and in the astrophysical environment. The KH instability is a fundamental fluid instability that arises when strong velocity gradients exist at the interface between two fluids. The KH instability is important because it drives the mixing of fluids and initiates the transition to turbulence in the flow. Until now, the evolution of the KH instability has remained relatively unexplored in the HED regime. This thesis presents the observations and analysis of two novel experiments carried out using two separate laser facilities. The first experiment used 1.4 kJ from the Nike laser to generate a supersonic flow of Al plasma over a low-density, rippled foam surface. The Al flow interacted with the foam and created distinct features that resulted from compressible effects. In this experiment there is little evidence of the KH instability. Nevertheless, this experimental design has

perhaps pioneered a new method for generating a supersonic shear flow that has the potential to produce the KH instability if more laser energy is applied. The second experiment was performed on the Omega laser. In this case 4.3 kJ of laser energy drove a blast wave along a rippled foam/plastic interface. In response to the vorticity deposited and the shear flow established by the blast wave, the interface rolls up into large vorticies characteristic of the KH instability. The Omega experiment was the first HED experiment to capture the evolution of the KH instability.

CHAPTER I

Introduction to Laboratory Fusion and High-Energy-Density Plasmas

1.1 Introduction

High-energy lasers and intense x-ray sources can create micro-implosions in the laboratory that compress and heat a few milli-grams of hydrogen to the point where nuclear fusion occurs [1, 2, 3]. During fusion two atomic nuclei combine and release energy in the form of energetic particles. Unlike fusion in thermonuclear weapons, laboratory fusion is not driven by fission reactions, and generates a relatively small explosive impulse due to the small amount of debris mass. In experiments to date the total output energy of the fusion reactions has been much less than the input energy required to drive the implosion. Nevertheless, current research indicates that the output energy could greatly exceed the input energy (i.e., an overall energy gain much greater than one) by driving the compression of the fuel with increased energy from bigger lasers and x-ray sources [4, 5, 6]. When this occurs, it is said that "ignition" of the hydrogen fuel will have occurred, and an essential milestone for fusion research will have been reached.

The pursuit of laboratory fusion is motivated by the need to develop a clean electrical power source and to understand the detailed physics of thermonuclear weapons.

Because the physical detonation of a nuclear weapon is no longer permitted in the United States under the Comprehensive Nuclear-Test-Ban Treaty [7], observations of laboratory fusion can help validate computer simulations that attempt to accurately calculate a full-scale detonation. The majority of fusion research has been motivated by the need to develop advanced predictive capabilities in order to better understand the nation's aging nuclear stockpile and those of other countries. In addition, there is hope that further advancements in laboratory fusion could ultimately lead to the development of a fusion power plant that would provide electrical power much like a conventional coal power plant. However, instead of burning fossil fuels, these plants would fuse hydrogen leading to the production of high-energy neutrons that subsequently generate steam, which powers a turbine. Unlike coal or fission plants, fusion power plants promise to produce few harmful by-products. Yet there remain many technological challenges to overcome before a fusion power plant can be built. In particular, robust high-repetition rate (around 1 to 10 Hz) lasers are required elements in many proposed fusion power plant designs.

Currently one of the most promising techniques to achieve high gain laboratory fusion involves the implosion of a small, millimeter-sized spherical capsule by direct irradiation with laser light or x-rays. The x-rays can be produced with a laser by irradiating a metal such as gold. The concept of compressing a capsule with an intense laser was first published by John Nuckolls in 1972 [8]. While there are numerous designs, a typical capsule will consist of one or more layers of material, known as an "ablator", that coat a hollow spherical shell of cryogenic Deuterium and Tritium (hydrogen isotopes whose combination is referred to as "DT") ice with an internal DT gas core (see Figure 1.1). When intense laser or x-ray radiation is applied to the capsule the outer layer of the ablator vaporizes (i.e., turns into a hot, ionized gas known as a plasma) and rapidly expands outward causing the capsule to recoil inwards. The implosion of the capsule works to compress the gas at the center of the

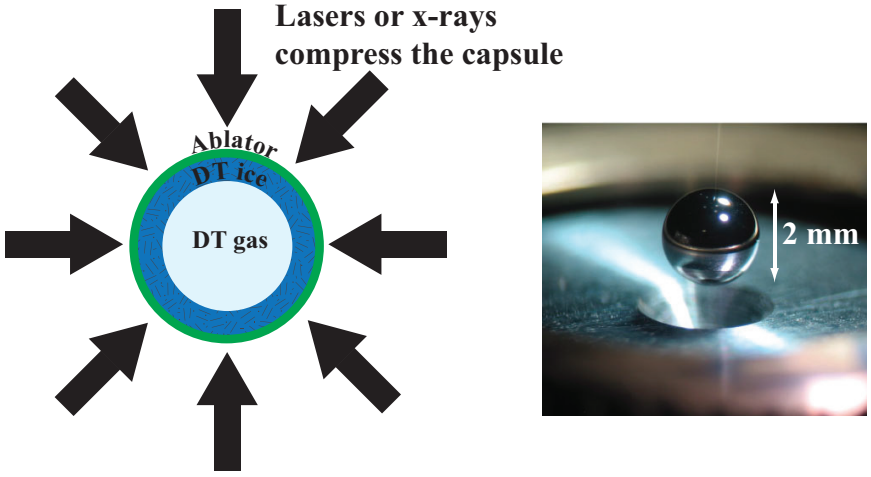

Figure 1.1: Shown here on the left is a cross-section of a typical fuel capsule used for laboratory fusion experiments. The applied laser or x-ray radiation drives the implosion by vaporizing the outer most layer of the capsule. The picture on the right shows a capsule in the final stages of fabrication. This particular design uses a highly polished Beryllium ablator. The capsule is filled with DT fuel through a tiny 10 μm diameter tube, which can be seen as a faint vertical line extending from the top of the capsule.

capsule to high enough temperatures (around 100 million Kelvin) and densities that fusion can begin. The fusion initiated in the gas provides a spark that is intended to ignite the surrounding DT ice leading to a self-sustaining burn wave. During the fusion burn, the inertia of the imploded DT ice works to confine the fusion process. Hence, this technique is referred to as inertial confinement fusion (ICF). This contrasts with another approach called magnetic confinement fusion (MCF) that uses magnetic fields to confine a slower-burning and lower-density hydrogen fuel. Although MCF also appears to be a promising technique, it will not be discussed in this thesis.

1.2 Laboratory astrophysics and high-energy-density physics

The extreme pressures and temperatures created in the ICF environment are comparable to those in many astrophysical systems such as core-collapse supernovae and the interiors of giant planets. By using the facilities intended for ICF and a cleverly designed target, the fundamental processes occurring in these systems can be investi-

gated in the laboratory [9, 10, 11]. In contrast to the phenomena occurring in space, laboratory experiments can carefully control and actively probe an evolving system with a variety of diagnostics. These experiments can be reproducible and provide data that can be quantitatively compared with astrophysical models and simulations. The ability to use fusion facilities to achieve experimental conditions that are relevant to astrophysical systems has led to the formation of a new area of research known as "high-energy-density laboratory astrophysics," which is part of "laboratory astrophysics." Previous experiments have studied supernovae hydrodynamics, high Mach number jets, collapsed radiating shocks, planetary interiors and opacities of elements found inside the Sun [12, 13, 14, 15, 16].

One of the pioneering experiments of laboratory astrophysics explored the mixing that follows the shock wave in a core-collapse supernova. In this type of supernova the collapse begins when a massive star (defined as one with a mass greater than 8 times the mass of the Sun) can no longer fuse atomic nuclei deep within its core. Once the outward pressure due to fusion energy stops the star collapses inward under its own weight. A result of this collapse is that most of the stellar material explodes outward. During this process, observations show that some inner material is thrust rapidly outward, so that in some sense the star turns itself inside out. Just how this happens is not known. There has been particular interest in this subject after astronomers discovered that observations of the recent supernova 1987A did not agree with modern computer models. However, there is little doubt that the shock induced mixing of the different elemental layers of the star is an important component of the overall dynamics. In order to better understand this mixing a laboratory experiment was designed to study the unstable mixing layer created in the outer helium and hydrogen layers of a supernova. The mixing in these layers can be modeled in the terrestrial laboratory due to the scale-invariance of the equations that govern the hydrodynamics. If the experiment is carefully designed so that the initial conditions

and certain non-dimensional quantities are similar to those of the supernova, then the mixing in the laboratory experiment will mimic the supernova mixing despite their enormous size differences. One such non-dimensional quantity is the Reynolds number, which is the ratio of the inertial forces and the viscous forces in a fluid flow. Supernovae have Reynolds numbers around 10^{10} while the laboratory experiment is around 10^5. Even though these estimates are five orders of magnitude different, the laboratory value is large enough such that viscous effects can be neglected. Figure 1.2a shows a full scale supernova simulation taken from Ref. [17]. It is important to note that the explosion is not spherically symmetric and that there is mixing of the heavy and light elements. This is expected to affect Earth based observations of the electromagnetic spectrum emitted from the heavy elements. Figure 1.2b shows an image of a scaled supernova experiment taken from Ref. [18].

Other laboratory experiments achieve similarity with their astrophysical counterpart without any scaling or transformation of the dependent parameters. The densities, pressures, and temperatures are similar to those in the astrophysical systems. For example, hydrogen can be compressed in the laboratory to pressures and densities that exist near the core of Jupiter [15]. Likewise, carbon can be compressed to a state thought to exist in the cores of Neptune and Uranus [19]. In another experiment, iron was heated to the same temperature and ionization state as the iron in the Sun [16]. The transparency of the Sun's iron to the radiation originating from its core is an important input into models that attempt to recreate the internal structure of the Sun. These laboratory experiments can only briefly maintain these extreme conditions, but they exist long enough to be accurately diagnosed. The measurements are then used to determine the detailed properties of matter in order to build a complete physical picture of the astrophysical system.

In general the investigation of plasmas with pressures greater than a megabar (one-million atmospheres), or equivalently an energy density of 10^{11} J/m^3, has been

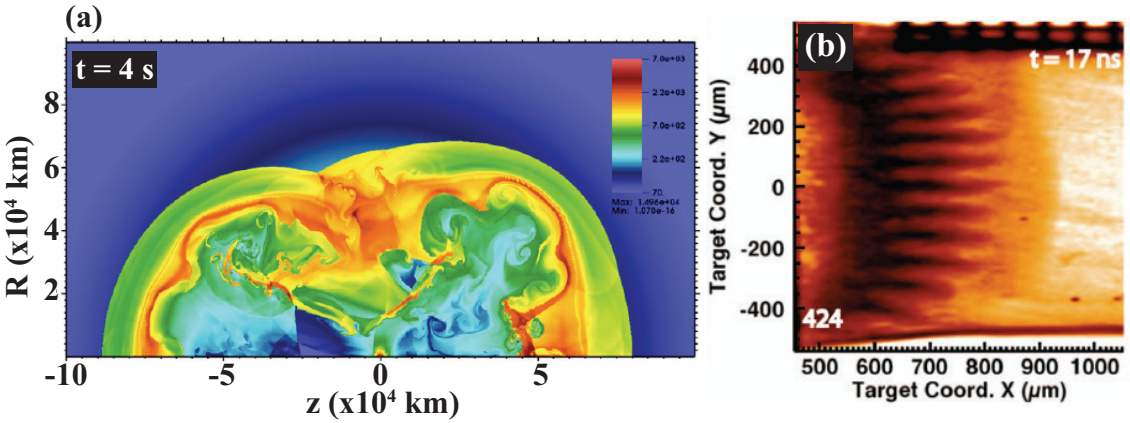

Figure 1.2: (a) Shown here is the density distribution of a full-scale core-collapse supernova simulation taken from Ref. [17]. The simulation is shown 4 s after the explosion of a 15 solar mass, blue supergiant star that modeled the progenitor star of supernova 1987A. The supernova shock front can be seen as a sharp boundary near the outer edges of the image. Deeper into the supernova a dense band of ejecta from several heavy elements (mainly oxygen, silicon, and nickel) is seen mixing with the surrounding material. (b) The image shown here is a radiograph of a laboratory experiment that recreated the conditions at the helium and hydrogen interface during the passage of the supernova shock wave. In the experiment the interface was made of plastic and foam and the shock wave was driven into the plastic by irradiating it with a high-intensity laser. The dark spikes grew from small sinusoidal perturbations that were machined onto the plastic surface. This image was taken from Ref. [18].

termed "high-energy-density physics" (HEDP). Both ICF and laboratory astrophysics experiments produce plasmas of this type, and often these experiments are simply referred to as HED experiments. The HEDP regime also encompasses ultra-fast and ultra-intense laser science, both heavy ion and intense electron beam physics, and quark-gluon plasmas. Research of high-energy beams of electrons and protons is in part motivated by the need to develop compact radiation sources for medical applications such as proton beam therapy [20]. Other research is motivated by the need to better understand complex issues such as non-linear compressible hydrodynamics, radiation transport, and material equations of state in the HEDP regime.

1.3 Hydrodynamic instabilities

For ICF to be successful, a fuel capsule must be symmetrically compressed without significant breakup and deterioration of the capsule wall during the implosion. Keeping the capsule intact during the implosion is challenging because the motion of the wall naturally becomes disorganized through the development of hydrodynamic instabilities. These instabilities are born from the initial surface roughness on the various capsule materials and the non-uniformities in the laser intensity profile. If they grow too much, the hydrodynamic instabilities essentially create holes in the capsule by amplifying these material and laser imperfections. Trying to do inertial fusion with a holey capsule is analogous to trying to achieve combustion in an engine with holey pistons. In either case if the fuel is not adequately compressed before it is ignited the efficiency of the burn decreases dramatically. These instabilities will always be present at some level, but the goal is to minimize their effects to allow sufficient compression of the capsule so that fusion can occur with substantial energy gain. The work presented in this thesis is aimed at the investigation of one of these hydrodynamic instabilities known as the Kelvin-Helmholtz (KH) instability [21, 22]. In addition to KH, there are two other instabilities that go by the names Rayleigh-Taylor (RT) [23, 24] and Richtmyer-Meshkov (RM) [25, 26] that are the primary hydrodynamic instabilities that cause capsule damage [27, 4]. The KH instability typically appears as a secondary instability that can assist these other instabilities in finely mixing the different layers of the capsule [28, 29]. The KH instability is also suspected to play an important role in mixing the plasmas in many astrophysical systems such supernova and jets. While it is difficult to directly identify the KH instability in astrophysical observations, its presence is predicted by computer simulations [17, 30, 31]. Therefore, it is necessary to perform experiments to verify that the computer simulations can accurately reproduce the laboratory observations. Once validated these computer codes can then be used to simulate real astrophysical

systems with some confidence.

The KH instability can arise whenever a strong velocity gradient exists in a density stratified or homogenous fluid flow. Fluids with strong velocity gradients are called shear flows. Typically shear is generated when one fluid passes into or over another fluid, or when fluid is forced to flow along a solid boundary. Boundary layers are formed when a flow is sustained over a solid object. Although strong velocity gradients exist within boundary layers, this type of flow is not KH unstable. Boundary layers form in response to a finite viscosity, but the KH instability can exist in a fluid with no viscosity. When a shear flow exists in a fluid containing a velocity gradient that is unperturbed by external boundaries such as neighboring solid walls it is called a "free shear flow." The KH instability can only occur between two fluids, and is most commonly observed in free shear flows and jets, which are typically generated by injecting a well-collimated fluid into a relatively slow moving fluid. It is perhaps best to imagine wind blowing over a lake as one example of a free shear flow. KH like structures have been observed in granular flows, yet it is not clear whether the underlying physics is the same [32]. In any case, nearly all turbulent flows are driven by shear. In a pure KH system the instability promotes the growth of small perturbations that grow and form secondary instabilities, which ultimately help the flow transition to a fully turbulent state. Understanding this transition is fundamentally important because the properties of the flow change dramatically once turbulence is established. For example, the momentum and thermal diffusivity of a flow may increase by an order of magnitude upon the transition to turbulence.

1.3.1 Previous shear flow experiments

There have been very few HED experiments dedicated to the investigation of the KH instability. One previous attempt to produce a shear flow under HED conditions was inconclusive and did not observe KH growth [33]. Another experiment deduced

that the KH instability was responsible for the ripples observed on an aluminum plate after the surface was repeatedly struck by a laser [34]. In other experiments designed to produce the RT instability, a shear flow is generated along the interpenetrating spikes and bubbles that form along a decelerating material interface [35, 12, 36]. Here the shear works to enlarge the spike tips by stripping off material, which is subsequently rolled into vortices that resemble the KH instability. These vortices may work to decrease or increase the overall drag experienced by the spike and thereby influence its acceleration history and position [37]. These enlarged spike tips are seen in the experimental data, but are under resolved [36]. In more recent experiments with similar geometry, but different initial conditions, the tips do not appear to enlarge [18]. The absence of tip growth has lead to speculation that the material in spikes may be constrained by magnetic fields [38]. The important role of the RT instability in both ICF and astrophysical systems provides further motivation to investigate detailed shear effects in the HED regime.

Outside the HED regime, shear flows have been studied extensively in "cold", non-ionized gases and fluids with applications ranging from hypersonic combustion to large-scale ocean dynamics [39, 40, 41]. Traditional experiments have used inclined tanks of stratified fluid to initiate a flow, generally at low Reynolds numbers, or wind tunnels that combine two parallel gas flows at the end of a thin wedge, known as a splitter plate. The splitter plate experiments have explored flows with maximum shear velocities on the order of 10^3 m/s and maximum Reynolds numbers around 10^6 to 10^7. In addition, shock tube experiments involving oblique membranes separating two gases have investigated shear flow effects. Shear develops between the two gases as a result of the shock speed difference in each gas. The experimental work presented in [42, 43, 44] and simulations in [45, 46] show the development of the shear layer formed in this type of experiment. Figure 1.3 shows three examples of the different experimental configurations that can be used to generate shear layers.

The high Reynolds numbers and supersonic Mach numbers achieved in the splitter plate and shock tube experiments are similar to those obtained in the HED regime, and thus make them relevant to the study here. In the splitter plate experiments a spatial evolving shear layer is generated as shown in 1.3a. Soon after the two streams combine, the linear KH instability amplifies small perturbations at the interface. These perturbations grow exponentially as they propagate down stream and eventually begin to roll-up into large vortices at which point the dynamics are already highly non-linear. Both incompressible and compressible splitter plate experiments have been carried out. The incompressible experiments have investigated the effects of varying density and velocity ratios of the two streams on the shear layer growth [47]. The compressible experiments have combined supersonic flows to investigate the shear layer growth dependence on Mach number. It was found that the growth rate of a compressible shear layer was correlated to a new quantity known as the convective Mach number [49, 50]. This Mach number is defined in the frame of reference of the largest organized vortices that convect downstream and appear to have originated from the KH instability. The shear layer growth begins to significantly decrease at a convective Mach number around 0.5. A further decrease in growth occurs as the convective Mach number increases.

1.4 Facilities for inertial confinement fusion and high-energy-density physics

Large high-energy lasers and x-ray sources have been the primary tools for generating the high temperatures and densities relevant to ICF and HEDP. At the present time, the National Ignition Facility (NIF) at Lawrence Livermore National Laboratory is the world's largest glass laser and is producing over 1 MJ (one-million Joules) of ultra-violet laser light. The NIF facility is in position to be the first to attempt the

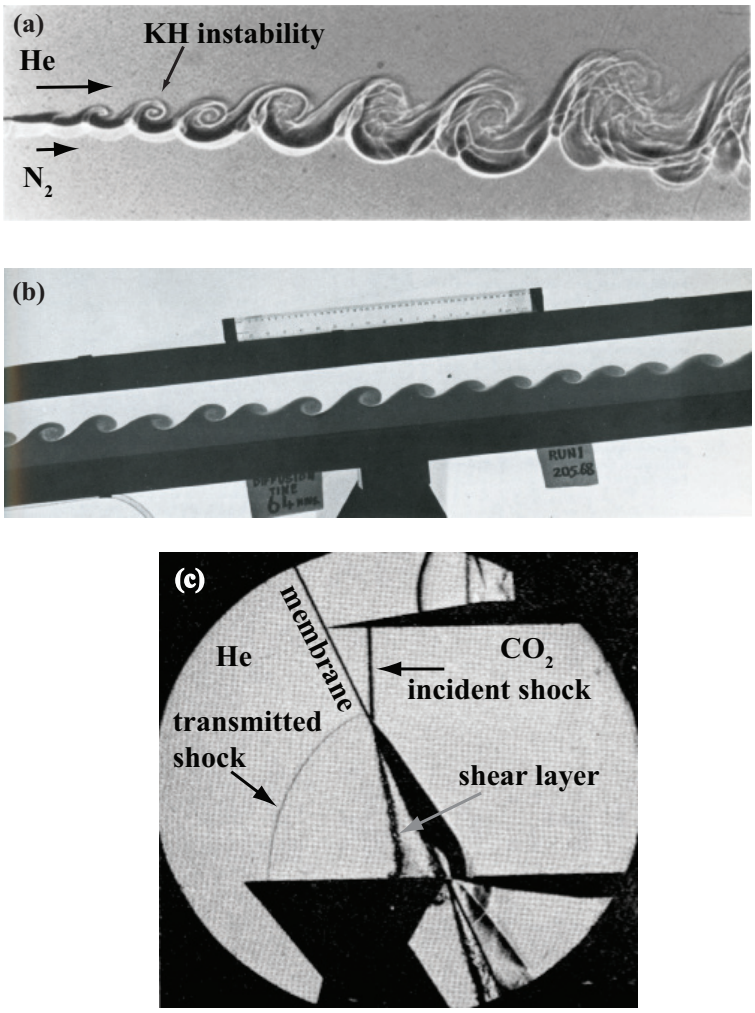

Figure 1.3: Here are examples of three different experimental configurations used to generate shear layers and the KH instability in ordinary fluids. (a) In this incompressible experiment (i.e., Mach numbers of both flows are near 0), two parallel flowing gases were merged near the end of a thin splitter plate. The KH instability developed and the flow then started a transition to turbulence. This image was taken from Brown and Roshko (1974) [47]. (b) A tank was filled with two liquids of different densities and then tilted. Like the splitter plate shown in (a), this experiment generated an incompressible flow. The fluid on the bottom was a colored brine solution while the top fluid was pure water. This image was taken from Thorpe (1971) [48]. (c) Here a shock wave crossed an oblique membrane separating He and CO_2 gases. A shear layer (known in these types of systems as a "contact discontinuity") developed due to the difference in the shock velocity in the two gases. In this image from Abd-El-Fattah (1978) [44] the shear generates a turbulent mixing layer behind the transmitted shock. The KH instability was not observed. The published data did not indicate if the shear layer was compressible, but we suspect the flow parallel to the contact discontinuity was largely incompressible.

ignition of a DT fuel capsule. Other facilities use pulsed power devices to efficiently convert a large discharge of electrical current into x-rays. The Z machine at the Sandia National Laboratory is the largest of these pulsed power devices. The Z machine channels over 20 MA (twenty-million Amperes) of electrical current into a thimble-sized array of wires, which vaporize and generate 1.8 MJ of x-rays. These x-rays take the place of laser light, and are used to compress the fuel capsule. The NIF and the Z machine are examples of some of the biggest facilities used in HEDP research. There are also many smaller facilities that contribute. Two of these smaller laser facilities, named Omega and Nike, were used to the conduct experiments presented in this thesis. A brief overview of both Omega and Nike will now be presented.

1.4.1 Omega laser

Located in Rochester, NY at the Laboratory for Laser Energetics, the Omega laser occupies an area the size of an American football field and outputs a maximum of 30 kJ of ultra-violet (UV) light when all 60 beams are fired [51]. In Figure 1.4 a computer aided image of the laser and a picture of the interior of the main chamber are shown. The Omega laser uses a combination of rod and disc amplifiers made from Nd-doped phosphate glass (Nd:glass) and pumped by flash lamps to amplify a seed pulse generated by a small fiber laser. A total of 60 beams of infrared light (wavelength = 1.054 μm) are produced, and then converted to UV light (wavelength = 0.351 μm) by passing the infrared light through two potassium dihydrogen phosphate (KDP) crystals. The first crystal doubles the frequency of a fraction of the infrared light, while the second crystal combines the remaining infrared light and the frequency doubled light to produce UV light. The 60 UV beams are then distributed uniformly over a large, 3.3 m diameter spherical vacuum chamber and focused to the center of the chamber by 1.8 m focal length, f/6.7, fused-silica aspheric lenses. The target diagnostics are inserted into the chamber through external ports positioned

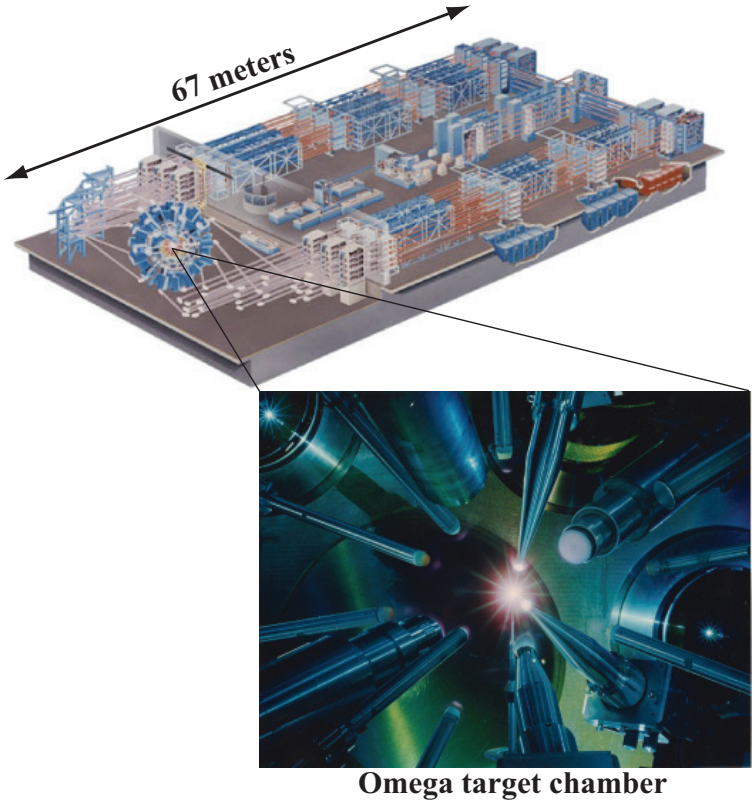

Figure 1.4: The Omega laser facility is shown here in a computer aided image. The long rows of equipment near the outside of the image are the final stages of the Nd:glass amplifiers. All of the beams can be focused into the 3.3 m diameter target chamber, which is located at the left end of the image. The picture shows the interior of the target chamber during an experiment when the lasers were fired. The target is located at the center of the picture and is surrounded by diagnostics.

around the chamber wall. Phase smoothing, polarization smoothing, and smoothing by spectral dispersion are all beam smoothing techniques used to achieve 1 to 2% irradiation non-uniformity of a single beam. Although each beam is capable of depositing a maximum of 500 J on target, the typical energy per beam is approximately 375 to 400 J if all smoothing techniques are employed. A variety of temporal and spatial pulse shapes are available on Omega. In many HEDP experiments, the beams are configured for a 0.2 to 1 ns (one-billionth of a second) temporal pulse length and a 0.8 to 1 mm diameter footprint. The maximum shot rate is around 1 shot/hour and is limited by the cooling time of the Nd:glass amplifiers, if there are no problems

with the target or the diagnostic alignment. On a good day a total of more than 10 shots can be expected.

1.4.2 Nike laser

The Nike laser, located in Washington, DC at the Naval Research Laboratory (NRL), is the largest laser of its kind and was built as a prototype for a larger laser system that could ultimately be used in a fusion power plant [52, 6]. The work done at NRL on Nike, and on the related Electra laser, represents the largest effort put forth by any group to make a fusion power plant feasible. Unlike Omega, the Nike laser uses a krypton-fluoride (KrF) gas mixture, instead of Nd:glass, as the lasing medium. High-energy electron beams, instead of flash lamps, are used to pump the gas into an excited state before a seed pulse extracts the energy. The Nike laser generates 56 beams with a total of 2 kJ of energy at a wavelength of 0.248 μm. Typically 44 of these beams are used to drive a target, while the remaining 12 are dedicated diagnostic beams. See Figure 1.5 for pictures of the target chamber and the main laser amplifier.

There are several advantages of KrF lasers over glass lasers. By operating at a shorter wavelength (0.248 compared to 0.351 μm) a KrF laser can potentially deposit more energy into a target by using higher laser irradiances (perhaps beyond $2\text{x}10^{15}$ W/cm^2) without suffering from laser-plasma instabilities, which act to decouple laser energy from the target [53]. The higher irradiances allow a thicker capsule to be used, which in turn increases the stability of the implosion. Furthermore, the high bandwidth that is intrinsic to KrF lasers lends itself to a spatial smoothing technique known as induced spatial incoherence (ISI). This technique does not rely on complicated optics such as distributed phase plates or diffractive gratings, but rather on the naturally short coherence time of the individual beams. When the beams are combined in the target plane the short coherence time leads to rapid constructive and

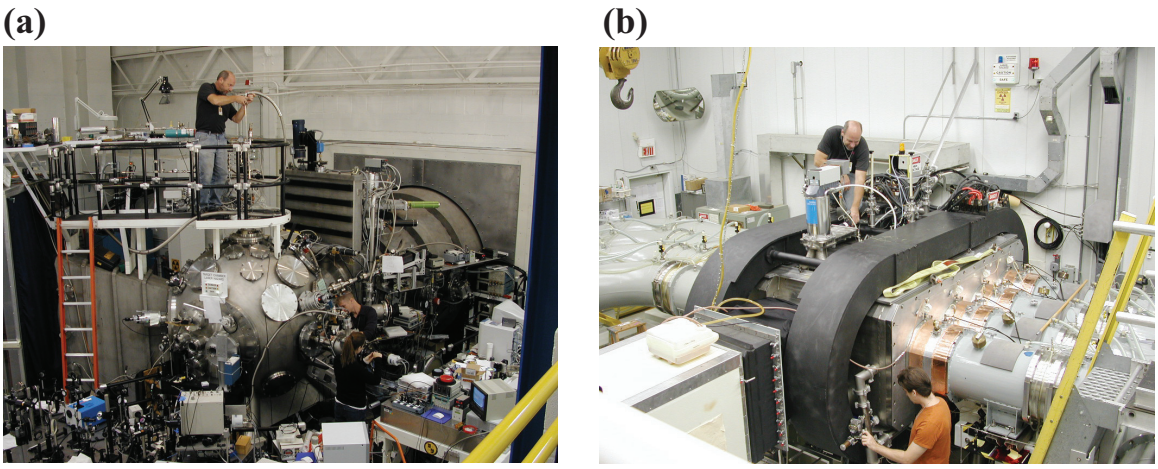

Figure 1.5: (a) The main chamber into which all of the Nike beams are focused. Attached to the chamber ports and the surrounding optical tables are the various target diagnostics. (b) This picture shows the main amplifier of the Nike laser. The two large black coils are electromagnets used to confine the high-energy electron beams generated by the discharge of several banks of capacitors onto velvet covered cathodes. The KrF gas is contained in a 60 x 60 x 125 cm chamber located between the black coils. The laser light enters and exits the amplifier through the square tunnel at the lower left of the image.

destructive interference creating a short-lived speckle pattern. With all 44 Nike drive beams overlapped, the time average non-uniformity of the spatial profile is 0.3%. The spatial profile is rotationally symmetric and is 750 μm FWHM with a 400 μm flat top. The nominal temporal pulse length is 4.2 ns with each beam delivering approximately 40 J on target. Typically 40 drive beams are focused onto the target, while the remaining 4 beams are blocked by calorimeters that measure the beam energy. In this configuration, $\sim$ 1.4 to 1.6 kJ is delivered to the target with beam irradiances around 5 - 8x10^{13} W/cm^2. Higher irradiances can be achieved by focusing the beams to a smaller spot size and using shorter temporal pulse shapes. Typically, the shot rate is around 1 shot/hour. This is limited by the time required to pump the target chamber down to vacuum ($\sim 10^{-5}$ Torr). On a good day a total of more than 8 shots can be expected.

1.5 Summary of chapters

The introduction provided in this first chapter motivates the study of laboratory fusion and high-energy-density experiments that are relevant to astrophysical phenomena. Looking more closely at these systems, shear flows appear to be an important aspect that remains relatively unexplored. In Chapter II, the initial development of an experiment dedicated to the investigation of a HED shear flow is discussed. This experiment was designed specifically for the Nike laser. The work in Chapter II was published in the journal *High-Energy-Density Physics* [54]. After the presentation of the preliminary experiments in Chapter II, a more in depth discussion related to the analysis and simulation of these experiments is presented in Chapter III. The work in Chapter III was published in the journal *Physics of Plasmas* [55]. Then in Chapter IV the results of another shear flow experiment are discussed. This experiment was carried out on the Omega laser, and was the first to observe the evolution of the KH instability in a HED plasma. The work present in Chapter IV was published in *Physical Review Letters* [56] and other papers [57, 58]. Finally, in Chapter V the conclusions and future directions of these experiments are discussed.

In addition, Appendix A includes a brief introduction to a common imaging diagnostic known as an x-ray framing camera and its associated microchannel plate (MCP) component. A three-dimensional MCP model and a novel MCP characterization technique are then presented. This work was previously published in *Review of Scientific Instruments* [59]. Appendix B serves as a library of all the image data that did not appear in the chapters of this thesis. Appendix C contains an additional radiographic image that was not presented in Chapter IV, as well as a detailed shot log from the Omega KH experiment.

CHAPTER II

Experimental Design for Generating Strong Shear Layers with the Nike Laser

2.1 Introduction

The development of a new experimental platform for generating a strong shear flow in a HED plasma is described in detail. The targets were designed with the goal of producing a diagnosable Kelvin-Helmholtz (KH) instability. Other HED experiments have shown some evidence of the KH instability, yet the instability was under-resolved and not easy to diagnose [36, 60, 61]. To generate the shear flow the Nike laser was used to drive a flow of Al plasma over a low-density foam surface that had machined perturbation. The interaction of the Al and foam was captured using x-ray radiography at an energy of 1.865 keV. The selection of the individual target components is discussed and results are presented in this chapter.

2.2 Experimental Constraints

A shear flow requires a sustained flow of fluid, and for laser-driven, HED experiments the amount of mass involved in the flow is limited by the deposited laser energy on the target. The Nike laser typically delivers 1.5 kJ to the target. The detailed operating parameters of the Nike laser are described in Section 1.4.2. For this exper-

iment 10 of the 12 dedicated diagnostic beams (also known as "backlighter beams") were used to generate x-rays for radiographic imaging of the target. The remaining 2 backlighter beams were blocked by calorimeters that measured the beam's energy. The temporal pulse length of all the backlighter beams can be varied from 0.3 to 5 ns. The backlighter beams were delayed relative to the start of the drive beams in order to capture the target dynamics at various intervals. We chose to irradiate a piece of Si wafer in order to generate He-α x-rays (1.865 keV) for ungated radiography. The images presented here used a 0.3 ns backlighter pulse and a Fuji BAS-TR image plate as the detector. The maximum delay between the start of the drive beams and the backlighter beams is $\sim$ 17 ns for the Nike laser. This is limited by the original pulse length ($\sim$ 20 ns) of a low-energy laser that simultaneously provides the seed pulses for both the main and diagnostic beams. Therefore, all the target dynamics that we hoped to observe must take place within 17 ns from the start of the main beam pulse.

The initial target features as well as the evolved features must be resolvable by the imaging diagnostic. At the Nike facility, spherical crystal x-ray radiography has routinely achieved 10 μm resolution [62]. The time dependent growth of the KH instability in the linear regime where the ratio of the initial amplitude and the perturbation wavelength is less than 10% ($\eta_o/\lambda < 0.1$) is given by $\eta(\mathrm{t}) = \eta_o e^{\gamma t}$ where γ is the growth rate of the KH instability in its linear phase. For an inviscid and incompressible shear layer with an infinitely thin transition region

$$\gamma = \frac{k\Delta U}{2}\sqrt{1 - A^2}, \tag{2.1}$$

where k is the wavenumber of the perturbation, ΔU is the flow velocity difference across the interface, and A is the Atwood number [63]. A homogenous shear layer ($A = 0$) with $\lambda = 100$ μm and ΔU = 10 μm/ns (ΔU = 100 μm/ns) will give an e-folding time of $\sim$ 3 ns (0.3 ns). After one e-fold a perturbation with $\eta_o = 10$ μm

would grow to $\eta = 27$ μm, which would be detectable. Any further growth is difficult to predict with linear theory. However, a simple non-linear model predicts that the maximum amplitude is 0.28 λ [64]. Since flow speeds in excess of 10 μm/ns are easily achieved in HED experiments, it appeared feasible to design an experiment that would show detectable KH growth in the 17 ns window available on Nike. Nevertheless, the above analysis requires a steady state flow, a condition that is rarely achieved in any HED experiment. One might expect that a single wavelength of the perturbation must experience shear for the duration of one e-folding time in order to achieve the growth predicted by linear theory. If this were the case, the spatial extent of the flow (H) must be $\sim \Delta U \gamma^{-1} + \lambda$. For $A = 0$ and $\lambda = 100$ μm, $H = \lambda(\pi^{-1} + 1) = 132$ μm. However, this simple calculation assumes that the fluids have infinite depths. Reference [34] explores the effects of finite fluid depth D on the linear KH growth rate, and shows that the growth rate decreases for $D < \lambda$. This implies that a larger extent of flow material is required to produce one e-fold of KH growth. Likewise for stratified shear layers ($A \neq 0$) that are Rayleigh-Taylor stable, γ is smaller so a larger spatial extent of the flow is also required to produce one e-folding of growth.

2.3 Nike Target Design

The main components of the target are shown in Figure 2.1. Figure 2.2 shows a picture of a completed target. The overall concept was to create a high-velocity flow of plasma (referred to as the drive flow) over a low-density foam surface with a single mode perturbation. To create the flow the Nike laser was used to irradiate a thin foil of material. The large ablation pressure created by the laser launched a forward shock into the foil, which was compressed and ionized. The shock broke out of the rear of the foil into a vacuum gap. Depending on the size of the gap and the laser temporal duration the flow will decompress and increase its spatial extent to varying degrees as it accelerates across the gap. The foam was placed at the end of the gap

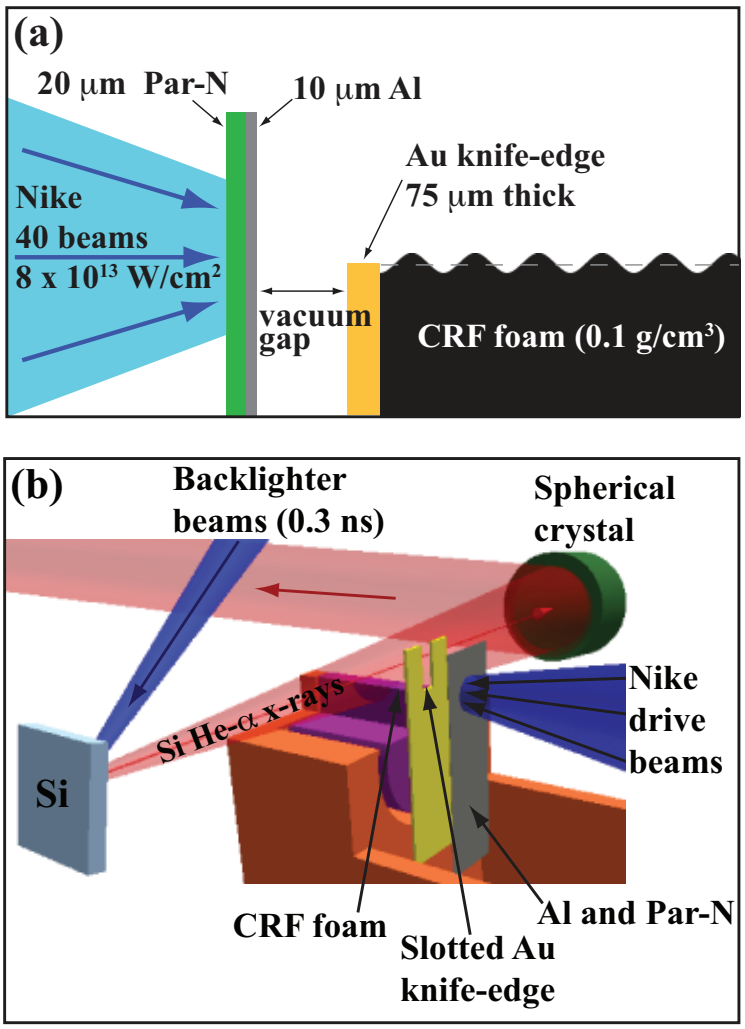

Figure 2.1: (a) A cross-sectional view of the Nike target designed to create a free shear flow that is potentially Kelvin-Helmholtz unstable. The foam perturbations were single mode and had wavelengths of 100, 200, and 300 μm wavelengths with 10, 20, and 30 μm peak-to-valley amplitudes respectively. (b) A three-dimensional rendering of the target showing the spherical crystal imaging diagnostic. Here the slotted knife-edge is shown along with the basket in which the stock foam was glued in order to perform the machining operations.

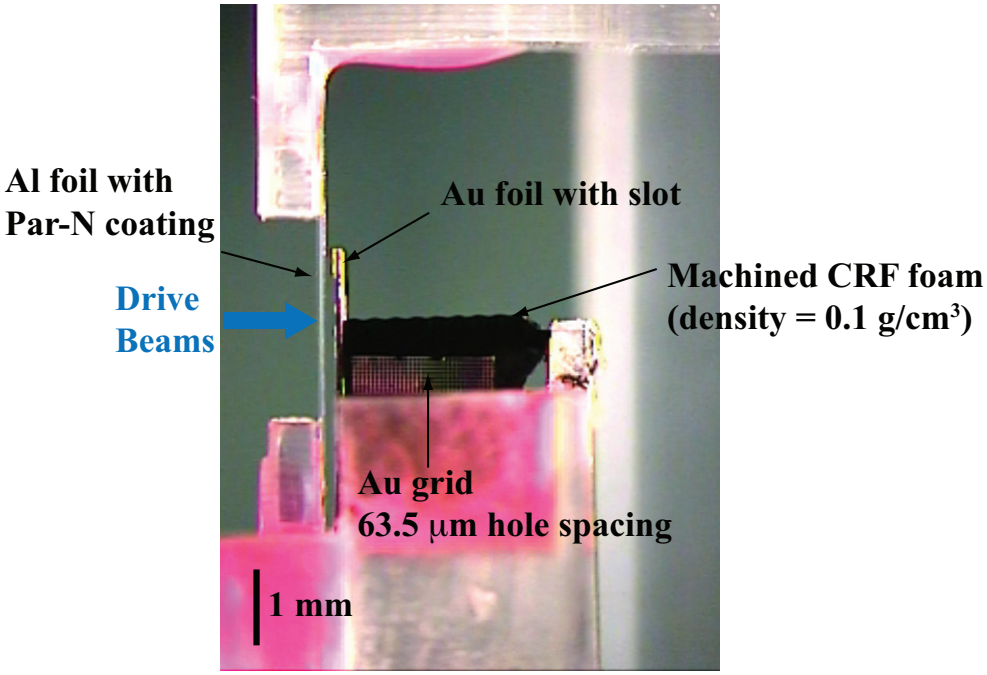

Figure 2.2: Shown here is a picture of a complete Nike target. The foam perturbation of this target had a wavelength of 300 μm and an amplitude of 15 μm. The pink material is UV curing epoxy.

and was typically protected by a slotted gold foil (see Figure 2.1b), which we will refer to as the knife-edge. The knife-edge preserved the shape of the foam as the top half of the flow interacted with the foam surface. When the flow struck the lower half of the knife-edge a forward shock was driven into the gold, while a reverse shock propagated back into the oncoming flow. As the top half of the Al plasma flowed over the foam surface the internal and ram pressures of the flow drove lateral shocks down into the foam. The shocked foam then served as the second fluid with which the drive flow interacted to produce a shear layer. The machined perturbations on the foam surface provided an initial seed for the KH instability. In the following sub-sections the selection of each target component is described.

2.3.1 Knife-edge Design

The knife-edge was designed to collimate the drive flow and protect the foam. The thickness of the knife-edge was chosen so that the forward shock propagating

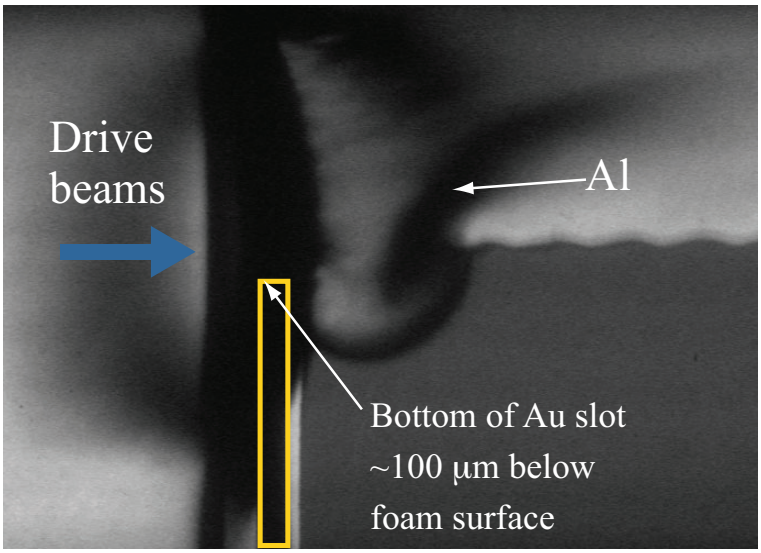

Figure 2.3: For this target the bottom of the slot in Au knife-edge was positioned $\sim$ 100 μm below the surface of the foam. This experiment demonstrated the important role that the knife-edge plays in protecting the foam. In this image it appears that a bow shock was formed due to impact of the supersonic Al flow onto the foam.

through it would break out significantly later in time and would not interfere with the dynamics taking place on the foam surface. Figure 2.3 provides experimental confirmation that the knife-edge was necessary to preserve shape of the foam. Initial 1D Hyades simulations indicated that the knife-edge thickness should be $\sim$50 to 75 μm [65]. All the results presented here used a 75 μm thick knife-edge. However, at this thickness the break out of the knife-edge shock was observed in experiments, so future experiments should use a greater thickness. Entrainment of gold from the knife-edge did not appear to be an issue, based on the radiographs, even when the thickness was increased to 150 μm on a single prototype target. As shown in Figure 2.1b the slot in the knife-edge was extended 1 mm above the surface of the foam in order to help collimate the drive flow. The width of the slot was 400 μm to match the drive beam spot size in an attempt to drive the largest amount of mass at a uniform velocity. The knife-edges were laser cut from a 75 μm thick gold foil by a commercial vendor. A 75 μm tungsten foil with a 300 x 300 μm aperture was tested, but was found to restrict

the amount of mass that passed through the opening and appeared to create a flow with a greater divergence than the slotted design. In addition, an angled knife-edge with a 30° bend starting at the bottom of the slot was found to work well. However, it proved difficult to machine the foam with a matching shape so that it could attach directly to the knife-edge. In all cases, the bottom of the knife-edge was centered on the foam perturbation as shown in Figure 2.1a.

2.3.2 Foam selection and machining

The foam chosen for this experiment was carbonized-resorcinol-formaldehyde (CRF) with a density of 0.1 g/cm^3 and an average cell size of 0.020 μm. The composition of the foam, by percent mass, is 93% C, 6% O, 1% H. CRF foam was selected for two reasons. First, at a width of 400 μm, CRF foam provides 1.5 optical depths at 1.865 keV. This created good contrast in the foam image, which allowed us to observe the lateral shock propagating in the foam. Second, CRF is relatively easy to machine compared to SiO_2 ("aerogel") or divinyl-benzene (DVB) foams. The machined seed perturbations are an important aspect of the target since they provided the initial conditions for the flow in the experiment and for future 2D simulations. Our first machined patterns were circular grooves scratched into a flat foam surface using a lathe. More advanced techniques allowed us later to machine sinusoidal perturbations with wavelengths of 100, 200, and 300 μm with peak-to-valley amplitudes equal to 10, 20, and 30 μm, respectively. See Figure 2.4 for SEM images of typical finished foam pieces. These perturbations were machined at the University of Michigan using a custom 25 μm radius diamond tool from Chardon Tool on a conventional CNC lathe. The patterns were first cut using the lathe, and then transferred to a CNC end mill to machine the foam into its final shape. The width of the foam was machined to 400 μm in order to match the width of the knife-edge. Most of the surface roughness of the final piece was due to chipping that extended below the surface.

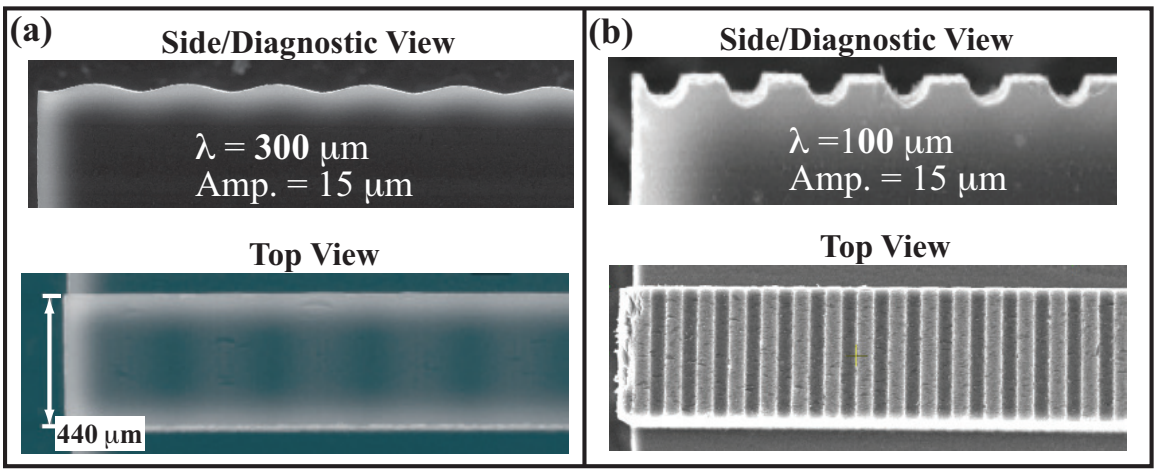

Figure 2.4: Scanning electron micrographs of completed foam pieces. The foams were machined at the University of Michigan with a conventional CNC lathe and end mill. (a) A sinusoidally patterned foam with $\lambda = 300$ μm and peak-to-valley = 30 μm. (b) A grooved pattern with grooves spaced at 100 $/mu$m intervals and 30 μm deep. The groove radius was ~ 25 μm.

The sinusoidal perturbations represented the most advanced pattern we were able to machine. Multi-mode patterns were not attempted. Overall, we were surprised to find that we could machine these patterns with our lathe, which has relatively coarse minimum tool movements of 3 μm. The ability to machine CRF was important in order to fabricate a large quantity (>50) of low-cost targets.

2.3.3 Drive Foil Selection

Three materials were tested as drive foil candidates: polyimide (i.e., Kapton), polystyrene, and aluminum. Experiments showed that after passing through the knife-edge only the Al had sufficient velocity, and enough opacity to be observed in the radiograph. Although 1D Hyades simulations indicated that all three materials should be visible, the 3D decompression of the plasma and the loss of mass at the knife-edge made all materials less opaque than predicted. After some initial experiments the Al foil thickness was set at 10 μm. Using this foil thickness the spatial extent of the flow was 200 to 300 μm, and it had a bulk velocity between 50 and 100 μm/ns.

In order to maximize the KH growth rate we attempted to match the shocked foam and Al densities, yet in most cases the Al density was 0.030 g/cm^3 and the shocked foam density was 0.18 g/cm^3. Future experiments should try a lower foam density, which can be as low as 0.020 g/cm^3 for CRF foam. The Al foil was coated on the laser-driven surface with 10 or 20 μm of plastic in order to prevent the laser from directly irradiating the Al and producing x-rays. Initial experiments used Parylene-C, but later experiments used Parylene-N. Parylene-C contains chlorine that, when irradiated by the laser, has the potential to generate x-rays that could preheat the target. We found no evidence of preheat, yet we used 20 μm of Parylene-N on all of the Al drive foils as a precautionary measure. After our initial experiments, we found the Al drive foils had large surface perturbations that were believed to cause the clumping of the drive plasma seen in some of the radiographs. These foils were 10 μm thick with maximum perturbation amplitudes of $\sim$ 1 μm and wavelengths concentrated in the 50 to 100 μm range. The perturbations resulted from the cold rolling manufacturing technique used to flatten the foil to a specified thickness. This foil was purchased from Alfa Aesar and was 99.0% pure Al. Later experiments used foils that were made by evaporating Al onto a glass slide. These foils were purchased from the Lebow Company and were 99.99% pure Al. This technique, known as thermal evaporation deposition, produced foil perturbations with maximum amplitudes less than 0.025 μm on the Al surface that was not adhered to the glass and even smaller amplitudes on the glass interfaced surface. These improved foils with the smaller perturbations yielded a more uniform flow of plasma with less clumping observed in the radiographs.

In order to create a free shear layer, the internal pressure of the Al flow must drive a lateral shock into the foam and create a second fluid. As mentioned previously the foam fluid depth (D), which is determined by the lateral shock depth in the foam, affects the KH growth rate. If the foam remained completely rigid (i.e., $D = 0$) then there is no possibility of the KH instability forming. In this case, a boundary

layer would form with characteristic scales that are distinctly different from those of a free shear layer. In addition, the entire width of the foam surface should be shocked uniformly so the width was designed to match the constant irradiance width of the overlapped drive beams, which was 400 μm. The collimation of the Al by the knife-edge prevented contamination of the diagnostic line of sight with Al that was driven by the low irradiance wings of the laser spot. Due to the high x-ray opacity of the Al at 1.865 keV, very little is needed to obscure the foam surface from the diagnostic line of sight. A more sophisticated target might use a shock tube made from Be to contain the entire experiment. Yet due to safety concerns Be cannot be irradiated in the Nike laser chamber. In addition, a rigid plastic shock tube with low opacity was difficult to fabricate, so we were forced to design an experiment with no shock tube. Using higher energy x-rays (around 5 keV), future targets could use thick plastic (perhaps acrylic) shock tubes with thin observation windows. The target could be machined from a single piece and then thinned down to 50 μm where the observation windows are needed.

2.3.4 Vacuum Gap Sizing

Initial experiments demonstrated that the size of the vacuum gap affected the amount of mass that propagated through the knife-edge. See Figure 2.5 for a comparison of the different Al and knife-edge geometries. In the initial target design, the vacuum gap was made large enough so that the drive laser would end before the Al plasma encountered the knife-edge. This would allow the plasma to expand in the vacuum gap and increase its overall spatial extent, thereby increasing the interaction time of the Al plasma and the foam. Furthermore, we did not want the laser to directly irradiate and ablate the foam, which would produce undesirable effects that are unrelated to shear and difficult to accurately capture with numerical simulations. Taking this into consideration, 1D Hyades simulations indicated the gap should be

500 to 900 μm wide. Yet, at these sizes experiments showed that very little mass was visible in the radiographs, and there was essentially no interaction with the foam (see Figure 2.5f). We suspect that lateral spreading of the reverse shock developing in front of the knife-edge restricted the flow of plasma through the slot. However, when the gap size was decreased there was less time for this reverse shock to develop since the flow was more compact. After some initial experiments we determined that a gap of 100 μm produced the most uniform flow of Al plasma. At these gap sizes, there was no strong evidence of disruption of the foam from direct laser illumination. Targets with a zero distance gap (i.e., the Al foil was directly attached to the knife-edge) were tested and found to work well. In addition, several targets were designed with the Al foil attached behind the gold slot, so the laser spot was masked by the gold before it struck the Al. This geometry did not produce a uniform flow of Al and appeared to create a large amount of gold debris. Figure 2.5b also shows a radiograph from a target with a side cut knife-edge. In this geometry the knife-edge slot was orientated orthogonal to its nominally vertical position, so that the width of the Al was observed without changing the diagnostic position.

Future experiments should further investigate targets that use a zero distance gap. These targets were able to create a large amount of uniformly distributed mass behind the knife-edge. A reflected shock does not appear to inhibit the flow through the opening in this design. If a more extended flow is desired then the use of angled knife-edges, as mention in Section 2.3.1, should also be investigated. Increasing the complexity of the target geometry may be worthwhile if a less restricting opening can be created. Perhaps the simplest angular design is one that is bent around the bottom edge of the slot to form a V-shape. When the drive flow first impacts the knife-edge, it would only encounter a single edge instead of striking the entire surface. The drive flow would then be deflected away from the opening, allowing the flow in line with the slot to propagate through. This effect can be seen in Figure 2.6c. To

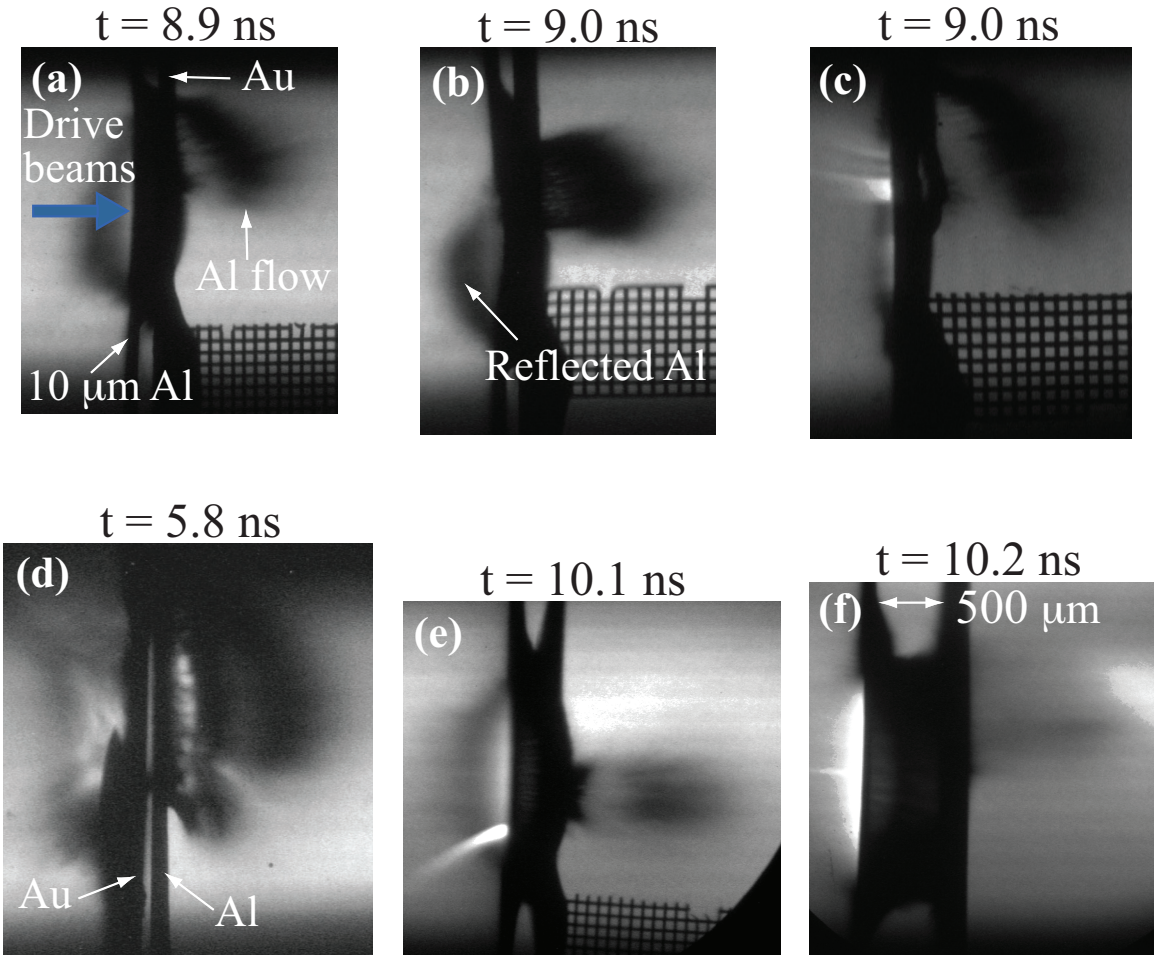

Figure 2.5: Here are radiographs of six different driver configurations that were tested on the Nike laser. The time was measured from the start of the drive pulse. All six used a 10 μm Al foil coated with parylene on the drive surface. Unless otherwise specified the Al foil was smooth (i.e., not cold rolled). (a) This became the workhorse drive setup. Al was coated with 20 μm Parylene-N on the drive surface and had a nominal vacuum gap of 100 μm. (b) Same configuration as (a) but with an orthogonally cut knife-edge so that the view is orthogonal to that of (a). (c) Same configuration as (a) but no vacuum gap. (d) Same as (a) but the knife-edge was placed in front of the Al. (e) Cold rolled Al was used and coated with 20 μm Parylene-C on the drive surface. A W foil with a 300 x 300 μm aperture was used instead of the slotted gold knife-edge. (f) Cold rolled Al was used and coated with 10 μm of parylene-N on the drive surface. The slotted gold knife-edge was used and the vacuum gap was set to 500 μm.

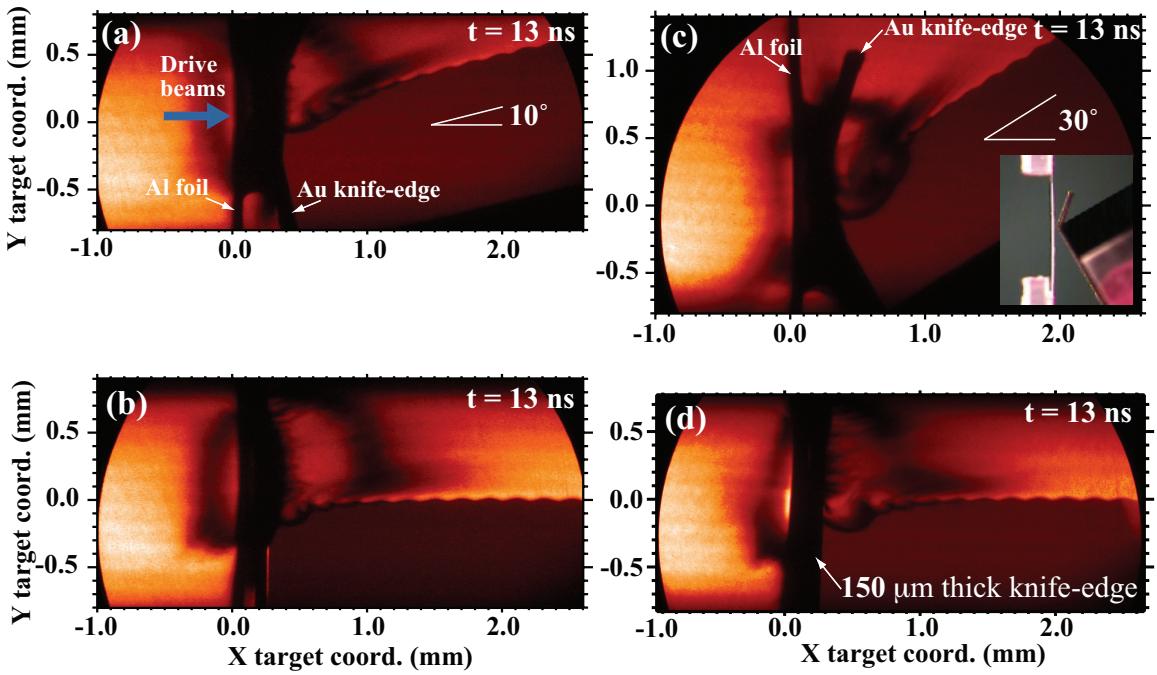

Figure 2.6: Shown here are four radiographs from the second experimental campaign. The foams had perturbations with wavelengths of 200 μm and peak-to-valley amplitudes of 20 μm. The vacuum gap was 100 μm for all targets. The radiographs were captured ∼13 ns after the start of the drive beam pulse. (a) The foam was tilted 10° and the knife-edge was bent into a V-shape with an opening angle of 150° . (b) This target was the same as (a) but the foam was not tilted and the knife-edge was flat. (c) The foam was tilted 30° and the knife-edge was bent into a V-shape with an opening angle of ∼130° . The inset image is a photograph of the target. (d) This target used a 150 μm thick knife-edge and a zero distance gap.

the left of the original Al foil position (x = 0), more mass has been deflected away from the centerline of the target compared to targets with flat knife-edges such as the one shown in Figure 2.6b. A more sophisticated design could further bend the two upright sections of the slots into the diagnostic line of sight in order to form a nozzle-like structure.

2.3.5 Modular Target Design

After our first experimental campaign we switched to a modular target design that had several interchangeable components. A small, portable fabrication station

was constructed on top of a 2 x 4 ft optical breadboard, and transported to the Nike facility. This station was used to assemble and metrologize the targets. The station and the modular design allowed us to quickly change our target geometry as new data continued to improve our understanding of the target physics during the campaign.

2.4 Experimental Results

The majority of the data were collected from two experimental campaigns. The first campaign used a 10 μm Al foil (cold rolled and coated with 20 μm Par-C), followed by a 200 μm vacuum gap and a W foil with a 300 μm x 300 μm aperture as mentioned previously. The foam perturbations in this case were the circular groove type shown in Figure 2.4b. Figure 2.7a shows a radiograph from the first campaign. The second campaign used a 10 μm foil (made by evaporative deposition and coated with 20 μm Par-N) and a nominal 100 μm vacuum gap. Instead of the W aperture a gold foil with the 400 μm slotted knife-edge was used. In addition, the more advanced sinusoidal pattern was developed for the second campaign and employed on all the foam pieces (see Figure 2.4a). Figure 2.7b shows an image from the second campaign. The foam perturbations increase their vertical extent in both targets in Figure 2.7. These images show that the perturbations extend in the direction opposite to the flow. This backwards tilting is perhaps due to the non-uniform pressure applied to each perturbation. The upstream side (i.e., the side closest to the knife-edge) of the perturbation experiences a larger ram pressure than the downstream side. In addition, distinct dark bands formed above the perturbations. These may be the result of shocks forming in front of the perturbations due to the supersonic flow of Al. Detailed analysis of these data will be reported in Chapter III. The bands also appeared in tilted foam targets shown in Figure 2.6a and c. The 10° tilted target produced more perturbation growth than a nearly identical target with no tilt shown in Figure 2.6b. The foam pieces were tilted in an attempt to increase the ram pressure

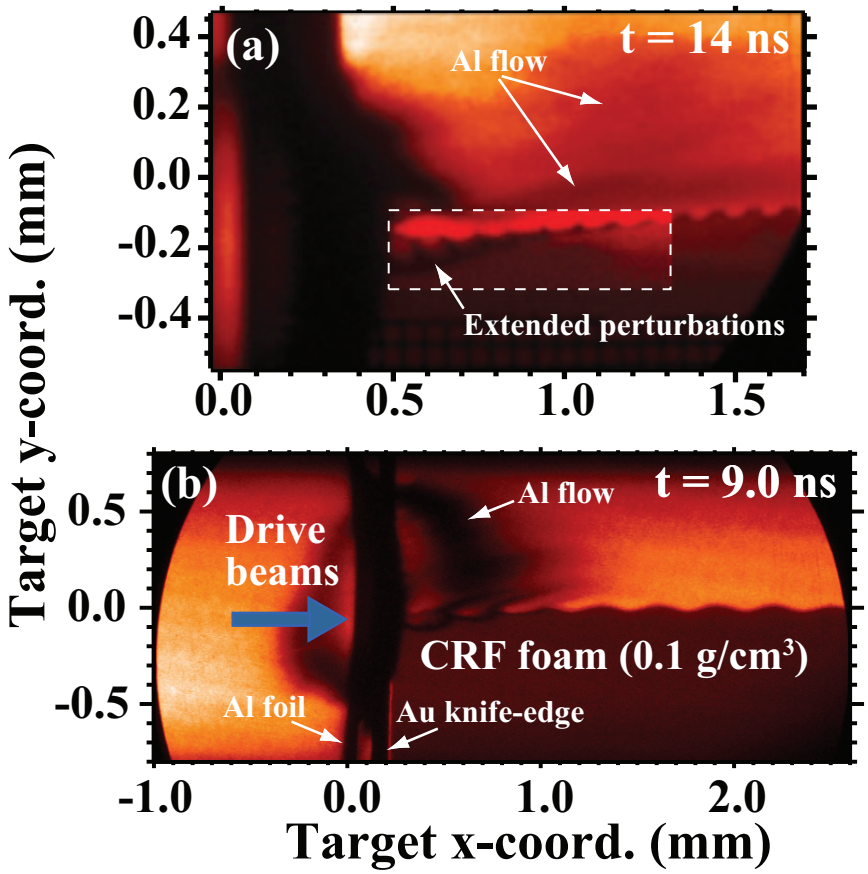

Figure 2.7: Shown here are radiographs from two separate targets from the first and second experimental campaigns. The time corresponds to the elapsed time between the start of the drive beams and when the image was captured. (a) The first campaign used a 75 μm thick W foil with a 300 x 300 μm aperture to collimate the Al flow. The perturbations were circular grooves with a radius of 25 μm and spaced at 100 μm intervals. The region inside the dashed box was enhanced to show the extended perturbations. (b) The second campaign used a 400 μm slotted Au knife-edge to collimate the flow. The perturbations were a single mode sinusoid with λ= 300 μm and a peak-to-valley amplitude = 30 μm.

created by the incident Al and cause a greater interaction between the Al and foam. The tilted targets also used a V-shaped knife-edge, discussed in Section 2.3.4, which appeared to work well. In Figure 2.6c enough mass was deflected away from the knife-edge such that the leading edge of the knife-edge is visible. Future shear experiments should further investigate the V-shaped knife-edge with un-tilted foams. Finally, Figure 2.6d shows a target that used no gap and had two knife-edges glued together to create a single knife-edge with the same original shape but with a total thickness of 150 μm. The extra thickness contained the forward shock in the knife-edge and appeared to collimate the Al flow without entraining much of the gold. Perhaps, a more advanced knife-edge could have internal surfaces that were specifically machined like a rocket nozzle in order to tailor the shape of the flow.

2.5 Summary

A new experimental target aimed at creating a strong shear layer in a HED plasma was developed and fielded on the Nike laser. The experiment demonstrated a clear interaction of an Al flow and a rippled foam surface. Various target configurations were tried, and it was found that the behavior of the target depended on the geometry of the knife-edge. In the future a more sustained drive flow may be achieved by using an angled knife-edge or thick knife-edges with shaped internal surfaces. A modular target design allowed us to rapidly assemble or modify a target during a single shot day. This proved to be beneficial when fielding new targets.

CHAPTER III

Supersonic Flow Over a Compressible Wall on the Nike Laser

3.1 Introduction

This chapter focuses on the detailed analysis of one of the target designs discussed in Chapter II. As mentioned in Chapter II, these targets used the Nike laser to create and drive Al plasma over a rippled foam surface. The experiments presented in this Chapter used a ripple with a 300 μm wavelength and a 15 μm amplitude in order to seed the KH instability. The analysis of these experiments revealed that the flow of Al was supersonic (Mach = 2.6 $\pm$ 1.1). In response to the supersonic Al flow shocks are expected to form in the Al flow near these perturbations. An analysis of the experimental radiographs was used to infer the existence and composition of the shocked regions of the flow. In addition, the interface perturbations exhibited growth that had possible contributions from both Kelvin-Helmholtz (KH) and Richtmyer-Meshkov (RM) instabilities. At supersonic Mach numbers compressible effects can significantly influence the growth of the KH instability, so it is important to use the growth rate derived from the compressible dispersion relation. Two-dimensional FLASH simulations are used to gain further insight into the detailed evolution of the experiment [66]. These simulations confirm that shocks are indeed expected

to form near the perturbations. Previous experiments have also created supersonic flows, most notably high Mach number jets have been generated using laser driven targets and Z-pinch machines [67, 68, 69, 70]. In addition, the post shock flow in many HED experiments is supersonic in the laboratory reference frame and thus will support reflected shocks from various objects inserted into the flow. Nevertheless, this particular target geometry is the first of its kind, and it has provided insight into the interaction of a supersonic flow and a structured interface.

3.2 Experimental Setup

To create the high velocity Al flow, the Nike laser irradiated a 10 μm thick Al foil (99.99% pure Al) coated with 20 μm of plastic (Parylene-N, C_8H_8, ρ= 1.10 g/cm^3) as shown in Fig. 2.1a. For this experiment 38 of the 44 drive beams were used, yielding a total of 1.4 kJ on target and a corresponding maximum irradiance of 8 x 10^{13} W/cm^2. The plastic serves as an ablator and prevents the laser from directly illuminating the Al, which would otherwise generate x-rays that might preheat the target. At t = 0 the plastic was initially irradiated by only three beams with a total irradiance of 6.6 x 10^{12} W/cm^2, which drove a shock into the plastic. Then at t = 1.4 ns the remaining 35 beams turned on, and created a large ablation pressure ($\sim$ 10 Mbar) that launched a second shock into the bulk of the plastic and then into the Al. One-dimensional Hyades simulations indicate that this second stronger shock overtook the weaker shock in the Al before it broke out into vacuum. At t $\sim$ 2 ns the shock broke out of the Al and into vacuum. A rarefaction wave was then launched back into the Al plasma as the leading edge of the Al expanded into vacuum. At t = 4.2 ns the initial three beams switched off and the target was driven until t = 5.8 ns by the remaining 35 beams with an irradiance of 7.7 x 10^{13} W/cm^2. After the shock broke out the laser continued to drive the target for an additional 3.8 ns, which kept the spatial extent of the Al compact. The rarefaction in the plastic did not begin

until the end of the laser drive. After expanding across a 100 μm vacuum gap the Al flow was split into two sections by a 75 μm thick gold foil that was positioned in the center of the flow (i.e., directly behind the center of the laser spot). The primary purpose of the gold foil was to protect the low-density carbon resorcinol-formaldehyde (CRF) foam that was located behind the gold foil. The CRF had a density $\rho = 0.1 \pm 0.005$ g/cm^3 and an average cell size of 0.02 μm. The gold reflects the lower half of the Al, while the top half continues to flow along the perturbed CRF foam. As shown in Fig. 2.1a, sinusoidal perturbations were machined into the surfaces of the foam pieces to provide a seed for the KH instability. Three different perturbations were fielded with wavelengths equal to 100, 200 and 300 μm with amplitudes of 5, 10, and 15 μm respectively. The edge of the gold was aligned with the center of the perturbation, allowing the Al flow to interact only with the surface. The Al drives a shock into the gold foil, yet the thickness of the gold has been chosen so that the shock broke out late enough in time such that most of the foam surface was unaffected. To further collimate the Al flow, two sections of the gold foil extended 1 mm above the foam surface, forming a rectangular slot in the center of the foil with a 400 μm wide opening as shown in Fig. 2.1b. The CRF foam was machined to a width of 400 μm in order to match the width of the slot. The slot width was chosen to match the constant intensity width of the laser spot in an attempt to drive the largest amount of mass at a uniform velocity.

The target was imaged using un-gated x-ray radiography with a spherically bent quartz crystal operated at a magnification of 13 [62]. Ten of the diagnostic beams were focused onto a small piece of Si wafer that produced x-rays used to back light the target (see Fig. 2.1b). The temporal duration of the diagnostic beams was set at 300 ps to create a short burst of x-rays to capture the target dynamics without excessive motion blurring. The various target materials differentially absorbed the x-rays as they passed through the target on their way to the crystal. The crystal selected the

1.865 keV Si He-α x-rays and imaged them onto a Fuji BAS-TR imaging plate, which was shielded by a 13 μm Be filter. The image plate was scanned with a Perkin-Elmer Cyclone image plate scanner that produced an image with 42 μm square pixels. The resolution of the spherical crystal imager is theoretically limited by astigmatism, yet more often it is the local bending quality of the crystal that determines the final resolution. Modular transfer functions (MTF) were generated from images of both vertical and horizontal razor blades in the target position. The MTF of the vertical razor blade had values of 0.1 and 0.5 at wavelengths equal to 12 μm and 30 μm respectively. The MTF of the horizontal razor blade had values of 0.1 and 0.5 at wavelengths equal to 20 μm and 55 μm respectively. The vertical and horizontal MTFs sampled different regions of the target plane, which were in turn imaged with different parts of the crystal. Thus, this resolution variation was mostly likely due to the variation of the local crystal quality and not astigmatism. Figure 3.1 shows both vertical and horizontal MTFs. The dashed lines were determined by taking the Fourier Transform of a Gaussian profile that was fitted to the line spread function (LSF). The LSF was computed by taking the numerical derivative of the intensity profile across the razor image. This intensity profile is known as the edge response of the detector.

3.3 Experimental results

Figure 3.2 shows radiographs from four separate targets captured at different times. These images show the Al being pushed through the Au knife-edge and then interacting with the foam. In Fig. 3.2a the upper half ($y > 0$) of the Al flow encountered the foam, while the lower section ($y < 0$) was reflected back toward the laser. Later in time, as seen in Fig. 3.2b the full extent of the Al emerged from the Au knife-edge and appeared as a shell of material with an average width of 200 to 300 μm. The curvature of the shell is due to the variation of the laser drive irradiance.

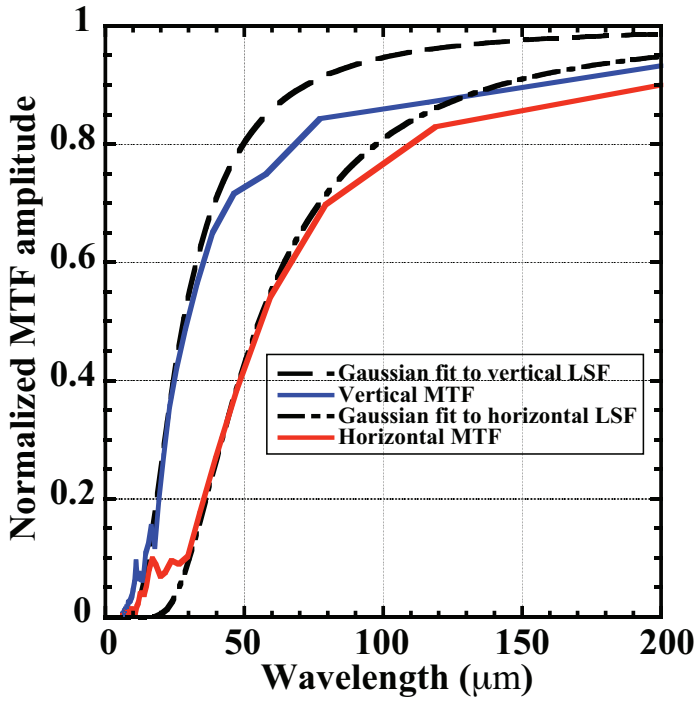

Figure 3.1: This plot shows both vertical and horizontal MTFs calculated from radiographs of vertical and horizontal razor blades placed in the target position. The dashed lines are determined by taking the Fourier Transform of a Gaussian that was fitted to the line spread function.

As the Al propagated over the foam a lateral shock was driven down into the foam, increasing the density and making the shocked foam appear darker in the radiographs.

3.3.1 Shocks in the Al flow

The most notable features in Fig. 3.2 are the dark bands appearing above the first few perturbations. These features appeared on all of the fielded perturbation sizes; however, for the 100 and 200 μm wavelengths they were less resolved. The 300 μm perturbations displayed the clearest images that suggested these structures are shock waves generated by the interaction of the Al flow and the foam perturbations. These band structures are better seen in the enlarged images in Fig. 3.3. The radiograph of a flat foam target, shown in Fig. 3.4, did not show the dark bands confirming that the perturbations interacted with the Al flow. Shocks would be expected to form

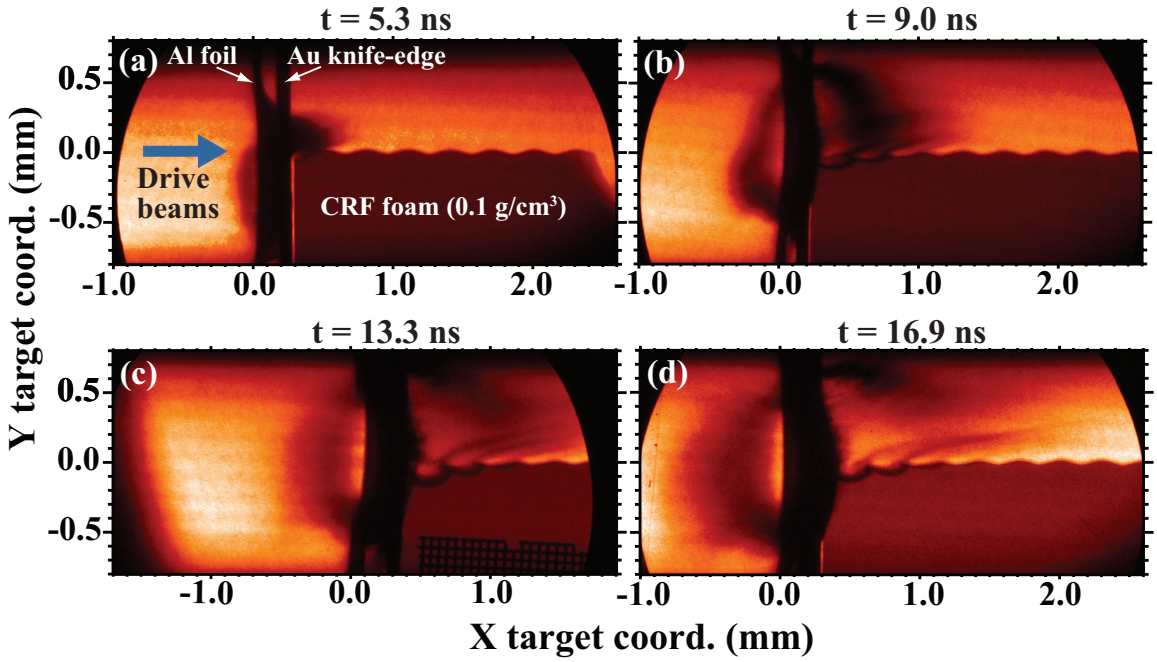

Figure 3.2: The time evolution of the target is shown here with four radiographs of four separate Nike targets. All of the targets used foam with a perturbation wavelength of 300 μm and a peak-to-valley amplitude of 30 μm. The distance between the rear of the Al foil and the front of the Au knife-edge was 100 μm. The plume extending to the left of x = 0 was Al that was reflected from the Au knife-edge. The time elapsed between the start of the drive beam pulse and the start of the diagnostic pulse is given for each image.

if the Al flow was supersonic relative to the perturbations that are initially fixed in the lab frame. The relevant Mach number here is the flow Mach number, defined by $M = \frac{v_{Al}}{c_{s,Al}}$, where v_{Al} is the velocity of the Al flow in the lab frame and $c_{s,Al}$ is the local sound speed in the Al flow. The flow is supersonic for $M > 1$.

The flow Mach number was estimated using only the experimental data. To do this the flow velocity, the internal pressure, and the density of the Al flow must be measured. The flow velocity was measured by tracking the position of the densest section of the Al flow over several radiographs taken at different times relative to the start of the drive laser. The average flow velocity was 83 $\pm$ 22 μm/ns. This measurement yielded the velocity of the bulk Al, which was slower than the high

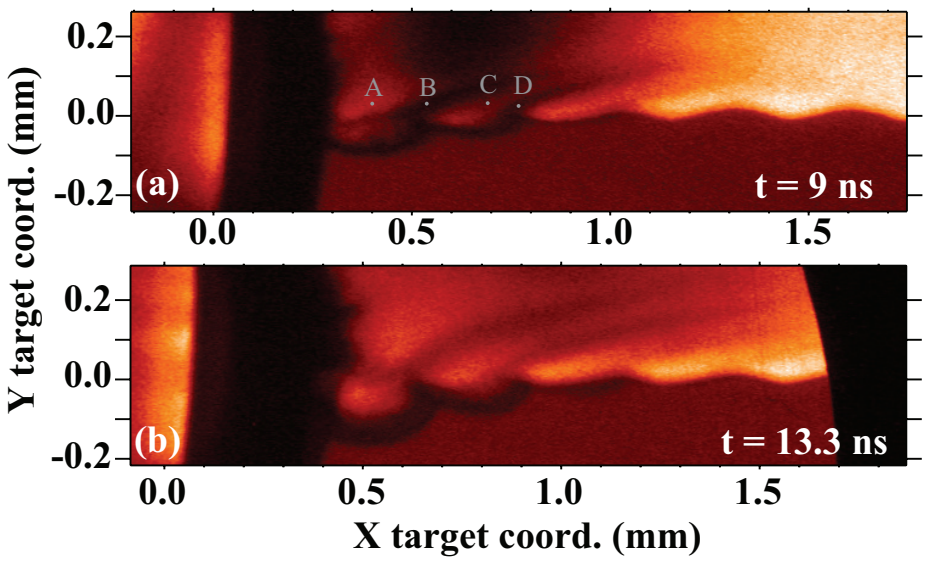

Figure 3.3: Shown here are two radiographs of the foam surface interacting with the supersonic Al flow. The upper image is an enlarged section of Fig. 3.2b and the lower image is an enlarged section of Fig. 3.2c. The dark bands seen above the perturbations are believed to be the result of shock waves, which increased the local Al density. The densities at points A, B, C, and D are 0.008 ± 0.002 g/cm^3, 0.023 ± 0.004 g/cm^3, 0.013 ± 0.002 g/cm^3, and 0.018 ± 0.003 g/cm^3 respectively. There is a visible intensity difference between points C and D. However, these absolute uncertainties indicate that the densities could be equal, which implies that the uncertainties were overestimated. In front of the Al flow, the foam surface appears blurred due to a combination of the finite diagnostic resolution and a slightly skewed diagnostic line of sight, which produces a variation in the x-ray optical path length near the foam surface.

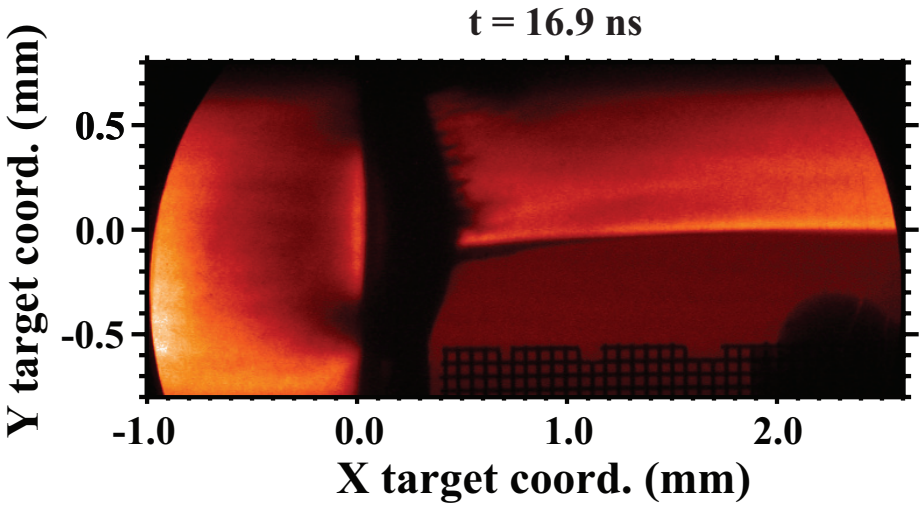

Figure 3.4: This radiograph of a Nike target with a flat foam showed no interface development, indicating that the perturbations were responsible for creating the distinct features observed in the Al flow.

velocity, lower density Al that was rapidly expanding into vacuum in front of the bulk Al. The densities of the Al and foam were calculated by using the simplified radiation equation, also known as Beer‘s law, given by

$$I = I_0 e^{-(\mu_m \rho_m z_m)} + I_b \tag{3.1}$$

where I_0 is the unattenuated x-ray source value, I_b is the background value, ρ_m is the density of material m, μ_m is the mass absorption coefficient of material m, and z_m is the width of the material m along the diagnostic line of sight, into the page of Fig. 3.2. Rearranging Eq. 3.1, the density is given by

$$\rho_m = -\frac{\ln\left(\frac{I-I_b}{I_0}\right)}{\mu_m z_m}. \tag{3.2}$$

I_b was measured from the section of radiograph that corresponded to the image of the Au foil. Thus, I_b includes the noise added during the scanning of the image plate, diffuse reflections from the crystal, and scattered x-rays from elsewhere in the vacuum chamber. The diffuse reflections and scattered x-rays were minimized by placing a

small aperture in the path of the reflected x-rays at the image distance of the x-ray source. For 1.865 keV x-rays, $\mu_{Al} = 2708$ cm^2/g and $\mu_{CRF} = 371$ cm^2/g, assuming the foam composition by percent mass was 93% C, 6% O, and 1% H. However, transmission measurements of the unshocked portions of the foam yielded $\mu_{CRF} = 520 \pm 50$ cm^2/g. The difference in μ_{CRF} is most likely due to a discrepancy in the foam composition. All of the calculations presented in this chapter take $\mu_{CRF} = 520 \pm 50$ cm^2/g. Both the thickness of the foam and the density are known to within 5% uncertainty, yet the composition of the foam could not be verified. The width of the Al flow, z_{Al}, was estimated using a different target, shown in Fig. 3.5, with the Au knife-edge orientated orthogonally to the standard target. The width of the Al was measured by finding the 50% intensity points of the intensity profile taken through the widest section of the Al. The density was assumed constant over this width and was set equal to z_{Al}. For the Al and shocked foam density measurements $z_{Al} = 600 \pm 100$ μm and $z_{CRF} = 400 \pm 50$ μm. In Fig. 3.2b the maximum density of the Al above the bands was 0.027 ± 0.005 g/cm^3. Within the experimental uncertainty, this density agrees with those measured in other radiographs at similar times.

The internal pressure of the Al was estimated by calculating the lateral shock speed in the flat foam target shown in Fig. 3.4. Assuming the pressure was constant across the Al/shocked-foam interface, the internal Al pressure at the interface was equal to the pressure of the shocked foam. The shocked foam pressure (p_{sf}) can be found by combining the shock jump equations for mass and momentum. Assuming the initial unshocked foam pressure is negligible,

$$p_{sf} = \rho_0 u_s^2 \left(1 - \frac{\rho_0}{\rho_{sf}}\right) \tag{3.3}$$

where ρ_o is the unshocked foam density, ρ_{sf} is the shocked foam density, and u_s is the foam shock velocity measured in the laboratory frame. Measuring ρ_{sf} and u_s from the flat foam target we find $u_s = 22 \pm 5$ μm/ns and $\rho_{sf} = 0.17 \pm 0.05$ g/cm^3,

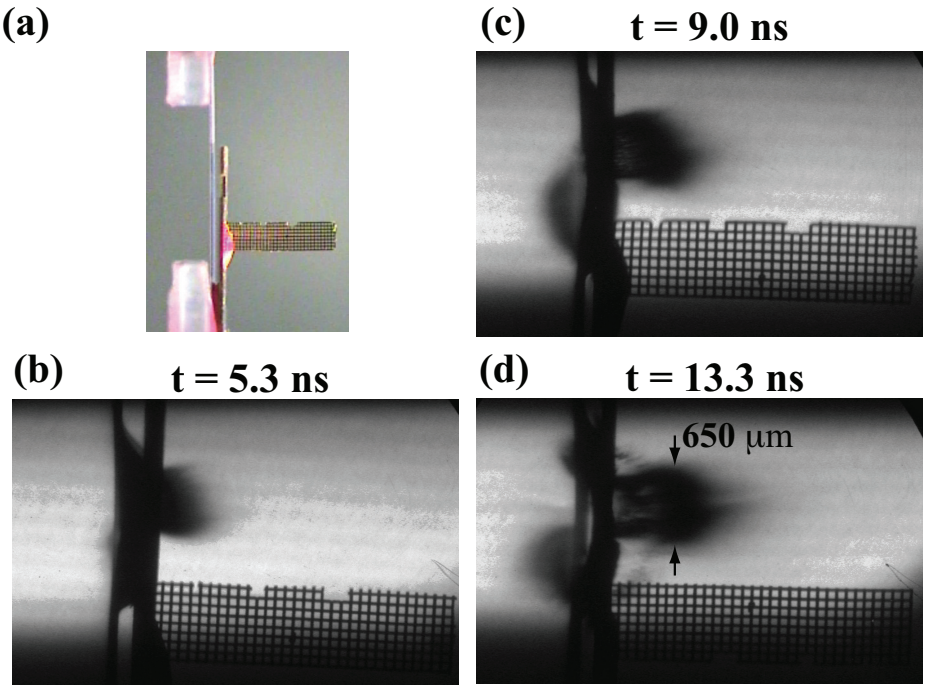

Figure 3.5: (a) This image shows a picture of a Nike target that used an Au knife-edge that was orientated orthogonally to the standard knife-edge design. The orthogonal design made it possible to measure the width of the Al flow along what was previously the z-direction in the standard design. (b) - (d) These radiographs show the Al as it flows through the orthogonal slot in the Au at various times. Each image represents results from a separate target. The laser enters from the left in each image.

which gives $p_{sf} = 0.2 \pm 0.1$ Mbar. This represents some average Al pressure since the pressure exerted on any point of the foam surface is a function of time due to the limited extent of the flow and its decompression. The polytropic sound speed in the Al flow $c_{s,Al}$ is defined by

$$\sqrt{\frac{\gamma p_{Al}}{\rho_{Al}}}, \tag{3.4}$$

where γ is the polytropic index, p_{Al} is internal pressure of the Al, and ρ_{Al} is the Al density. Assuming $\gamma = 1.4$, setting $p_{Al} = p_{sf}$ and taking $\rho_{Al} = 0.027 \pm 0.005$ g/cm3, we have $c_{s,Al} = 32 \pm 11$ μm/ns. Using the differential flow speed stated earlier (83 ± 22 μm/ns) yields a flow Mach number of 2.6 ± 1.1. Thus, the Al flow is supersonic, which supports the idea that the dark bands are the result of shock waves

in the Al flow. However, it is possible that the bands are simply composed of foam that was stripped from the perturbations in a process similar to that described by Ref. [71]. In this case, a supersonic flow of Al would not be required to form the band structures. Furthermore, the opacity of the shocked foam and the bands are similar in the radiographs, so it is not obvious which material is being observed. Therefore, the amount of foam stripped from the perturbations and its contribution to the opacity of the bands must be estimated.

To estimate the opacity contribution of the foam the amount of stripped foam mass (m_s) is first estimated for the experiment shown in Fig. 3.2b. The amount of foam affected by the lateral shock was calculated by finding the leading edge of the shock, which is defined as the location of the 50% pixel value between the shocked and unshocked foam. Then the location of the original perturbed surface was estimated. The region between the original surface and the shock front contains all the foam that has the potential to be stripped and included into the bands. Figure 3.6 delineates this area and divides it into two regions marked 1 and 2. The initial foam mass of Region 1 and 2 is 1.2 ± 0.2 μg and 0.5 ± 0.2 μg respectively.

The uncertainty is due to variations in the placement of the boundaries that define the shock position and the location of the initial foam surface. These boundaries are manually translated by small amounts until it is clear that the lines do not agree with the features in the radiograph. The uncertainty is then the difference between the mass bounded by the translated boundaries and the mass bounded by their nominal positions. In each region some of the initial mass remains compressed directly behind the shock front. The thin dark region directly behind the shock was assumed to be compressed foam with no entrained Al. The areas containing the compressed foam are shown in Fig. 3.6. For Region 1 the amount of compressed mass is 0.77 ± 0.1 μg and 0.51 ± 0.1 μg for Region 2. Here the uncertainty is dominated by the placement of the boundaries, while the contributions from small variations in I_0, I_b, and μ_{CRF}

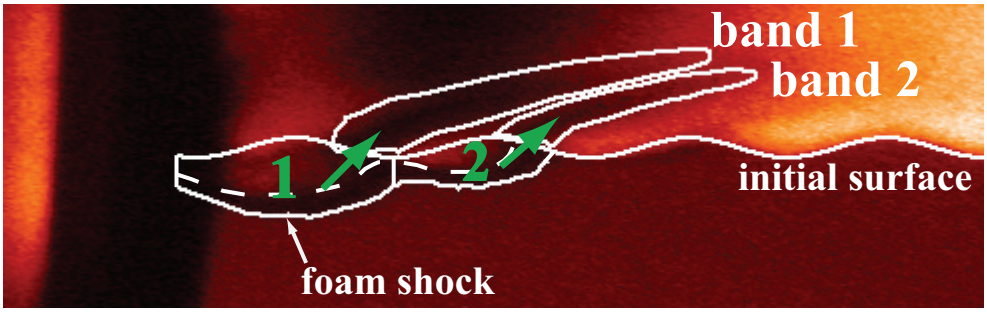

Figure 3.6: Shown here is an enlarged image of Fig. 3.2b. The overlaid lines define the various regions used in the opacity analysis. The line near the bottom of the image defines the location of the foam shock. We assumed the region between this line and the dashed line directly above it contained only shocked foam. The sinusoidal line represents the initial position of the foam surface. The region between this line and foam shock is divided into two regions labeled at "1" and "2" in the image. We assumed that the mass stripped from Region 1 and Region 2 was uniformly distributed over two respective areas labeled as "band 1" and "band 2" in the image.

are negligible. The stripped mass is then the difference between the initial mass and the remaining shocked mass. For Region 1, $m_s = 0.33 \pm 0.1$ μg and for Region 2, $m_s = 0.04$ (-0.02, +0.12) μg. We assume that the foam stripped from Region 1 only contributes to the opacity of the first band and the foam stripped from Region 2 only contributes to the opacity of the second band. This is reasonable because there does not appear to be strong mixing between the two bands.

Some spatial distribution of the stripped mass must be assumed in order to estimate its opacity contribution. The stripped foam from Region 1 was assumed to be uniformly distributed over the area labeled as band 1 in Fig. 3.6. Likewise, the stripped foam from Region 2 is uniformly distributed over the area labeled as band 2. The contribution of the foam opacity is then defined as the average ratio of the foam opacity and the total opacity for each pixel inside the area defined by the bands. The opacity contribution of the foam is then $22 \pm 7\%$ and 7 (-3, +15)% for the first and second bands respectively. Thus, we can say with some confidence that we are observing the dynamics of the Al flow when examining the bands. Furthermore, the amount of Al required to create the remaining opacity in both bands is 0.35 μg. This mass of

Al must have originated from the Al flow before the bands formed. The amount of Al mass available from the flow was 0.5 μg, which is greater than the amount required to form the opacity of the bands. This again confirms that the previous estimates of the opacity are reasonable. The opacity analysis was repeated for the radiograph shown in Fig. 3.2c. For this image the opacity contribution of the foam was 22 (-3, +7)% and 6 (-6, +12)% for the first and second bands respectively.

Overall, the experimental data suggests that the dark bands observed in the radiographs are the result of shocks in the Al flow. However, in this case, due to the limited resolution of the diagnostics, it is difficult to prove the existence of shocks using only the experimental data. We therefore turn to simulations in 3.4 for compelling evidence of their existence.

3.3.2 Interface growth

The perturbations seen in Fig. 3.2c and d show small developments that may indicate the presence of an instability mechanism. The most developed perturbations have a peak-to-valley height of 75 to 100 μm. The interface experiences a shear flow and an impulsive loading that suggests both KH and Richtmyer-Meshkov (RM) instabilities may be present. The shock wave in the foam quickly evolved into a decelerating blast wave that allowed the interface to be RT stable. Although distinct KH vortices did not appear in the radiographs, the question remains whether some component of the observed growth was due to the KH instability in its linear regime. The simplest estimation can be made by assuming that the Al and shocked foam are infinite in their spatial extents. In addition, if the fluids are inviscid and incompressible, and separated by an infinitely sharp transition layer (i.e., a velocity profile with a discontinuity at the interface) the linear growth rate is given by Eq. 2.1. Here $A = \frac{\rho_{sf}-\rho_{Al}}{\rho_{sf}+\rho_{Al}}$ where ρ_{Al} is the density of the Al flow and ρ_{sf} is the density of the shocked foam. Assuming the foam has no forward velocity, ΔU is just the Al

flow velocity equal to 83 μm/ns. Taking $A = 0.7$ and $k = 2\pi$ / 300 μm^{-1} yields γ = 0.6 ns^{-1}, which is an e-fold time (τ) of 1.7 ns. Again, this estimate assumed an abrupt velocity transition between the two fluids. However, another estimate of the KH growth can be made with an added finite velocity transition layer. Growth rates for linear velocity profiles across a stratified interface are easily calculated [63]. Here we assume the total transition layer width is equal to the peak-to-valley height of the perturbation (30 μm) and the transition layer contains a fluid with a density equal to the average of the Al and shocked foam densities. The interface deceleration is on the order of several $\mu\text{m/ns}^2$ so buoyancy effects can be neglected (i.e. the Richardson number ~ 0), and this calculation yields a slightly larger $\tau = 2.1$ ns. As expected a finite transition layer makes the interface more stable. The e-folding times for an interface with and without the velocity transition layer are plotted in Fig. 3.7. For the case without a velocity transition, both A = 0 and A = 0.7 are plotted.

In addition, the finite depth of the shocked foam can stabilize the linear KH growth. Equation 4 from Ref. [34] estimates the linear growth rate taking in account the finite depth of one of the fluids in a KH unstable interface. Using an interface with no velocity transition layer and foam fluid depths of 5, 10, 25, and 50 μm, we find $\tau = 4.5$, 3.2, 2.1, and 1.6 ns respectively. For large depths this equation becomes $k\Delta U\sqrt{\rho_{Al}/\rho_{sf}}$ since it was assumed that $\rho_{sf} \gg \rho_{Al}$. From the experiments in Fig. 3.2, the estimated foam depth is 50 μm, so the finite depth should not have a strong affect on the linear growth rate.

So far compressibility effects have been neglected. A simple dispersion relation for the linear KH compressible growth rate can be derived for an infinitely sharp transition layer with fluids of equal densities [72, 73, 74]. Equation 3.5 gives the growth rate (γ_{comp}) from this dispersion relation.

$$\gamma_{comp} = kc_s \,\text{Im}\left(\sqrt{-\sqrt{M^2+1} + \frac{M^2}{4} + 1}\right) \tag{3.5}$$

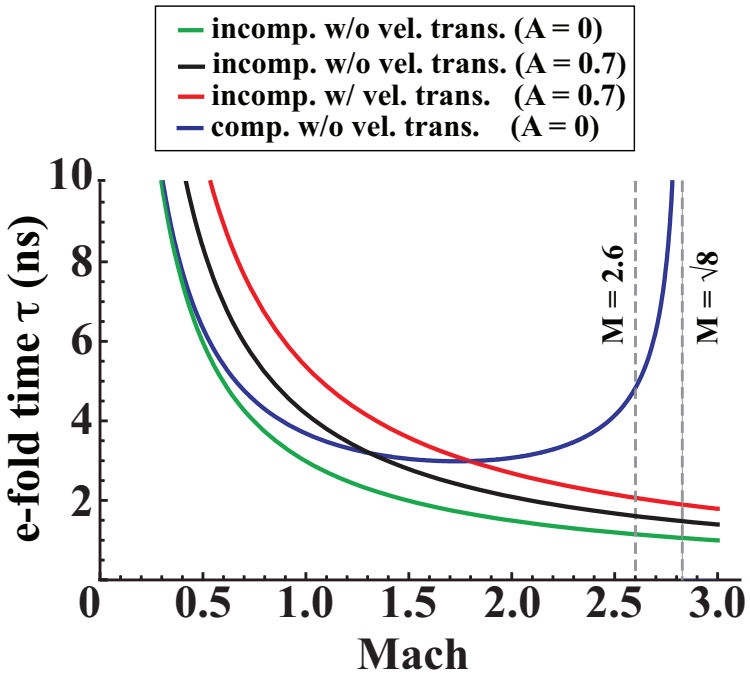

Figure 3.7: This plot compares the e-folding times predicted by four different linear KH models. The perturbation wavelength in these models was set to 300 μm. For the incompressible cases the Mach number does not appear in the dispersion relations. However, the Mach number is used here so that the incompressible models can be compared to the compressible model. For the incompressible models the flow velocity was equal to the product of the sound speed (c_s = 32 μm/ns) and the Mach number. Two of the incompressible models used the measured densities of the aluminum (ρ = 0.027 g/cm^3) and shocked foam (ρ = 0.17 g/cm^3). The compressible model had no velocity transition and assumed that the densities were the same on both sides of the interface (i.e., Atwood number A = 0).

The dispersion relation was derived for the case in which one fluid is at rest in the laboratory frame of reference. Here then c_s is the sound speed for the gas that is in motion and the Mach number M is the flow velocity divided by c_s. This is exactly how it was defined previously for the Nike target. Figure 3.7 plots the e-folding time ($1/\gamma_{comp}$) predicted by the compressible dispersion relation as a function of Mach number. For M = 2.6, c_s = 32 μm/ns, and k = 2π / 300 μm^{-1}, we find τ = 4.8 ns. This is more than factor of two greater than the e-folding values predicted by the incompressible models. Interestingly, for $M \geq 2.83$ ($\sqrt{8}$) this simple dispersion

relation has no unstable modes. In other words, a vortex sheet is always stable for $M \geq 2.83$. However, when a velocity transition layer is added two new unstable modes appear, and interface perturbations become unstable for all supersonic Mach numbers [75].

An accurate estimation of the KH growth is difficult because the Al flow was unsteady due to its limited spatial extent. However, the effective drive time (t_d) of a single perturbation can be estimated as H/v_{Al} where H is the approximate width of the densest section of Al flow and v_{Al} is the flow velocity. For Fig. 3.2b, we estimate $H \sim 300$ μm and $v_{Al} = 83$ μm/ns. The final amplitude of a perturbation is then given by $\eta = \eta_c e^{t_d/\tau}$. Here we assumed the foam perturbations are compressed by the shock in the foam to a smaller amplitude $\eta_c = f_c \eta_0$, where f_c is the compression factor. Inputting the measured foam density and shock speed yields $f_c = 0.77$ [76]. Then for $\eta_0 = 15$ μm, $H = 300$ μm, $v_{Al} = 83$ μm/ns, and $t_d = 3.6$ ns we have $\eta = 24$ μm for $\tau = 4.8$ ns and $\eta = 64$ μm for $\tau = 2.1$ ns. Thus, compressible effects are important, and for this experiment the compressible growth time ($\tau = 4.8$ ns) is considered to be the best estimate of KH growth. A more accurate estimate would be obtained if a velocity transition layer and a finite fluid depth were added to the compressible theory. These effects make estimating the growth considerably more complex and will not be discussed here.

In addition to KH, the interface may also be RM unstable due to the vorticity created when the shock in the foam was launched from the foam surface. The linear model described by Ref. [76] was used to calculate the interface growth. This represents an upper estimate of the potential growth, because here a shock was launched from the foam surface, in contrast to the standard RM geometry where a planar shock crosses a rippled interface. Less vorticity is generated in the scenario of the present experiment than in the standard RM model. Shock velocities of 10, 20, and 30 μm/ns were used in the model. For $k = 2\pi$ / 300 μm^{-1} and 10 ns of growth time we calcu-

lated growth factors (ratio of the final and initial perturbation amplitude) of 1, 1.3 and 1.8 for shock velocities of 10, 20, and 30 μm/ns respectively. Thus, for initial amplitudes of 15 μm, the final amplitudes after 10 ns are 15, 20, and 27 μm. For the 10 μm/ns shock speed the RM effect is weak enough that the compressed perturbation does not have time to grow larger than its initial amplitude. As described in 3.3.1 the estimated foam shock velocity was 22 ± 5 μm/ns. With an upper estimate of the shock speed at 30 μm/ns, the perturbation has a final peak-to-valley amplitude of 54 μm. This still falls short of the 75 to 100 μm of observed growth, which suggests the growth was not solely driven by RM effects. The total perturbation growth then has potential contributions from both KH and RM. This analysis highlights the fact that the present experiments cannot resolve the individual contributions of the KH and RM instabilities. Future experiments must consider this carefully and perhaps find ways to differentiate between these two instabilities.

3.4 Simulations

The one-dimensional, Lagrangian radiation hydrodynamics code Hyades [65] was used to simulate the drive and expansion of the Al foil. The simulations used multi-group radiation transport, average atom ionization, flux limited electron heat transport (with flux limiter $f = 0.05$), and polytropic equations of state ($\gamma = 1.4$) for the Al and parylene. The density and velocity profiles are shown in Fig. 3.8. The maximum density predicted at t = 9 ns by Hyades is 0.9 g/cc, which is 30 times larger than the observed density.

We would expect 2D and 3D effects to decrease the observed density. In particular, the constricting nature of the knife-edge slot will decrease the mass flow, while the expansion of the Al in the y-direction will decrease the areal mass density along the diagnostic line of sight. Observing the flow at a point fixed at x = 0.5 mm, Hyades predicts that the Mach number is large (> 10) in the low-density Al expanding in

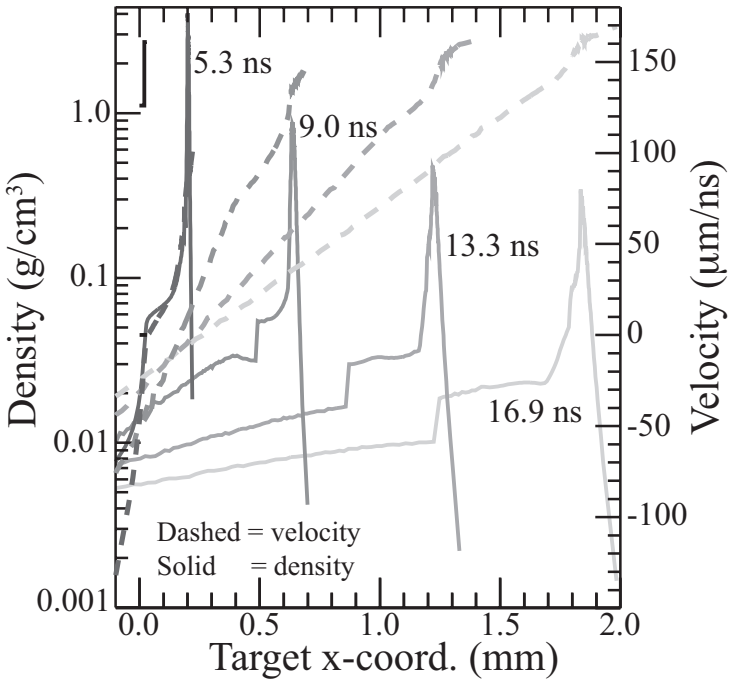

Figure 3.8: This plot shows the simulated one-dimensional density and velocity profiles of the expanding Al foil at four different times. Here 1D Hyades was used to simulate the interaction of the Nike drive beams with a 10 μ Al foil coated with 20 μm Parylene-N on the laser irradiate side. The short vertical line in the upper left of the plot marks the initial position and density of the foil at t = 0. The discontinuity seen near the center of the profile is an artifact of the code. It occurs at the boundary of the Parylene-N and Al.

front of the higher density section. This high Mach number lasts for less than one ns, before the Mach number rapidly decreases to ~ 2 for 4 to 5 ns. After this time Hyades predicts a subsonic flow.

The pressure, velocity, and density of the Hyades output were sampled 50 μm from the rear of the Al foil, in the center of the vacuum gap. These values served as the inflow conditions at the left boundary of a separate two-dimensional simulation with FLASH [66]. FLASH is an Eulerian, adaptive mesh code that uses a polytropic equation of state. The simulations presented here assumed $\gamma = 1.4$. FLASH does not have the capability of simulating the effects of an incident laser, so Hyades must be used to generate the initial conditions. We found that FLASH simulations appeared

more like the data when the vacuum gap between the Al and the gold knife-edge was increased to 500 μm. This was 400 μm greater than the vacuum gap used in the experiment. The larger gap allowed more time for the Al to decompress before it encountered the knife-edge. The larger gap also introduced a timing offset between the simulations and the experiment. We effectively compensated for the timing offset by matching the position of the Al with respect to the knife-edge in both the simulation and experiment. In this way, we attempted to reproduce a similar evolution of the foam surface.

Figure 3.9 shows the density field from the FLASH simulations with 0.5 μm resolution. The simulations were taken at t = 15 ns and t = 20 ns to match the data at t = 9 ns and t = 16.9 ns. At the later time, it was difficult to locate the Al in the radiograph because the rapid decompression of the flow made the Al relatively transparent to the backlighter x-rays. The simulations clearly show the formation of the dark bands near each perturbation that are similar to those seen in the experimental radiographs.

The density, velocity, and pressure experience discontinuous jumps at the suspected shock location, thus proving that shocks are present in the simulations. These simulations also show that the bands are composed entirely of Al, which indicates that there was no mixing of the Al and foam in the simulations. The 2D FLASH simulations over-predicted the density of the Al, which is again most likely the result of using 1D initial conditions and missing 3D effects. The simulated material temperatures, densities, pressures, and average ionization states are shown in Table 3.1 for the positions marked by the lettered points shown in Fig. 3.9a and b. These points correspond to areas of shocked foam, bulk Al, and low-density Al. The shocked foam locations A and D are positioned directly behind the shock. The average ionization state Z_{TF} was calculated using the analytical fits to the Thomas-Fermi equations found in Table 2.1 of Ref. [77]. The average ionization state Z_{Saha} was calculated

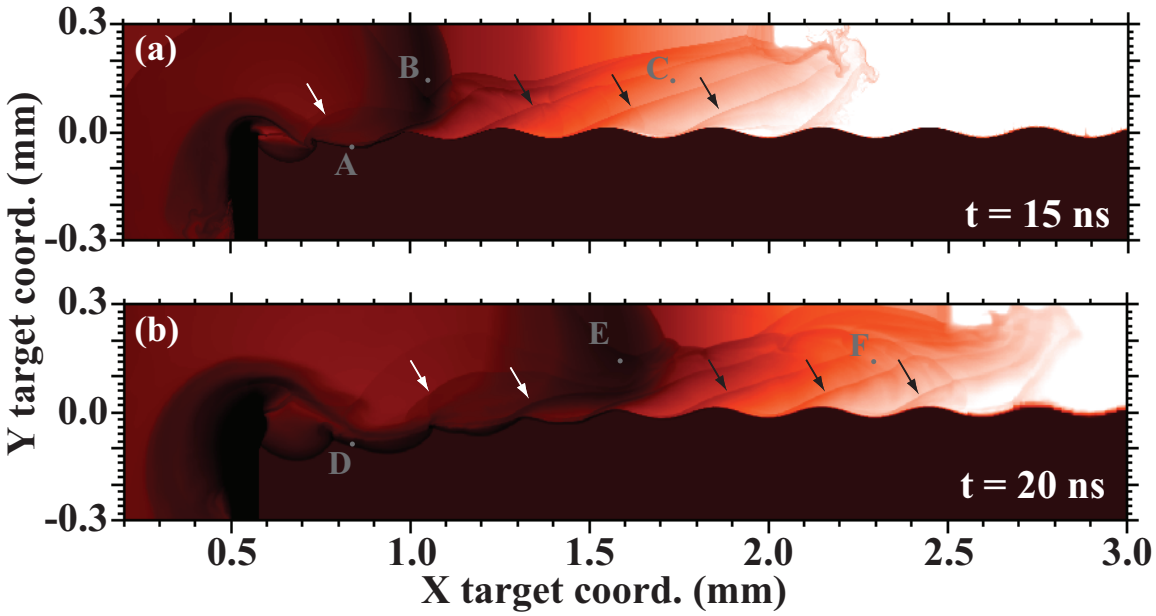

Figure 3.9: Two-dimensional FLASH simulations at t = 15 and 20 ns showed the development of shock waves near the perturbations. The arrows indicate the location of several of the shocks. The black arrows point to high Mach number shocks that have a planar shape, and the white arrows point to the curved bow shocks that formed in the lower Mach number region behind the bulk of the Al. This simulation used a 500 μm vacuum gap, so the front of the Au knife-edge is located at x = 0.5 mm. The origin of the y-axis lies along the center of the perturbation, while x-axis origin is set to the left boundary of the simulation domain. At this boundary the Al flowed into the domain with a pressure, velocity, and density calculated by 1D Hyades. These simulation times were chosen such that position of the Al coincides favorably with that from the experiment at t = 9 and 16.9 ns.

from the Saha equation for a hydrogen like ion found in Ref. [78]. The ionization states of the shocked foam and the bulk Al are small enough that the opacities are not expected to vary from the cold opacity values.

The FLASH simulations show the effects of the Mach number on the shape of the shocks formed around the foam perturbations. For high supersonic Mach numbers, or small perturbations, the shock will be planar and will remain inclined close to the foam. The angle between the shock and the perturbation can be estimated from the oblique jump conditions, the results of which are typically shown in a plot known as a

	A (foam)	B (bulk Al)	C (low-denisty Al)	D (foam)	E (bulk Al)	F (low-density Al)
$P(Mbar)$	0.10	0.10	3.0×10^{-5}	0.07	0.061	2.8×10^{-5}
ρ (g/cm^3)	0.48	0.30	7.0×10^{-6}	0.50	0.17	5×10^{-6}
$T(eV)$	2.8	8.8	120.6	2.2	10.4	156.0
Z_{TF}	1.6	2.4	8.3	1.5	2.5	9.2
Z_{Saha}	0	1.0	10.7	0	1.0	12.4

Table 3.1: This table displays the pressure (P), density (ρ), material temperature (T), and the estimated average ionization states (Z_{TF} and Z_{Saha}) of the lettered positions shown in Fig. 3.9a and b. Except for Z_{TF} and Z_{Saha}, all of these values were taken directly from the FLASH simulations. The values for Z_{TF} and Z_{Saha} were calculated from analytical models using the FLASH density and temperature values. No solutions of the hydrogenic Saha equation existed for points A and D, so it is assumed that the ionization is equal to 0 for these locations according to the Saha model.

shock polar [79]. However, if the Mach number decreases to a lower supersonic value, or equivalently the perturbation becomes steeper (i.e., becomes a greater obstacle to the Al flow) as a result of the interaction with the Al, the shock wave will become curved and will stand off at a greater distance from the perturbation. This type of shock is frequently referred to as a detached or bow shock. The transition to a bow shock occurs when the oblique jump conditions cannot be satisfied by a single planar shock. In general, by observing the shape and location of the shocks in a supersonic flow the Mach number can be estimated if the experimental geometry is well defined.

We can estimate the Mach number when this transition occurs for the experiments presented here. The perturbations are approximated as a linear wedge with an opening angle (θ) equal to the slope of a sine wave at the inflection point (see Fig. 3.10.

For a 300 μm wavelength with a 15 μm amplitude this gives $\theta = 18°$. Then solving the oblique jump equations for a wedge with $\theta = 18°$, we find that for $M > 2$ we would expect a planar shock to form around the perturbations as shown in Fig. 3.10a.

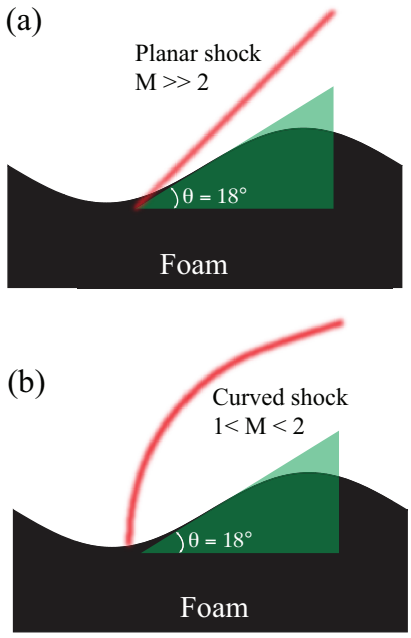

Figure 3.10: By approximating the perturbation shape as a planar wedge, the shape of the shock yields information about the Mach number of the flow. The drawing is to scale.

Therefore, the low density, high Mach number Al flow in front of the bulk will generate planar shocks around the perturbations. Evidence of these planar shocks appear on the right most affected perturbations in the radiographs of Fig. 3.3, Fig. B.17 and the FLASH simulations shown in Fig. 3.9. The FLASH simulations predict Mach numbers between 6 and 10 in these regions. The shocks increase the local density of the flow and cause the Al to become visible while the surrounding Al appears relatively transparent. For $1 < M < 2$ we would expect curved shocks with a larger stand-off distance to form as shown in Fig. 3.10b. This appears to happen behind the bulk Al where the Mach number has decreased and the foam perturbations have steepened. In these regions the FLASH simulations predict Mach numbers between 1 and 3. Further away from the foam surface the angle of Al shock approaches the Mach angle, which is equal to $sin^{-1}(1/M)$. This result can be derived from elementary gas dynamics as illustrated by the solution to the "wavy-wall" problem with a supersonic

flow [80]. The two right most perturbations in the simulation in Fig. 3.9b clearly show planar shocks that have inclinations that agree with the Mach angle predicted by the simulations.

3.5 Conclusions

Shear layers and the associated Kelvin-Helmholtz instability play important roles in the evolution of HED plasmas, which are relevant to ICF and astrophysical systems. The experiment presented here demonstrates the development of a supersonic shear layer (Mach = 2.6 $\pm$ 1.1) formed between a laser driven Al plasma and a rippled, shocked foam surface. Using only measured quantities we showed that the characteristic features of the flow are related to shockwaves that form in response to the interaction of the supersonic flow with the foam perturbations. Preliminary 2D FLASH simulations confirm that indeed shocks, with structure similar to those observed in the experiment, will form in this environment. In addition, analytical models for compressible KH and RM growth, predict that both types of instabilities can contribute to the growth of the interface perturbations. This makes it difficult to distinguish between these instabilities. Future experiments should aim to accurately quantify the contributions from the KH and RM growth. Furthermore, the opacity difference between the fluids involved in the experiment should be made large enough so that it is easy to identify the fluids in the radiographs. Imaging with harder x-rays is one possible technique to accomplish this in the future.

CHAPTER IV

Observation of a Kelvin-Helmholtz Instability in a High-Energy-Density Plasma on the Omega Laser

4.1 Introduction

This chapter discusses the results and analysis of a KH experiment carried out on different laser facility that delivered more energy than the Nike laser. This experiment used the Omega laser, along with a different target, in order to generate the KH instability. In this case the Omega laser created an unstable plasma shear layer by driving a blast wave along a plastic surface with sinusoidal perturbations. In response to the vorticity deposited and the shear flow established by the blast wave, the interface rolls up into large vortices characteristic of the KH instability. The experiment used point projection x-ray radiography at 5.18 keV to image the evolving target. This experiment was the first to capture well-resolved images of KH vortices in a high-energy-density plasma.

4.2 Experimental setup

The experiments presented here used rectangular, beryllium shock tubes to improve the planarity of the experiment by reducing the lateral expansion of material. The shock tubes had interior dimensions of 1.0 mm (wide) by 2.0 mm (tall) with

side wall thicknesses of 0.200 mm and top and bottom wall thicknesses of 0.500 mm. The lengths of the shock tubes were 4.0 mm. Inserted into each shock tube were two blocks of material each measuring approximately 1.0 x 1.0 x 4.0 mm. The upper block was made from carbon-resorcinol-formaldehyde (CRF) foam ($C_{1000}O_{48}H_{65}$, $\rho = 0.100 \pm 0.005$ g/cm^3 and average cell size 0.02 μm) while the lower block was composed of a vertical composite of three smaller blocks. The outer two of these blocks were made from polyamide/imide plastic ($C_{22}H_{14}O_4N_2$, $\rho = 1.42$ g/cm^3, trade name = Torlon), each measuring 0.40 x 1.0 x 4.0 mm, while the smaller, center block measured 0.20 x 1.0 x 4.0 mm and was made from 3% iodinated polystyrene ($C_{50}H_{47}I_3$, $\rho = 1.45$ g/cm^3). Polyamide/imide was used because it was easier to machine than standard polyimide. We will refer to the iodinated polystyrene block as 'CHI' and the polyamide/imide block as 'PAI'. Identical single-mode sinusoidal perturbations with $\lambda = 400$ μm and peak-to-valley amplitude = 60 μm were machined into one of the long faces of the CRF and PAI/CHI blocks using a diamond turning lathe. The two blocks are mated along the perturbed side and then mounted in the shock tube such that blocks were flush with both ends of the tube. Hurricane describes the design of the shock tube components of this target [57]. One end of the shock tube was covered with a 30 μm thick polystyrene (C_8H_8, $\rho = 1.05$ g/cm^3) ablator. On top of the ablator was a 50 μm thick Au washer. The washer had an outer diameter of 2.5 mm, with an interior, square cutout that was 1.0 x 1.0 mm. The Au washer was attached to the ablator such that it was aligned with the center of the CRF block. Attached to the front of the shock tube, and centered on the Au washer, was a large conical shield that prevented the detector from being exposed to the radiation emitted from the laser-ablated plasma. The shield was machined from a single piece of acrylic rod and was approximately 6.5 mm tall, 1 mm thick, and had an opening angle of 145°. A wedge-shaped piece of 50 μm thick Au foil was mounted to the exterior of the shield to further protect the detector. Before it was attached to the shield both sides of the

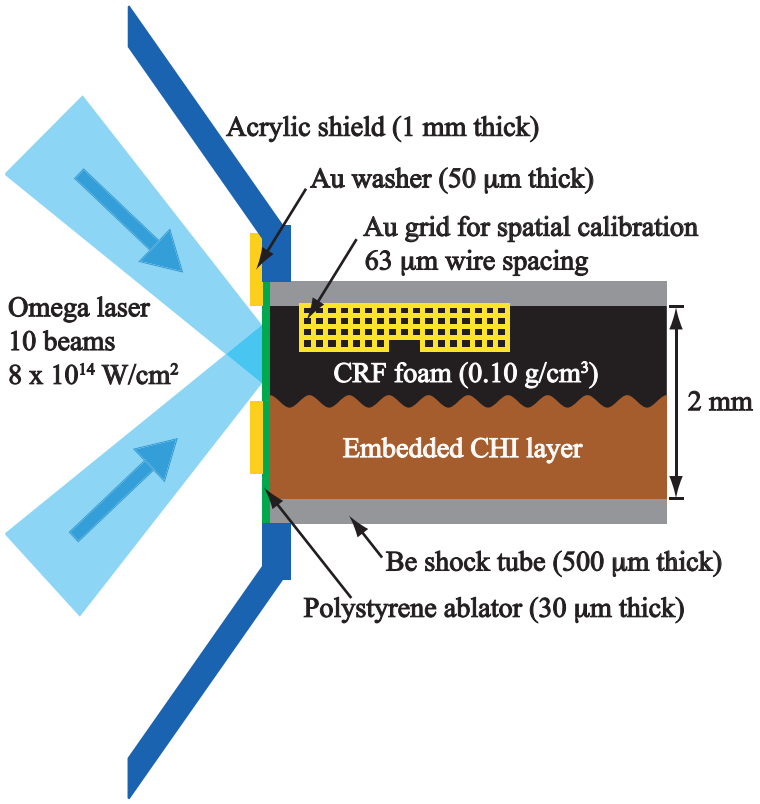

Figure 4.1: A cross-sectional view of the Omega Kelvin-Helmholtz target. The sinusoidal perturbation had a wavelength of 400 μm and a peak-to-valley amplitude of 60 μm. The Au grid was attached to the outside of the shock tube, but it is shown here for clarity.

Au wedge were coated with a few microns of plastic by applying polyvinyl alcohol (PVA) with a small paint brush. See Fig. 4.1 for a cross-sectional diagram of the target. Figure 4.2 shows pictures of the shock tube and the shock tube mounted in the conical acrylic shield.

The experiments were performed at the Omega laser facility at the Laboratory for Laser Energetics, University of Rochester [17]. The laser (Nd-glass, $\lambda = 0.351$ μm) delivered 4.3 $\pm$ 0.1 kJ to the target by overlapping ten drive beams onto the ablator, centered in the square cutout of the gold washer. Each beam had a temporal profile with 100 ps rise and fall times, a nominally flat top, and a full width at half maximum of 1.0 ns, and had an intensity profile whose shape is described by $exp[-(r/430\mu m)^{4.7}]$, where r is the distance from the center of the profile. The peak

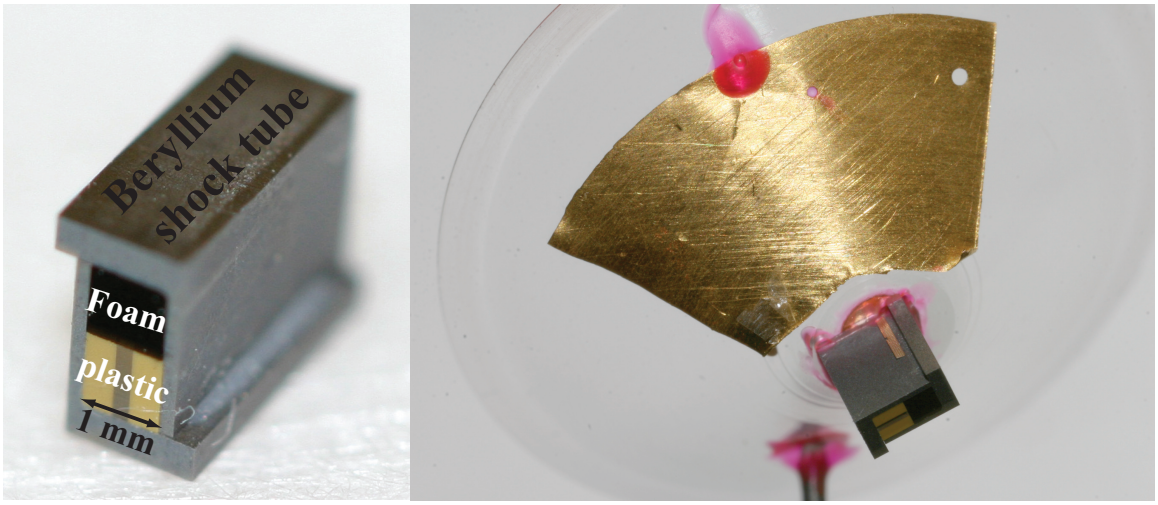

Figure 4.2: On the left is a picture of the Be shock tube that contained the foam and plastic blocks. The thin stripe seen in the center of the plastic block is the CHI layer. On the right is a picture of the shock tube mounted in the large acrylic shield. The rear (i.e., the end not irradiated by the laser) of the target is seen in this picture. The large Au wedge shielded the diagnostic from x-rays that were emitted by the laser ablated plasma. The pink material is a UV curing epoxy that was used to secure each component.

intensity of all ten overlapped beams was 8 x 10^{14} W/cm^2. The low intensity wings of the laser spot were masked by the Au washer, which prevented the disruption of the PAI/CHI blocks and the surrounding Be shock tube.

X-ray radiography was used to diagnose the target evolution at t = 25, 45, and 75 ns with respect to the start of the primary laser pulse. For each target shot only a single radiographic image at one of the specified times was captured. At the desired time interval an additional three beams, each with a nominal energy of 450 J, a 1 mm diameter spot size, and a temporal pulse shape like that of the drive beams, were overlapped onto the rear of a 200 x 200 x 5 μm V foil attached to a 2 x 2 mm polystyrene substrate. The laser-heated V plasma generated x-rays from the He-α transition (5.18 keV). Some x-rays propagated through the remaining solid V foil and through a tapered (20 to 35 μm diameter) pinhole aperture in a 50 μm thick Ta substrate (5 x 5 mm) located 500 μm from the V foil and 10 mm from the center

of the shock tube. The V x-rays transmitted through the target were incident on a single piece of Agfa D7 film, which was shielded by a 13 μm thick V foil in order to filter out lower energy x-rays from the continuum emission. The film was located 228.6 mm from the shock tube center, yielding a target magnification ~ 23. The film was later scanned with a microdensitometer that produced 22 μm square pixels. The inherent spatial resolution of the scanned image corresponds to the resolution element established by the pinhole size. The effective exposure length of the film was set by the temporal duration of the x-ray emission from the V foil, which was assumed to be equal to the duration of the laser pulse (1 ns). If shorter pulse durations are used then the finite ionization and recombination times of the electrons must be considered. Due to the well matched binding energy of the Iodine $L_1 2s$ electrons (5188 eV) and the energy of the V x-rays, nearly all of the 5.18 keV x-rays were absorbed in the CHI layer, with a 1:200 transmission contrast between the CHI and the surrounding Be and polyimide layers. Hence the CHI effectively served its intended purpose as a tracer layer in the flow by concentrating nearly all the opacity of the target in the center of the shock tube.

4.3 Experimental results

The drive beams irradiated the polystyrene surface and created a large ablation pressure (~ 50 Mbar) that was maintained while the laser was on. This large pressure launched and supported a shock into the polystyrene and the CRF foam. When the laser drive ended, a rarefaction wave was launched from the ablation surface and propagated to the shock front, which subsequently developed into a decelerating blast wave. The blast wave compressed, heated, and imparted forward momentum to the CRF foam, which led to the high-speed flow of ionized CRF plasma. At the CRF/CHI interface, the blast wave was refracted into the CHI where it continued to propagate as a transmitted shock in a direction nearly orthogonal to the blast wave. It was thus

unable to impart significant forward velocity to the CHI. Consequently, a velocity gradient developed and vorticity was deposited at the interface.

A time sequence of three radiographs in Fig. 4.3 shows the development of vortices that were initiated from the sinusoidal perturbations, and later driven to large amplitudes by the flow of CRF plasma that was created by the blast wave. Immediately after the blast wave passed the crest of a perturbation, mass appeared to be stripped in a process perhaps similar to that described by Hansen et. al. [71]. Reflected shock waves that further increase the local density are seen emanating from the perturbation behind the blast wave in Fig. 4.3a and the right most perturbation in Fig. 4.3b. In Fig. 4.3c the structure seen in the cores appeared to dissolve in the most developed roll-up, which may indicate the beginnings of a transition to turbulence. The evolution of the interface is similar to that of previous gas shock tube work, which involved oblique membranes separating gases of different densities [42, 81, 82]. However, in contrast to the present experiment, sinusoidal initial conditions were not implemented, and geometries where the shock wave and interface are orthogonal were not investigated in those experiments.

Measurements of the blast wave position in Fig. 4.3a indicate that it had an average speed of 60 $\pm$ 8 μm/ns. As the blast wave satisfies the requirements for self-similar behavior, its time-dependent position $X(t)$ can be modeled by a one-dimensional self-similar, planar blast wave in a polytropic gas with $\gamma = 1.4$. In this case, $X(t)$ and the density, velocity, and pressure profiles are described by Eq. 4.2–4.5 [83]. $\dot{X}$ is the velocity of the leading edge of the blast wave. The velocity, pressure, and density profiles from these equations are shown in Fig. 4.4a. The Mach number of the flow was computed from these profiles and is given by Eq. 4.6. The Mach

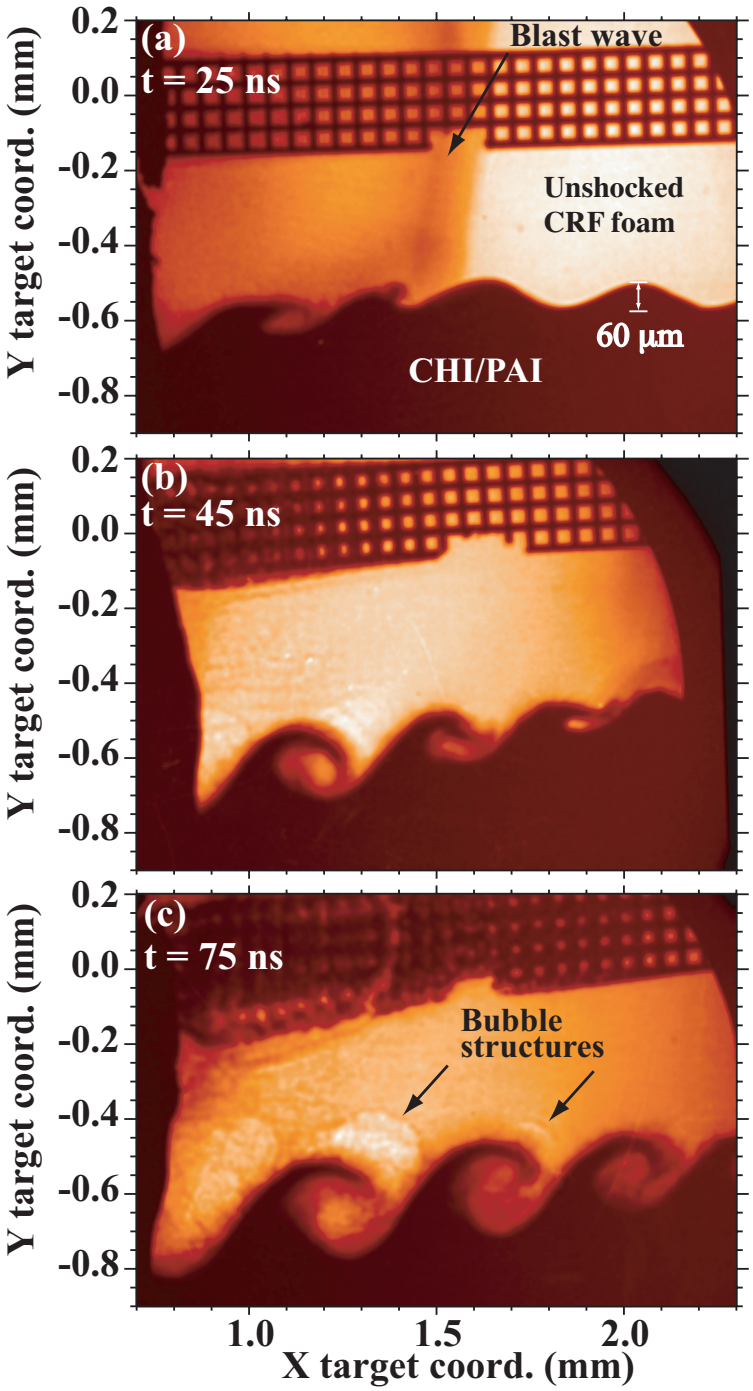

Figure 4.3: X-ray radiographs of three identical targets that show the formation of large Kelvin-Helmholtz roll-ups. These radiographs were captured at 25 ns (a), 45 ns (b), and 75 ns (c) after the start of the drive beam pulse. Here the origin of the x and y-axes was defined by the nominal position of the drive beams on the polystyrene ablator. The placement of the axes on the images is accurate to within 10%. The Au grid was distorted by the blast wave when it broke out from the inside of the shock tube and struck the grid. These images are displayed with no post processing.

number profile is shown Fig. 4.4b.

$$\xi(t) = x/X(t) \tag{4.1}$$

$$X(t) = At^{3/5} \tag{4.2}$$

$$\rho(\xi) = \rho_o q(\xi) = \rho_o 6(5-4\xi)^{-5/2} \tag{4.3}$$

$$u(\xi) = \dot{X} v(\xi) = \dot{X}\frac{5}{6}(2\xi - 1) \tag{4.4}$$

$$p(\xi) = \rho_o \dot{X}^2 \pi(\xi) = \rho_o \dot{X}^2 \frac{5}{6}(5-4\xi)^{-3/2} \tag{4.5}$$

$$M(\xi) = \frac{u}{\sqrt{\frac{1.4p}{\rho}}} = 1.89\left[\frac{2\xi - 1}{\sqrt{5-4\xi}}\right] \tag{4.6}$$

The constant A was determined by the position of the blast wave in Fig. 4.3a and is

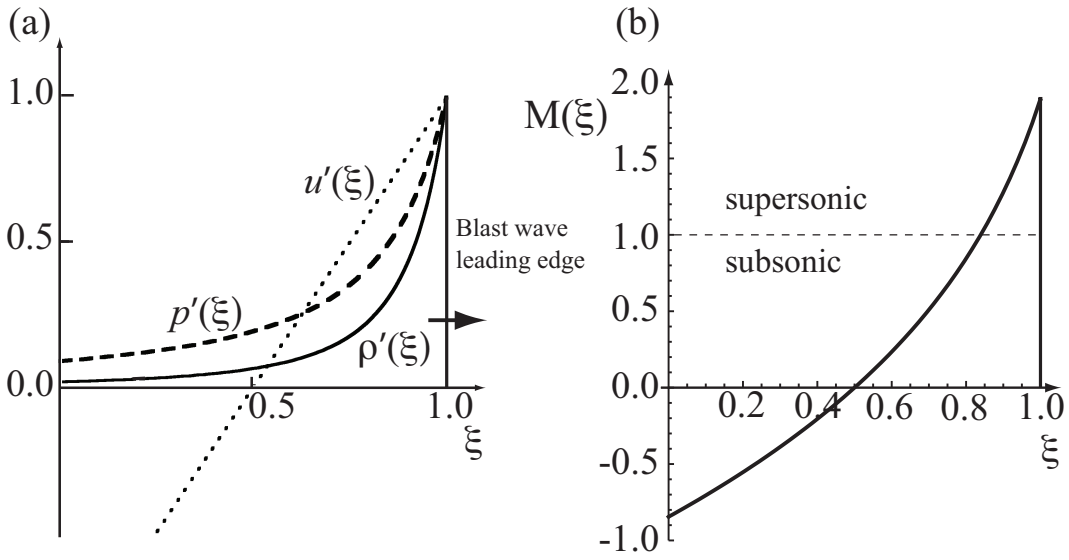

Figure 4.4: (a) Normalized density ($\rho'(\xi)$), pressure ($p'(\xi)$), and velocity ($u'(\xi)$) profiles for a 1D self-similar, planar blast wave in a polytropic gas with $\gamma = 1.4$ [83]. Each profile was divided by its maximum value, which occurs immediately behind the leading edge. Thus, $\rho'(\xi) = \rho(\xi)/[6\rho_o]$, $u'(\xi) = u(\xi)/[(5/6)\dot{X}]$, and $p'(\xi) = p(\xi)/[(5/6)\rho_o \dot{X}^2]$. (b) Mach number of the flow computed from the self-similar variables as given by Eq. 4.6.

equal to 220 ± 30 μm/ns$^{3/5}$. Using this equation we can estimate the time at which the blast wave passed each of the perturbations. Figure 4.5 shows the height of the

perturbation as a function of the time elapsed since the leading edge of the blast wave was centered on the crest of a perturbation. Thus, the first four points are from

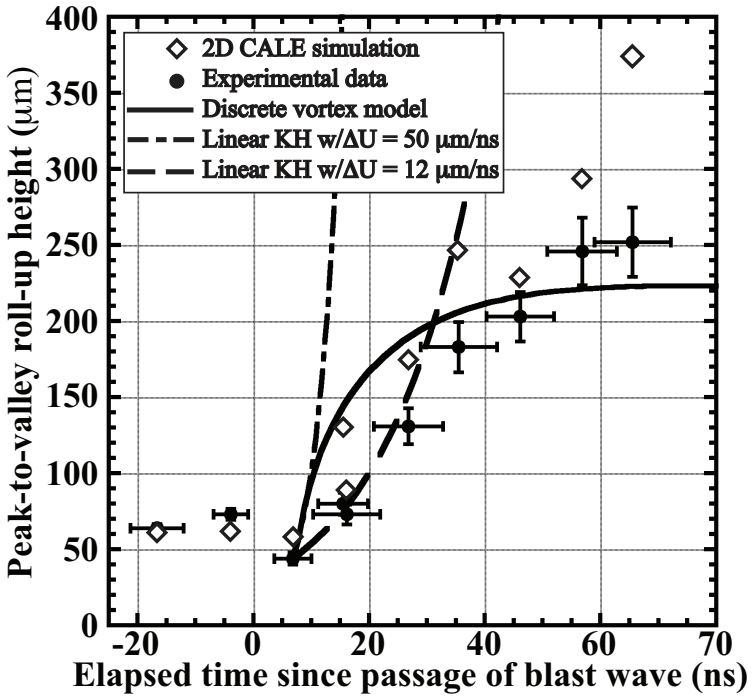

Figure 4.5: Experimental measurements of the peak-to-valley KH roll-up heights (observed over multiple targets) compared with several analytical models. All models assume the growth starts from the measured compressed perturbation height of 44 μm. The 2D CALE data points were estimated from the simulations presented in Ref. [58].

Fig. 4.3a, the next three are from Fig. 4.3b, and the next three are from Fig. 4.3c.

4.3.1 Estimating the shock compression of the foam

In this section the maximum density achieved by the compression of the blast wave (as seen in Fig. 4.3a) is measured. The maximum density is of particular interest because it can be used to extract further information such as the post-shock velocity and pressure. First a relatively simple, straight forward density measurement is described, and then a more sophisticated technique is demonstrated. In the simple approach the minimum pixel intensity value (I_{bw}) was extracted from an averaged horizontal lineout of the blast wave seen in Fig. 4.3a. The pixel intensity value from

the unshocked foam ahead of the blast wave was also recorded and assigned to the variable I_{unshk}. The maximum density of the foam in the blast wave (ρ_{bw}) is then given by Eq. 4.7.

$$\rho_{bw} = \rho_{unshk} + \frac{\ln\left(\frac{I_{unshk} - I_b}{I_{bw} - I_b}\right)}{\mu_{CRF} z_{CRF}} \tag{4.7}$$

Here μ_{CRF} is the mass absorption coefficient for CRF foam, z_{CRF} is the thickness of the CRF foam along the diagnostic line of sight, ρ_{unshk} is the density of the unshocked CRF foam, and I_b is the background pixel intensity value. An average pixel value from the left most portion of Fig. 4.3a served as the background intensity value. In this portion of the image the 50 μm thick Au foil entered into the field of view and was assumed to be completely opaque to the entire spectrum of x-rays. In Eq. 4.7 it was assumed that the thicknesses (z_{CRF}) of the shocked and unshocked foam were equal, and the Be areal mass from the shock tube remained constant along the diagnostic line of sight. In addition, it was assumed that the backlighter x-ray spectrum was monochromatic (i.e., all of the detected x-rays had an energy equal to 5.18 keV), which permitted the use of a single value for μ_{CRF}. Taking $\rho_{unshk} = 0.1$ g/cm^3, z_{CRF} = 1.0 mm and $\mu_{CRF} = 17.7 \pm 2$ cm^2/g, we find $\rho_{bw} = 0.39 \pm 0.05$ g/cm^3.

This simple density measurement did not account for the finite resolution of the diagnostic or the blurring due to the motion of the blast wave during the $\sim$ 1 ns exposure. Furthermore, if the leading edge of the blast wave was non-planar or tilted in the third dimension the areal mass along the diagnostic line of sight will be decreased. All of these effects work to smear out the intensity distribution in the image plane, and thus a lower density will be inferred if these effects are not taken into account. Therefore, the previously estimated $\rho_{bw} = 0.39 \pm 0.05$ g/cm^3 is a lower bound for the maximum density that results from the blast wave compression.

The more sophisticated measurement attempts to model all three smearing effects in order to infer the density at the leading edge of the blast wave. First, the motion

blurring and finite resolution effects are modeled, and then the non-planarity and tilting (i.e., the shape and orientation) effects are added. A 3D model of the blast wave was constructed using the density profile from the self-similar result (Eq. 4.3) with $\rho_o = 0.1$ g/cm^3. This 1D density profile was used to create a 3D array of mass values that represented the foam at t = 25 ns. The x-ray attenuation of the mass array was calculated using Eq. 3.1. A 2D intensity array was then generated by projecting the transmitted x-rays onto a simulated image plane. Figure 4.6f shows a section of the experimental blast wave taken from Fig. 4.3a, while Fig. 4.6a shows the 2D intensity array from the modeled blast wave before any of the blurring effects were added.

The effect of motion blurring can easily be included in this model by discretizing the exposure. During the exposure time the blast wave propagated through a continuous stream of x-ray photons. This stream of photons can be broken down into discrete packets with each packet imaging the blast wave at a slightly different time. The target is exposed to a total fluence equal to I_0, which is taken as the unattenuated source value used previously. The intensity of the source was assumed to be constant for the duration of the 1 ns exposure. The exposure is divided into m intervals so that the total signal collected (I) by a pixel in the image plane is given by Eq. 4.8,

$$I = \frac{I_0}{m} \sum_{n=0}^{m} \left[e^{-\mu_{CRF} z_{CRF} \rho(\frac{t_e n}{m})} \right] + I_b \tag{4.8}$$

where t_e is the exposure length, and $\rho\left(\frac{t_e n}{m}\right)$ is the time dependent density function of the foam that occupies the line of sight of a particular image plane pixel. The other variables have the same definitions as described previously for Eq. 4.7. Equation 4.8 was implemented numerically by translating the modeled blast wave in discrete steps within the 3D array of mass values. The distance of these steps was equal to $v_{bw}\frac{t_e}{m}$, where v_{bw} is the velocity of the leading edge of the blast wave and was set equal to

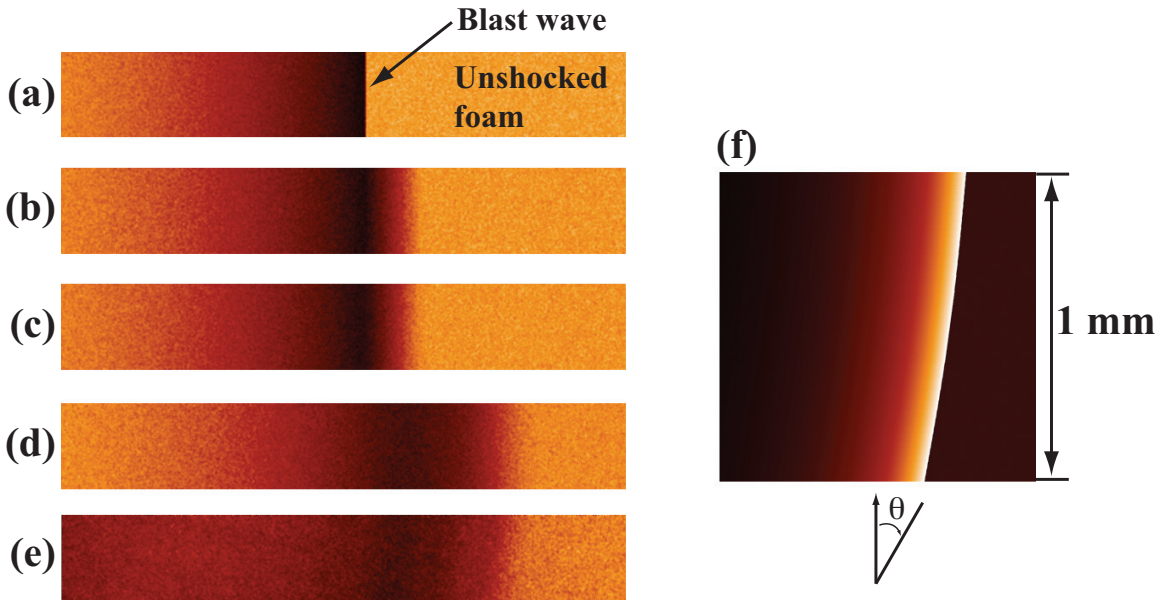

Figure 4.6: (a) This image represents the signal transmitted through a 3D array of mass values that modeled the distribution of compressed mass in the foam at t = 25 ns. Here the density profile with a maximum compression of 6.5 was used to generate the 3D array. (b) Motion blurring due to the translation of the blast wave during the exposure was added to the image in (a). (c) The image in (b) was convolved with a 2D Gaussian PSF (σ = 6.5 μm) in order to model the effect of finite diagnostic resolution. (d) The blast wave was tilted by setting $\theta = 7.8°$ and then shaped with a half-wavelength of a sinusoid (λ = 2 mm and amplitude = 15 μm) before motion blurring and finite resolution effects were added. (e) This is a small section of the the experimental blast wave taken from Fig. 4.3a. (f) Shown here is an image of a horizontal cross-section of the 3D mass array that shows the shape of the leading edge. In this image the brighter regions correspond to higher density. In order to create more realistic looking images Poisson noise was added to all of the images, except (f), after the blurring effects were included.

the measured value 60 μm/ns. We assumed that the variation in velocity during the exposure is negligible. At each time step a pixel collects signal. The amount of signal collected depends on what density (or equivalently what areal mass) the pixel "sees" during that time step. As stated by Eq. 4.8, the total amount of signal collected by a pixel is the sum of the contributions of each of the shorter exposures. Figure 4.6b shows the result of the motion blurring after it was applied to the ideal blast wave from Fig. 4.6a. Compared with the experimental image the motion-blurred blast wave model under predicts the amount of blurring observed at the lead edge.

Next, the diagnostic resolution was quantified by analyzing the grid in Fig. 4.3a. A simulated grid image was generated by convolving a 2D Guassian point spread function (PSF) with a 2D intensity array that represented the grid. Lineouts from the simulated image were fitted to the experimental lineouts by adjusting the standard deviation (σ) of the Gaussian PSF. A $\sigma = 6.5$ μm (FWHM = 15.3 μm) provided the best fit. In Fig. 4.7 the simulated and experimental grid images are shown, along with a plot that compares the averaged lineouts. As expected the vertical and horizontal experimental lineouts produced the same profile. The Gaussian PSF was convolved with the 2D intensity array that represented the simulated blast wave image with motion blurring included. The result was a further blurring of the image as shown in Fig. 4.6c. However, the model still did not capture the extent of the blurring observed in the experiment.

Finally, the shape and orientation of the leading edge of the blast wave was varied by shifting the values in the 3D mass array. The shape of the leading edge was modeled as a half wavelength of a sinusoid with $\lambda = 2$ mm and various amplitudes, and as a planar surface that was tilted at various angles. A combination of the half wavelength and the planar tilt was also tried. The combination model with a tilt angle $\theta = 7.8^\circ$ and amplitude equal to 15 μm provided the best fit to the experimental data. Figure 4.6f shows the shape of the leading edge in the combined model. This is a

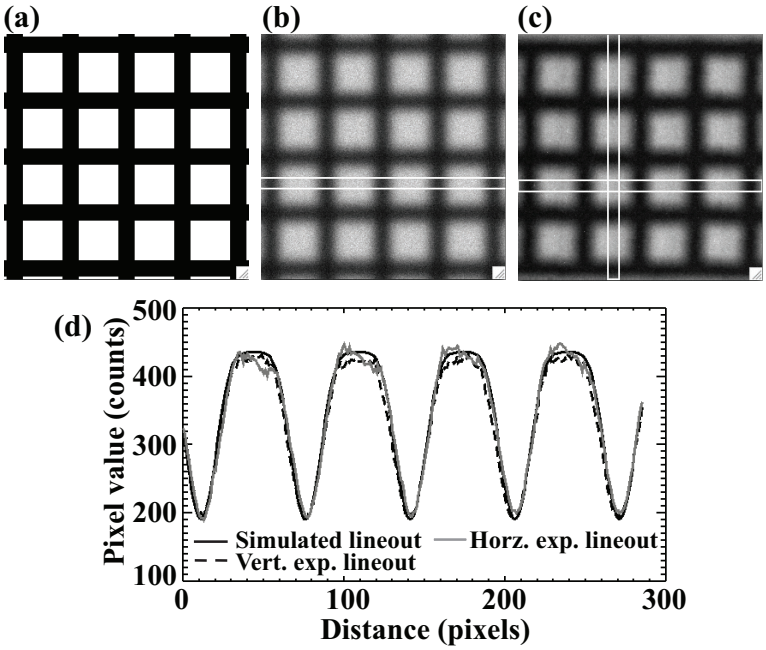

Figure 4.7: (a) Shown here is the 2D intensity array that represented the simulated Au grid in the object plane. (b) The simulated grid object was convolved with a Gaussian PSF ($\sigma = 6.5$ μm) in order to produce a loss of resolution that was similar to the experiment. Poisson noise was added to the simulated image. (c) A section of the experimental image from Fig. 4.3a. (d) Shown here is a comparison of the lineouts from the simulated grid image and the experiment. The white lines represent the sections over which the images were averaged in order to produce the lineouts. The simulated grid had a bar spacing of 63.5 μm (400 lpi) and a bar width of 19 μm. The manufacturer of the grid (Ted Pella) specifies the bar width at 28 μm. However, scanning electron micrographs of 4 randomly chosen grids revealed one with a bar width of 20 μm. Thus, it is reasonable to suspect that the grid seen in Fig. 4.3a had a bar width of 19 μm.

horizontal cross-section of the 3D mass array that shows a top-down perspective of the blast wave. The resulting simulated image is shown in Fig. 4.6d and the average profiles are shown in Fig. 4.8. In the initial modeling it appeared more attenuation, hence more foam compression, was required to achieve better agreement between the model and experiment. Unfortunately, density profiles for other γ values are not easily computed, so the analytic density profile for $\gamma = 1.4$ was modified by arbitrarily increasing the maximum density by increasing the value of the leading coefficient in Eq. 4.3. Of course the modified expression is no longer exact, but we expect only

small changes in the shape of the density profile for small variations in γ. All three of the simulated intensity profiles in Fig. 4.8 assumed a density profile with a maximum of 0.65 g/cm^3, which was introduced by increasing the leading coefficient in Eq. 4.3 from 6 to 6.5. This small increase in density improved the fit of the simulated profile by shifting the entire transmitted profile down to lower pixel values that matched the experimental values. Changing the density does not change the shape of the transmitted profile. It was the tilting of the blast wave was primarily responsible for the apparent broadening of the intensity distribution seen in the experimental radiograph.

Reasonable fits were also achieved by further increasing the compression and the tilt angle simultaneously. In addition, the uncertainty in μ_{CRF} allowed for a greater range in the acceptable values for the maximum density. For instance, a lower compression value could be compensated for with a slightly higher μ_{CRF} value that was within the limits of its uncertainty. Overall, the analysis indicated that the maximum density was 0.65 $\pm$ 0.05 g/cm^3. The uncertainty was set by the maximum and minimum density values that could be used to obtain acceptable fits to the experimental data. The uncertainty does not account for errors introduced by assuming a monochromatic x-ray spectrum. The compression would be overestimated if there was significant signal from continuum x-ray emission.

Interestingly the data suggests the density downstream from the leading edge does not rarify as quickly as in the model profile. In fact at x $\sim$ - 250 μm the data shows that the transmitted x-ray intensity begins to level off, which may mean the foam density became constant. How this comes to be is not clear. The additional reflected shock waves from the walls of the Be shock tube could be important. The shocks reflected from the top wall and the plastic ripple can increase the areal mass along the diagnostic line of sight. Spatial variations in the x-ray source intensity have been neglected here since they did not appear to be present in the t = 25 ns image. The

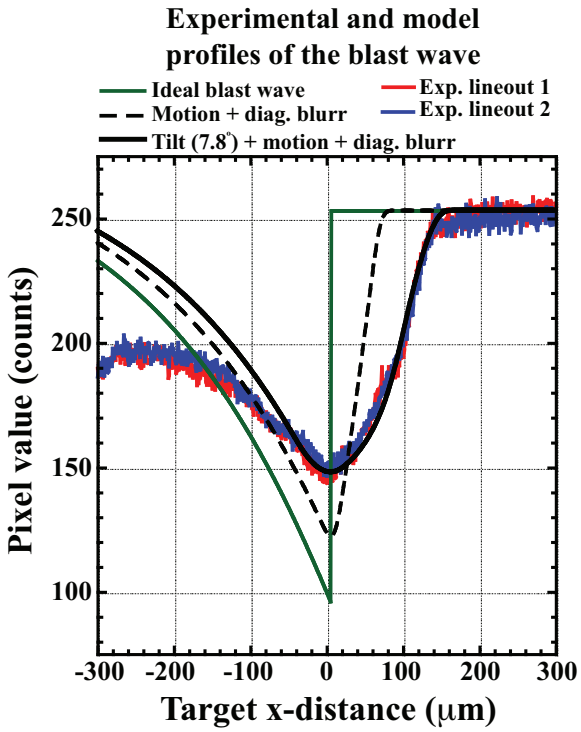

Figure 4.8: This plot shows two experimental lineouts of the blast wave seen in Fig. 4.3a, and three lineouts from the blast wave models shown in Fig. 4.6. The experimental lineouts were taken from two different locations just below the Au grid. The green curve is a lineout of Fig. 4.6a, which included no blurring effects. The dashed curve is a lineout of Fig. 4.6c, which includes motion blurring and finite diagnostic resolution. Finally, the black curve is a lineout of Fig. 4.6d, which included motion blurring, finite diagnostic resolution, and the variation of the shape and orientation of the blast wave.

spatial non-uniformity of the x-rays transmitted through the unshocked foam ahead of the blast wave was less than 10%. However, an erroneously high density would be inferred if the source intensity abruptly decreased in the region behind the blast wave. Future experiments should use a lower image magnification or a larger piece of film so that the unattenuated source can be observed around the perimeter of every target.

4.3.2 Transition to turbulence

For an experiment that maintains a steady flow, the transition to turbulence is expected to occur when the outer scale Reynolds number reaches $\sim$ 1-2 x 10^4 [84]. The transition is characterized by a fine (sometimes referred to as "molecular" or "atomic") mixing of fluids, and the development of a large range of spatial scales that have a characteristic spectrum. In planar shear layer experiments the large, outer spatial scales grow from the KH vortices. If the flow is maintained for a sufficient length of time, an intermediate range of spatial scales (known as the "inertial range") will develop. The inertial range is uncoupled from the energy carrying, outer scale and the much smaller Kolmogorov scale, which dissipates energy through the viscous heating of the fluid. If the existence of the inertial range is a necessary condition for turbulence, then simply having a large Reynolds number is not sufficient for a turbulent state to exist. Rather a large Reynolds number must be maintained long enough until the inertial range is established. The KH experiment presented here produced an unstable flow and hence a time varying Reynolds number. Thus, it is not immediately clear if the flow was turbulent. Looking at the cores of the vortices in Fig. 4.3c the fine structure appears to dissolve as the vortices evolve, so one might argue that a transition was beginning to take place. However, since turbulence requires large-scale 3D motions we would expect the break up of the entire vortex upon a turbulent transition. The energy cascade to smaller scales is driven by the vortex line stretching that can only occur in the presence of 3D motions. So if the vortices remain well-organized with no internal structure then a fully turbulent state will not be achieved. On the other hand, if an impulsive flow has enough time to briefly generate 3D motions then a decaying turbulent state will appear.

A detailed analysis of a similar experiment, which generated a Rayleigh-Taylor instability, concluded that the transition had not occurred and that more laser energy was necessary to maintain a larger Reynolds number [85]. Determining the temporal

history of the Reynolds number is challenging because it depends on the plasma viscosity, which is sensitive to the ionization state of the plasma. The temporal history of the ionization state must be determined from numerical simulations since it is difficult to extract from experimental measurements with the currently available diagnostics. In the future we plan to apply the same transition analysis that was presented in Ref. [85] to our KH experiment.

Nevertheless, we calculated a single Reynolds number using only the experimental data and published analytical expressions. The analysis in the previous section determined that the maximum density at the leading edge of the blast wave was 0.65 g/cm^3, but could be as low as 0.6 g/cm^3 and as high as 0.7 g/cm^3. Assuming strong shock conditions, the range of density measurements implies a range of γ values. For the following calculations the density is taken as 0.65 $\pm$ 0.5 g/cm^3, which corresponds to an approximate variation $\gamma = 1.36 \mp 0.04$. Using these values for ρ and γ the post-shock flow speed, pressure, foam temperature (T_s), average ionization state (Z), and kinematic viscosity (ν) were calculated. By requiring the conservation of mass flux through the blast wave we find that foam plasma immediately behind the blast wave had a speed of 51 $\pm$ 7 μm/ns. Then using Eq. 3.3 we find that foam plasma immediately behind the blast wave had a pressure of 3 $\pm$ 1 Mbar. Assuming electron-ion equilibrium, the post-shock foam temperature (T_s) is given by,

$$T_s = \frac{2(\gamma - 1)Am_p u_s^2}{(1 + Z)(\gamma + 1)^2} \tag{4.9}$$

where γ is again the adiabatic index of the shocked foam, A is the atomic mass of the foam, m_p is the proton mass, and u_s is the blast wave speed [78]. Analytical fits to the Thomas-Fermi ionization model [77] were used to iteratively solve for the average ionization state until it was consistent with the value given by the above equation for T_s. This process yields $T_s = 17 \pm 5$ eV and $Z = 2.4 \pm 0.3$. Inserting

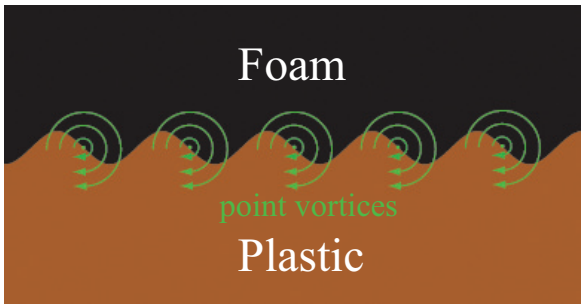

Figure 4.9: Shown here is the setup for the discrete vortex model that was used to calculate the growth of the interface. The point vortices were spaced one wavelength apart and positioned in the center of the perturbations.

these values into a known equation for kinematic viscosity [86] gives $\nu = 0.013 \pm 0.003$ cm^2/s, which leads to an initial Reynolds number of 10^6 using a post shock velocity of 50 μm/ns and a scale length equal to the initial peak-to-valley amplitude of the perturbation (60 μm). The Kolmogorov scale length (δ_K) can be determined by evaluating $\delta_{outer} Re^{-3/4}$, where δ_{outer} is the outer scale length of the flow, which we assumed equal to the peak-to-valley amplitude of the perturbation. This gives $\delta_K = 0.002$ μm for Re $= 10^6$ and $\delta_{outer} = 60$ μm. The resolution of the imaging diagnostic is on the order of 10 μm making it impossible to directly observe the Kolmogorov scale in this case. However, based on the observation that the vortices appeared to remain 2D in Fig. 4.3, the existence of a fully turbulent state does not seem likely.

4.3.3 Modeling the vortex growth

In Fig. 4.5 a discrete vortex model with a constant circulation $\Gamma = 4700$ μm^2/ns was used to calculate the time-dependent growth of the perturbations, starting from a compressed height of 44 μm [57, 64]. In this vortex model the potential flow generated by an infinite string of line vortices was calculated. The spacing between vortices was equal to the perturbation wavelength ($\lambda = 400$ μm) as shown in Fig. 4.9. The circulation per vortex was determined by evaluating Eq. 10 from Ref. [57]. In this equation the circulation was derived from the baroclinic vorticity that was generated

at the interface as a result of the strong density and pressure gradients that existed near the leading edge of the blast wave. The strength of the vorticity was determined by evaluating the baroclinic source term ($\nabla\rho \times \nabla p/\rho^2$) in the vorticity equation. Interestingly, this is the same term that is responsible for RM growth, yet in the KH scenario the vorticies have the same sign. In other words they are all rotating in the same direction, clockwise or counterclockwise. It is important to point out that the incompressible KH growth rate given by Eq. 2.1 is greatest when the fluid densities are equal (i.e., A = 0). This implies that $\nabla\rho = 0$ across the interface. So we might think that the plastic block should be replaced with a foam block that has the same density as the one above it. However, once the shock is launched it will cross the perturbed interface and continue to travel at the same velocity since it will not experience a change in material density. Because of this lack of shock refraction at the interface, the velocity of the shocked fluid will be the same on both sides of the interface. In this case there will be no shear flow to drive the KH instability. When an initial density difference does exist (i.e., $A \neq 0$) the shock is refracted as it crosses the interface, which leads to a velocity difference that generates vorticity. No further vorticity is generated after the shock crosses the interface. However, the vorticity strength can be maintained if the flow behind the shock remains constant. In the Omega experiment presented here the flow velocity was not constant, so the vorticity strength decayed over time.

From the calculated circulation, the components of the velocity field were determined. The position of the interface was tracked in time by numerically solving the differential equations for the velocity field (Eq. 12 and 13 in Ref. [57]) using points along the unperturbed interface as the initial conditions. At each time step the height of the interface was determined by finding the point on the interface that had the largest height (i.e., the largest y-coordinate). Early in time the points closest to the vortex center grew the fastest, while the points further from the vortex grew slower

but contributed later in time. As shown in Fig. 4.5 the vortex model predicts a saturation of the roll-up height. At saturation the roll-up peak-to-valley height is 0.56λ.

In the experiment the roll-ups are further stretched by the decompression of the shocked CHI, which is not now included in the model and perhaps why the model underestimates the height of the roll-up later in time. Figure 4.5 shows the incompressible, inviscid KH growth model that was derived from the linearized fluid equations [63]. Here constant shear velocities (ΔU) of 50 μm/ns and 12 μm/ns were used. The 12 μm/ns value is equal to the average velocity calculated from the self-similar velocity profile over the $\sim$ 30 ns time period it takes the velocity to decay to zero. These simple linear models predict exponential growth and do not include a velocity transition layer. Adding a transition layer would further slow the growth of the perturbations. In any case the linear models are only valid up to a perturbation amplitude that is 0.1λ, which is 40 μm or 80 μm peak-to-valley for present experiment.

Simulations of this experiment face their own challenges. These include the unknown equation of state of the foam, laser absorption treatments that are not fully three dimensional, and the problem of the resolution of small-scale structures. Figure 4.5 also shows results from preliminary 2D CALE simulations, discussed elsewhere in [57, 58], that overestimated the average blast wave velocity in the first 25 ns by $\sim$ 20%. The time used for the simulation data points in Fig. 4.5 was the time elapsed when the simulated blast wave reached a given crest. The simulated roll-up heights do not agree well with the experimental values. Further work must be done to refine the simulations. We expect that 3D simulations will be necessary to achieve good agreement with the experiments. The increased decompression of the flow due to the break out of the shock through the walls of the shock tube in the added dimension will cause the flow behind the blast wave to slow down more rapidly and earlier in time

relative to the 2D case. This effect has been observed in 2D simulations that used thinner shock tube walls. Also, the present simulations did not include a turbulence model, which may have an important effect on the vortex development. Preliminary 2D CALE simulations using a $k - \epsilon$ type model predicted that the vortices were completely dissolved by 75 ns. It is important to point out that the simulation data present in Fig. 4.5 was taken from simulations that were carried out before the experiments were performed. More recent simulations are in better agreement with the experimental data, but still overestimate the roll-up height.

4.3.4 Bubble structures in the flow

The source of bubble-like structures that appear to emanate from the downstream side of the left-most roll-up in Fig. 4.3b and the two-left most roll-ups in Fig. 4.3c is not known. Similar bubble structures have not been observed in any previous HED experiment. Based on the observed x-ray attenuation, the densities associated with these structures are as follows. The brighter regions within the largest bubble in Fig. 4.5c had densities of 0.03 (+ 0.06, - 0.03) g/cm^3 while those of the dark rim of the bubble were 0.21 $\pm$ 0.06 g/cm^3. Uniform regions outside the bubble had densities of 0.10 $\pm$ 0.06 g/cm^3. The measured average density difference between the exterior and interior of bubble ($\rho_{out} - \rho_{in}$) was 0.09 $\pm$ 0.03 g/cm^3. The bubbles appeared to be expanding at $\sim$ 10 μm/ns. Ref. [58] shows that the bubbles are not now reproduced by 2D simulations, and offers several hypotheses concerning their origins. The current uncertainty in the equation of state of the CRF foam is certainly a major limitation. We speculate that the formation of the bubbles may be associated with the velocity reversal of the CRF flow. The bubbles may also have some connection with the shocklets discussed as a theoretical possibility by Dimotakis [87].

4.4 Conclusion

In conclusion, this Omega KH experiment is significant because it demonstrates a novel method for creating a shear flow and is the first to create a diagnosable KH instability in a HED system. Understanding the KH instability is important because it plays a central role in the transition to turbulence in many HED, astrophysical, and other fluid systems. We observed unique bubble-like structures whose origins are still under investigation. Currently, simulations are unable to reproduce these bubbles, indicating that this shear flow experiment provides a rigorous test for benchmarking numerical simulations. Future laser-driven experiments using steady shocks rather than blast waves could create a more sustained flow with a higher Reynolds number in order to drive the system to a fully turbulent state.

CHAPTER V

Conclusions and Future Directions

5.1 Conclusions

The previous chapters showed the results from two new experimental targets that were designed to create the KH instability in a HED plasma. The development of these targets was motivated by the need to understand the detailed evolution of the KH instability in a fluid that was ionized and highly compressible. Until the development of these targets, there were no previous experiments in the HED regime that successfully observed the evolution of the KH instability. The KH instability is important because it initiates the entrainment and mixing of one or more fluid species, which ultimately leads to a transition to turbulence. Once this transition has occurred the properties of the flow change dramatically. Understanding the mixing and turbulent transition is critical to the success of the current ICF program. The degree of mixing that occurs between the DT ice and DT gas in an imploding fuel capsule affects the efficiency with which fusion products are generated. As the degree of mixing increases it becomes more difficult to produce high gain implosions. In addition, mixing in the HED regime is applicable to astrophysical systems such as supernovae, accretion disks, and jets. The mixing that occurs during a supernovae explosion determines how and when the heavy elements deep inside the star get transported to the surface and observed from Earth.

The goal of the experiments presented here was to develop experimental platforms that would generate an observable KH instability in the HED regime. These experiments were not aimed at imitating a specific astrophysical or ICF system. However, these platforms now enable future experiments to explore the astrophysical cases or other phenomena such as the transition to turbulence. Toward this end, two different platforms were developed. The first platform used the Nike laser to create and drive a supersonic flow ($M = 2.6 \pm 1.1$) of Al plasma that propagated over a low-density foam surface. The radiographic images of this target showed little perturbation growth, and further analysis revealed that the RM instability could contribute to some of the observed growth. This illustrated that the RM instability is quite ubiquitous in HED systems, and is present any time a shock wave encounters or is launched from a structured interface. Thus, future HED experiments must carefully tune the relative growth rates of the KH and RM instabilities so that only one instability governs the evolution of the flow. The combined KH and RM growth is a potential interesting area of research that should only be attempted after the pure KH system is well understood.

In addition, the research surrounding the analysis of the Nike experiment brought to light the significant role compressibility plays in decreasing the KH growth and the subsequent mixing. This fact has perhaps not been fully appreciated by the HED community. Simple calculations showed that the growth observed in the Nike experiment may have been reduced by compressible effects. As will be discussed later, future experiments should vary the Mach number from subsonic to supersonic and compare the KH growth for each case. Further analysis of the Nike radiographs revealed that the distinct dark bands surrounding each perturbation were due to an increase in density caused by the compression of the Al flow. Two-dimensional FLASH simulations suggested that the compression maybe be strong enough to create shock waves, in which case the shape of these shock waves was influenced by the supersonic

Mach number and the shape of the perturbation. As the Mach number is increased, the shock transitions from a detached bow shock to an attached shock.

The Omega experiment was more successful at generating the KH instability. The increase in the available laser energy allowed for a target design that was distinctly different from the Nike target. In the Omega target, a shock wave was confined inside a Be shock tube while it propagated along a rippled interface. Due to the relatively short duration of the laser pulse the shock quickly decayed into a self-similar blast wave that was responsible for depositing vorticity onto the perturbed interface. A refracted shock wave propagated down into the plastic perturbation which subsequently turned into plasma. Once in a plasma state the interface was free to roll-up into large vorticies that are characteristic of the KH instability. The evolution of the vorticies was captured with a series of images from three identical targets, each captured at different times. These were the first data collected in the HED regime that tracked the evolution of a well resolved KH instability.

The high quality of the data enabled a measurement of the Reynolds number of the immediate post-shock flow. The maximum density of the foam was inferred from a model that included the self-similar density profile, diagnostic blurring due to source broadening, and motion blurring. With all of these effects included, the inferred maximum density was 0.65 g/cm^3, which indicated that a $\gamma = 1.4$ was reasonable. Using these values the measured Reynolds number was $\sim 10^6$. As discussed in Sec. 4.3.2 a large Reynolds number does not guarantee a turbulent state. Due to the unsteadiness of the flow it is not clear how long this large Reynolds number is maintained. Finally, the Omega experiment produced low-density bubble structures that thus far have not been reproduced by numerical simulations. The physical process that created these bubbles remains unknown. These bubbles continue to motivate future experiments.

5.2 Future Directions

There are two future experimental endeavors that are natural extensions of the work presented here. First would be the development of an experiment that generated an observable transition to turbulence starting from a small perturbation ($\eta_0/\lambda < 0.1$). This experiment could be similar to the Omega experiment, but would need to establish a steady flow, such that a perturbation experiences a constant velocity flow. This might be achieved by using a laser pulse with a longer temporal duration, which could support a steady shock wave with uniform post-shock conditions. On the way to becoming turbulent the vortices are expected to coalesce and form larger vortices, which increases the amount of mixing. This process is known as vortex pairing or amalgamation. To encourage vortex pairing a multi-mode interface should be used. Vortex pairing should also be studied in both incompressible and compressible flows. Traditional splitter plate experiments have shown that the break-up of the vorticies is accompanied by the formation of small pairs of counter-rotating, streamwise vortices [88]. They are referrred to as "streamwise" because the axes of these vortices are aligned with the direction of the flow. They are believed to play an important role as a secondary instability that initiates the break-up of the main vortices during the transition to turbulence. In future HED experiments the streamwise vortices may be imaged by viewing the target from above or directly along (i.e., parallel to the perturbation wavevector) the perturbed surface. These viewing directions are both orthogonal to that of the current Omega target. In either of these new orthogonal lines of sight, the clever placement of a thin tracer layer will most likely be needed to localize the absorption of the x-rays that form the radiographic image.

Determining when and if the flow is turbulent will be challenging due to the limited resolution of the images produced by the current diagnostics. In the best case scenario, a series of images would show a vortex that appears coherent and organized early in time and then completely dissolved later in time. Also, a supporting argument would

be made that the Reynolds number was maintained sufficiently large for a duration of time such that the inertial range of spatial scales was established. The image sequence and the Reynolds number argument would be perhaps the most evidence that can be brought to bear to convince ourselves that the flow has reached a turbulent state. On the other hand, if the velocity fluctuations of the flow could be measured then this could be used to recreate the spectrum of length scales, which would provide direct insight into the conditions of the flow. However, with the current diagnostics it is not clear how a series of such time-resolved measurements could be carried out in these types of HED experiments. Future targets on the NIF and possibly the Z-machine [89] could be an order of magnitude larger than the current generation of targets. These targets could have centimeter scale dimensions with perturbation wavelengths around 1 mm and amplitudes of 0.1 mm. Increasing the target size would perhaps make a turbulent transition easier to observe.

The second interesting extension of this thesis work is the investigation of the KH instability in a compressible HED flow. As the flow becomes increasingly compressible (i.e., achieving higher Mach numbers) the KH growth is suppressed and the shape of the vortices is expected to change. The vortices may become stretched preferentially in the direction of the flow and thus become less effective at entraining unmixed fluid. We may have already observed such vortices in the Omega experiment. Some of the vortices in Fig. 4.3a and 4.3b appear to be folded over and stretched in the direction of the flow during the early phases of their evolution. This may be expected since the flow immediately behind that blast wave was supersonic in the laboratory frame of reference. Previous compressible experiments in cold fluids have not captured the linear KH growth or the developing roll-up. In such experiments the flow quickly becomes turbulent before the vortices are imaged. In a HED experiment a supersonic flow could be created by maintaining a steady shock or by the release of a shocked fluid into vacuum, which was the method used in the Nike experiment. Ideally, the

density, pressure, and flow velocity could be inferred from the radiograph and used to measure the Mach number, and determine if the Mach number has any spatial variations. The goal of such an experiment would be to measure the KH growth for flows with a variety of Mach numbers. Perhaps starting at $M \sim 1$ and beyond $M = 2.83$. A compressible vortex sheet with equal density fluids is predicted to be stable for $M \geq 2.83$. Here it was assumed that one of the two fluids is fixed in the laboratory frame of reference, so that the Mach number is defined as the flow velocity of the fluid in motion divided by its sound speed. Finally, imaging x-ray Thomson scattering could be used to measure the spatial variation of the temperature and ionization state. Once these quantities are known then the viscosity, and hence the Reynolds number, can be easily determined.

APPENDICES

APPENDIX A

Microchannel Plate Operation and Modeling

A.1 Introduction

To capture the fast hydrodynamics taking place in many ICF and high-energy density experiments requires an imaging system with an extremely short exposure time. Material and shock velocities in these experiments frequently reach 100 μm/ns (100 km/s), while the associated imaging diagnostics have resolutions on the order of 10 μm. This means that exposure times must be around 100 ps in order to confine the motion blurring to a few resolution elements of the detector. Unfortunately, this exposure time is not obtainable with traditional mechanical shutters or conventional solid state detectors such as charged coupled devices (CCD) or complementary metal oxide semiconductor (CMOS) devices that can operate in direct detection mode or with a phosphor converter. Furthermore, the signal in some experiments requires amplification. The solution often involves making an intense burst of x-rays that has a temporal duration short enough to reduce motion blurring. With the recent development of ultra-fast lasers, it is now possible to create short duration K-α x-ray sources using laser pulse lengths of 1-10 ps and spot sizes < 10 μm FWHM [90]. In

other cases, a device known as a gated x-ray framing camera (XRFC) is employed. This diagnostic uses a microchannel plate (MCP) to detect and amplify the incident x-ray signal. The MCP is essentially a thin, semi-conducting glass wafer with millions of small cylindrical channels (diameters typically around 10 μm) that operate much like tiny photomultiplier tubes by converting incident x-rays to into bursts of electrons. As these electrons exit the rear of the MCP they are then accelerated onto a phosphor coated fiber optic screen, which produces visible light that is then detected by a CCD or film. The MCP can serve as fast shutter if a short voltage pulse is applied to Au conducting strip lines that have been previously deposited onto the MCP surface by thermal evaporation or sputtering. The applied voltage controls the channels ability to multiply electrons. When no voltage is applied, the MCP is effectively turned off and remains mostly opaque to x-rays below 10 keV for the typical MCP thickness and channel spacings used in most HED experiments. At higher energies the probability that x-rays will pass through the entire thickness of the MCP without being detected increases. Microchannel plate gain, defined as the number of electrons produced by a single detected x-ray, and the MCP detection efficiency, defined as the probability an x-ray incident inside a channel will produce an output event, are two important metrics for MCP performance. Modeling these has proven difficult under the various conditions relevant for ICF and HED experiments.

Due to its ability to gate and amplify x-rays, the XRFC has been a work horse diagnostic for ICF and HED experiments for the past 25 years and will continue to be an essential diagnostic for the first ignition experiments on the National Ignition Facility in Livermore, CA. The XRFC will be needed to look for possible implosion asymmetries as well as to capture radiation spectra from the first fusion experiments that hope to achieve unity gain. Improvements to the imaging performance of the XRFC would undoubtedly allow us to more accurately diagnose any given experiment. The MCP primarily controls the XRFC performance, and so it has been the target of

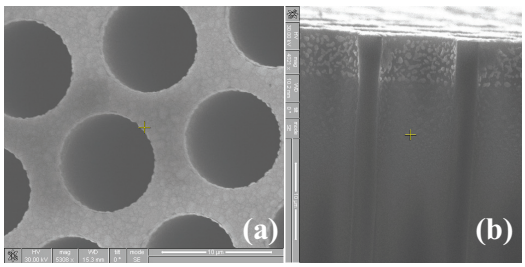

Figure A.1: Scanning electron micrographs of a microchannel plate with 10 μm diameter pores. This plate has been coated with solid CsI by the manufacturer Burle, Inc. (a) This is the input side of the MCP. (b) The MCP was broken in order to capture this image of the pore interior. Notice the CsI has become bunched into islands, probably due this particular plates exposure to humid air. This effect has been previously observed by [91].

much previous research. Many studies have attempted not only to improve the MCP performance, but also to characterize its performance in order to attain absolutely calibrated data. Here we attempt to model the absolute electron output of a single MCP to study the detection efficiency and noise generation. The model output is compared with experimental data.

A.2 3D Microchannel plate modeling

In order to improve the XRFC imaging capabilities the physical processes that govern the operation of a MCP must first be understood. It is perhaps most insightful to decompose the operation of the MCP into two fundamental processes. The first is the absorption of x-rays, which generates electrons with some initial energy spectrum and spatial distribution. Depending on their energy these electrons undergo a few to many collisions inside the MCP wall, and some may reach the channel surface and proceed into vacuum. Electrons emitted into vacuum with energies less than 50 eV are typically referred to as secondary electrons, while electrons with higher energies are known as photoelectrons or Auger electrons, both of which are contained in relatively narrow energy bands. The second process is the multiplication of these

electrons as they begin to propagate down a channel. The electric field inside the pore accelerates the electrons back into the wall, where they may produce more electrons that are again accelerated further down the channel. After the first electron emission from the x-ray absorption, it is thought that only secondary electrons are involved in the multiplication process. In most cases, absorption of the x-rays and the subsequent secondary electron multiplication process occur inside a single MCP channel. However, at x-ray energies above 3 keV (or perhaps as high as 5 keV), x-rays that cross multiple pores may begin to produce a non-negligible signal. Furthermore, the x-ray detection can take place in a separate medium such as a suspended transmission photocathode, which supplies the MCP with electrons. This is discussed in Ref. [92]. Here we will investigate the details of x-ray absorption and electron emission and a simple approach to modeling each of these processes.

An ideal MCP would detect all incident x-rays and then produce the same number of electrons for every incident x-ray. Yet, real MCPs are far from ideal. For instance, two x-rays with identical energies may strike the same location in a MCP channel and produce electron events with different sizes. This is the origin of MCP noise that subsequently becomes imprinted on the final image. A perfectly uniform signal is essentially transformed into a speckled image with some distribution of intensities due primarily to the gain variation in the MCP. It is important to note that the phosphor screen is also a source of noise due to the variation in phosphor coating thickness, phosphor sensitivity, and the variation of absorption in the fiber optic that guides the visible light produced by the phosphor to the CCD or film. In addition, a CCD may also introduce output variations due to defective pixels and non-uniform quantum efficiencies. The noise or perhaps more accurately, the variation in the detected signal, produced from these effects is essentially constant and hence known as "fixed-pattern noise." Unlike the noise introduced by the MCP, this type of noise can be easily subtracted using flat fielding techniques [93].

A.2.1 X-ray absorption in the MCP

A description of the x-ray absorption and the associated electron emission depend on the x-ray incident angle (α), the x-ray energy (E_x), and the chemical composition and thickness of the receiving material. A general x-ray and material geometry is defined in Fig. A.2. The chemical composition of the MCP glass is not well known, which makes the x-ray absorption and the secondary electron emission modeling notoriously difficult. Not only does the composition vary with depth into the MCP wall, but also down a single channel [94]. For the common x-ray energies used in HED experiments (1-10 keV) the primary interaction with the MCP and its various coatings occurs through photoabsorption, which is characterized by the mass photoionization cross-section (μ_a) given in units of [cm^2/g]. Assuming each atom scatters independently (true for x-ray energies above 50 eV) and dipole scattering is the primary scattering mechanism (true for small scattering angle and/or wavelengths that are large compared with the atomic dimensions) the x-ray interaction is completely characterized by the angle independent atomic scattering factors $f_1(0)$ and $f_2(0)$ [95]. The form factors determine the complex index of refraction $(1-\delta+i\beta)$ and μ_a. These two quantities are the essential parameters for determining the absorption depth z of the x-rays (see Fig. A.2) as well as the reflection coefficient $R(\alpha)$. Assuming no multilayer effects, external reflection occurs for angles less then or equal to the critical angle α_c, given by $\sqrt{2\delta}$. In other words, $R(\alpha \leq \alpha_c) = 1$.

X-rays transmitted through the surface are refracted across the boundary and proceed to travel into the bulk of the material. The attenuation inside the material is given by $e^{-x\mu_a\rho}$, where ρ is the mass density and x is the path length traveled by the x-rays in the material. A path length equal to $(\mu_a\rho)^{-1}$ is defined as one attenuation length, the distance over which 63% of the incident x-rays have been absorbed. The absorption of an x-ray results in the emission of photoelectrons and Auger electrons into characteristic energies, which are determined by the electron binding energies

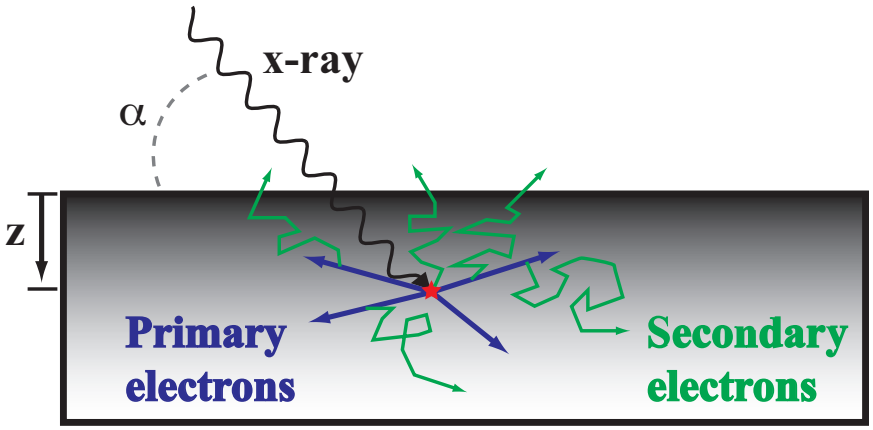

Figure A.2: An x-ray incident at an angle α is absorbed at a depth z. At the absorption site primary electrons are generated by the photoelectric and Auger processes. Through collisions with the material's valence electrons, the primaries produce secondary electrons that may eventually reach the surface and travel into vacuum.

of a particular atom. These electrons are referred to as primary or fast electrons and their spatial distribution inside the material is approximately isotropic [96]. As the primary electrons propagate away from the absorption site they undergo inelastic collisions with valance electrons, which are promoted to the conduction band where some may be energetic enough to leave the surface of the material. Those electrons that manage to propagate into the vacuum are the secondary electrons. They typically have an energy spectrum that is narrowly peaked around a few eV and a high energy tail that extends to a few tens of eV. The average number of secondary electrons emitted into vacuum per incident x-ray is known as the secondary electron yield (SEY). For a fixed energy and geometry the SEY can vary by an order of magnitude depending on the material. It is important to note that the primary electrons may leave the material after a few elastic collisions and contribute to the total electron yield. However, for the x-ray energies and materials of interest here, the number of primary electrons leaving the material has been shown to be negligible relative to the SEY. The number of primaries remains below $\sim 20\%$ of the total yield for x-ray energies of 1 keV [97]. Furthermore, the high-energy, elastically-scattered primaries

do not interact strongly with valence electrons and hence are typically not responsible for the generation of many secondaries. Rather, it is the primary electrons that are slowed by many inelastic collisions that ultimately generate most of the secondary electrons.

In order to model the absolute electron output of a MCP, the SEY from an incident x-ray must be accurately calculated. A semi-empirical equation for the SEY has been previously developed by Fraser *et. al.* [98]. The SEY is given by

$$SEY = [1 - R(\alpha)](1 - f)P_s(0)E_x\epsilon^{-1}(1 - \beta)^{-1}Y(T), \tag{A.1}$$

where $\beta = [\mu L_s \csc(\alpha')]^{-1}$ and $Y(T)$ is the relative yield versus thickness function given by

$$Y(T) = 1 - e^{-T(\mu \csc(\alpha') + L_s^{-1})}. \tag{A.2}$$

$R(\alpha)$ is the grazing incident dependent Fresnel reflection coefficient, f is the fraction of x-ray energy lost to primary electrons and material fluorescence, $P_s(0)$ is the average probability that a secondary electron will escape into vacuum once it has reached the surface of the material, E_x is the x-ray photon energy, ϵ is the average energy required to create a single secondary electron in the bulk of the material, μ is the x-ray linear absorption coefficient equal to $\rho\mu_a$, L_s is the average secondary electron escape length, α' is the angle of refraction of the incident x-ray, and T is the thickness of the material struck by the x-ray. The parameters $P_s(0)$, L_s, and ϵ are taken as semi-empirical constants that are material specific. See Table A.1 for a list these constants for the common materials used in MCPs. The values $R(\alpha)$, α', and μ are calculated from the atomic scattering factors, which have been experimentally determined and tabulated [95]. We assume that the primary electrons are not important contributors to the activation of the MCP channel. Here we assume that $f = 0$. In other words, all of the x-ray's energy is converted into secondary electrons. The parameters $P_s(0)$,

	$P_s(0)$	L_s (nm)	ϵ (eV)
MCP glass	0.15	3.3	10.0
Nichrome	0.024	2.0	6.65
Au	0.03	2.0	8.0
CsI (solid)	0.20	21.5	7.0

Table A.1: These parameter values were used to calculate the SEY given by Eq. A.1 and Eq. A.2. The values for MCP glass and Nichrome were taken from Ref. [98] and the values for Au were taken from Ref. [99]. The values for CsI were taken from Ref. [100].

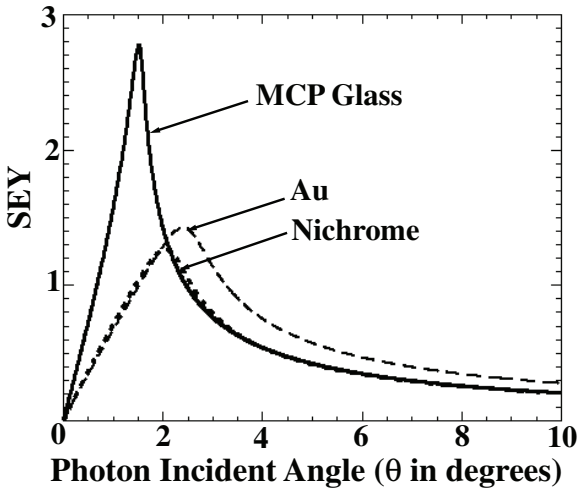

Figure A.3: Plotted here is the grazing incident angle dependence of the SEY for planar samples of MCP glass, nichrome, and Au using $E_x = 1.49$ keV (Al-Kα). The calculations were carried out using Eq. A.1, Eq. A.2, and the values from Table A.1. The MCP glass composition used for the SEY calculation was the type produced by Galileo given in Ref. [101].

L_s, and ϵ are given for four types of materials in Table A.1. Shown in Fig. A.3 is the angle dependent SEY that was calculated using Eq. A.1, Eq. A.2, and the values in Table A.1.

The channels of a MCP are usually tilted at some angle (referred to as the bias angle) with respect to the normal of the MCP surface to ensure that x-rays cannot travel directly through the MCP. In addition, the angled channel is thought to limit ion-feedback, a process in which ions created from residual gases at the output of a pore are accelerated back up the channel and initiate another cascade of electrons.

A non-zero bias angle establishes a MCP/x-ray interaction geometry for which α depends on the x-ray strike location inside the pore. For the three-dimensional MCP model developed here, we assumed the x-rays are normally incident on the MCP, which has a bias angle θ_B. In this case, α is given by Eq. A.3, where Ψ is the channel polar angle as defined in Fig. A.4b [102]. From this equation, we can see that $0 \leq \alpha \leq \theta_B$. It is important to note that the variation of α is purely a three-dimensional effect and is therefore not contained in two-dimensional models.

$$sin(\alpha) = cos(\Psi)sin(\theta_B) \tag{A.3}$$

A.2.2 Microchannel plate gain

The secondary electrons that are generated from the incident x-ray go on to be multiplied by the remaining length of the channel. The discrete dynode model can be used to estimate the total amplification of the secondaries [103]. The depth dependent gain $G(h)$ is given in Eq. A.4.

$$G(h) = \left(\frac{V}{V_0}\right)^{\frac{L}{4D}[1-(h/L)]} \tag{A.4}$$

Here V is the voltage difference between the input and output ends of the MCP, V_0 is the voltage difference required for unity gain, L is the total channel length, D is the channel diameter, and h is the distance from the rim of the pore to the location of the x-ray strike. Although, this model has been proven to give correct estimates, it relies on incorrect assumptions concerning the relationship between incident and emitted secondary electrons [104]. Equation A.4 does not account for saturation effects that will occur as the internal surface of the pore becomes depleted of electrons.

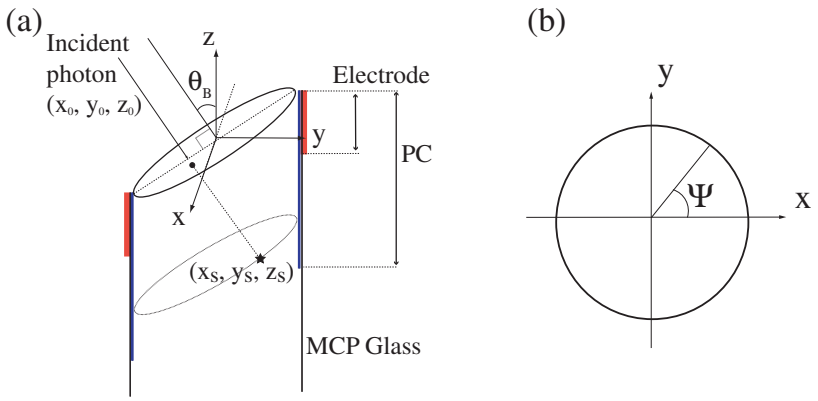

Figure A.4: (a) Shown here is the geometry of the microchannel plate model. (b) Definition of the channel polar angle Ψ.

A.2.3 3D MCP model

Our model assumes every channel on a single MCP has identical material composition, and electrode and photocathode coating specifications (e.g., coating thickness and coating depth down a channel). Therefore, the activation of many channels, spatially distributed across the input surface of the MCP, can be modeled as a single channel struck by many photons. Our present model does not yet account for multiple channel crossings of a single x-ray. This effect may become important for x-ray energies around 5 keV and above for a 10 μm channel diameter with a 12 μm channel-to-channel spacing. Figure A.4a shows the geometry of the single channel used in our working model. Notice the opening of the channel, at the input surface plane, is slightly elliptical due to the manufacturing process during which the MCP is cut at an angle from a cylindrical boule of MCP material in order to form channels with the specified bias angle (θ_B). The x-ray flux used in the model is assumed to be non-divergent and normally incident to the MCP surface, as seen in Fig. A.4a. Typically the x-rays used high-energy-density experiments are generated by line emission from a hot plasma, so the model x-ray flux is assumed to be monochromatic. With more effort a broad spectrum of x-rays could be incorporated.

The model begins by randomly placing a specified number of incident x-ray pho-

tons on the input surface plane of the channel. The position of the photons on the channel wall, given by coordinates (x_s, y_s, z_s) in Fig. A.4a, and the corresponding grazing incident angles (α) are then determined. α is calculated from Eq. A.3. Once the position of an x-ray strike is calculated, the model then determines what type and combination of materials the x-ray has struck. There are four possibilities: (1) MCP glass, (2) conducting electrode, which is typically nichrome, or if the electrode is also serving as the photocathode a popular choice is gold, (3) insulating photocathode material, such as CsI or KBr, with no electrode undercoat and (4) insulating photocathode with an electrode undercoat. Due to the end-spoiling effect, in which secondary electrons born into the region of the MCP coated with a conducting electrode may experience gain suppression, it is important to distinguish between cases (3) and (4). In the current model the secondary electron contribution from the interface of two materials, such as MCP glass and an insulating photocathode coating, was assumed to be negligible due to the relatively short escape lengths of secondary electrons compared to the coating thickness.

The SEY for each x-ray was calculated using Eq. A.1. The actual SEY value (δ_{SE}) that was then used in the MCP model was found by randomly sampling a Poisson distribution with a mean equal to the calculated SEY value. The reduced electric-field strength caused by the end-spoiling effect was expected to decrease the collision energies of the secondary electrons born in the end-spoiled region. As a rule of thumb, a secondary electron must be accelerated up to 30 eV before it strikes the MCP wall in order produce more secondaries. This energy threshold of 30 eV is sometimes referred to as the "first cross-over potential." To better quantify the end-spoiling effect we performed Monte Carlo simulations with a commercial electro-optics software package known as LORENTZ 2D that was purchased from Integrated Engineering Software. The software solved Poisson's equation in two-dimensions for a repeating array of channels that were each 10 μm across with 2 μm thick walls.

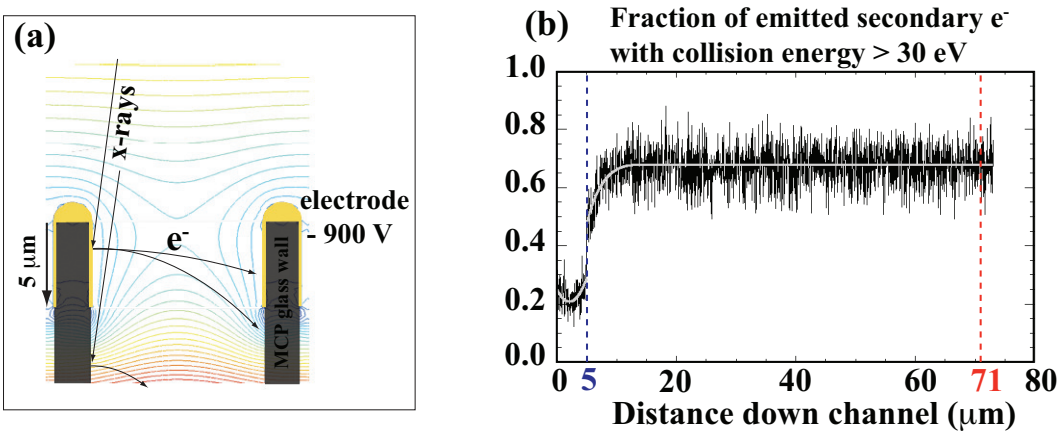

Figure A.5: (a) Shown here are the voltage contours for a MCP with - 900 V applied to the input electrode while the output electrode was held at ground (0 V). The channel diameter was 10 μm, and the channel wall was 2 μm thick and assigned a relative permittivity $\epsilon_r = 8.3$. The electrode coating was nichrome. It penetrated 5 μm into the channel. The LORENTZ simulations were carried out by G.K. Rathore. (b) Plotted here is f_s, which is the fraction of electrons that exceeded the first cross-over potential (30 eV) as function channel depth. The incident x-rays can only reach a maximum depth of 71 μm due to their 8° incident angle.

The total channel length was 430 μm. The resulting voltage contours are shown in Fig. A.5a. X-rays with energies of 1.49 keV were incident at 8° from the surface normal of the input face of the MCP in order to simulate a channel with $\theta_B = 8°$. LORENTZ then calculated the number of emitted secondaries and assigned each one a unique energy by sampling values from the energy distribution functions derived in Ref. [105]. Similarly, the emission angle of each secondary was found by sampling a standard Lambertian distribution function [105]. LORENTZ then tracked the secondaries as they were accelerated by the electric field inside the channel. Upon striking the wall their collision energy was recorded. The channel wall was discretized into 1 μm sized regions that were illuminated with x-rays until each region produced at least 100 secondary electrons. The exact number of secondaries from each region was assigned to the variable N_e. The number of secondaries that achieved a collision energy greater than 30 eV was assigned to the variable N_{30}. Then the regional fraction of secondaries

that exceeded 30 eV (f_s) is the ratio N_{30}/N_e. This fraction is plotted in Fig. A.5b as a function of the birth depth of the secondaries. Around 20 to 30% of the secondaries born in the first 5 μm of the channel will have collision energies larger than 30 eV. Around 68% of the electrons born deeper the channel will have collision energies larger than 30 eV. The percentage increases deeper into the channel due to the increased strength of the electric field that the electrons experience once they leave the end-spoiled region.

Using the plot in Fig. A.5 the end spoiling effect was included in our MCP model. In the model the sampled SEY value δ_{SE} was multiplied by f_s in order to determine the number of secondaries that will contribute to the final MCP output. The gain was then calculated using Eq. A.4. The final MCP output (MCP_{out}) is then given by Eq. A.5.

$$MCP_{out} = \delta_{SE} f_s G(h) \tag{A.5}$$

A.2.4 MCP Experiments

We used a DC x-ray source (Manson type) to illuminate an x-ray framing camera operated with static voltages applied to both the MCP and the phosphor screen. The x-ray source creates two identical x-ray beams with one directed at the framing camera and the other at a calibrated x-ray photodiode (IRD AXUV-100). When the framing camera and x-ray source are operated in a regime where the photon fluence per channel is $<< 1$ and the MCP gain is high (V $\sim$ 1 kV for $L/D = 40$), the phosphor screen becomes spotted with single MCP output events as seen in Fig. A.6. A pulse height distribution (PHD) can be constructed from Fig. A.6 and compared with the modeled PHD by striking our model channel with the same number of photons that are incident on the open area fraction of the MCP in the field of view of the CCD. We assumed the photons that struck the inter-channel space go undetected. Figure A.7 shows the resulting comparison of the simulated and experimental PHD.

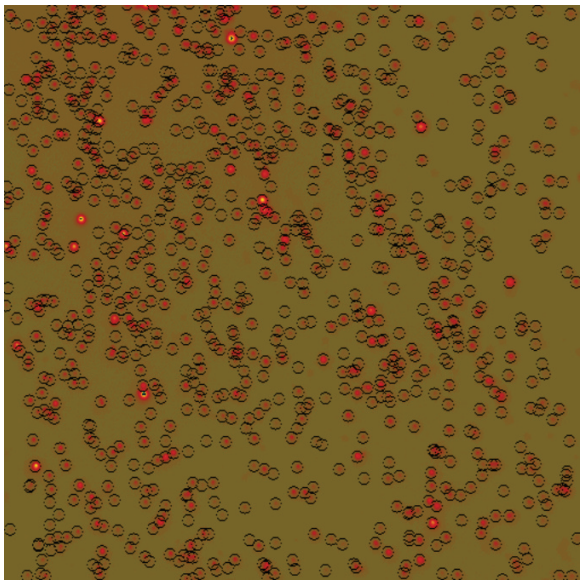

Figure A.6: A false color image of single MCP output events due to the detection of individual x-ray photons. For this image: the applied MCP voltage was 1100 V, the applied phosphor voltage was 4 kV, CCD exposure time was 10 milli-seconds, and x-ray flux was 2.4 $\pm$ 0.1 photons/s/channel, presumably from the Al K-α line (1.49 keV). A star finding routine called FIND, taken from the Online IDL Astronomy Users Library, was used to find and record the brightness of each event. Circles indicate a found event. The MCP used here was a Burle Long-Life^{TM} MCP with L/D = 43, D = 10 μm, $\theta_B = 8°$, and a nichrome(80/20) electrode coating that penetrates $\sim$ 5 μm on the input side and $\sim$ 20 μm on the output side. There was no insulating photocathode coating.

The model in its present, preliminary form appears to capture the range of intensity of the output events, but overestimates the quantum efficiency of the MCP glass. The overall MCP quantum efficiency (MCP QE) is defined as the probability that an incident x-ray will produce an output burst of electrons that can be detected by the CCD. If the x-rays that strike the inter-channel space are not detectable, then the maximum possible MCP QE value is equal to the open-area fraction of the MCP. The MCP used here had an open-area fraction equal to 64 %. For the data presented in Fig. A.7, the MCP QE was 3-5% for the experiment, 27% for the model with f_s = 1, and 20% for the model with the depth dependent f_s values from LORENTZ. We are now proceeding to improve the measurements by checking the source spectrum,

confirming the diode calibration, obtaining new MCPs (the one used for Fig. A.7 was old), and increasing the sensitivity of the system. We also need to assess the actual composition of the MCP glass. Future improvements include an accurate treatment of end spoiling based on electron optics simulations in actual fields and random sampling of the gain distribution, reflecting the statistical nature of the gain process [106].

A.2.5 Conclusions

Microchannel plates are important imaging devices used in many HED experiments to gate and amplify an incident x-ray signal. We have reported on the initial development of a 3D model used to produce the pulse height distribution of a single MCP. The model accounts for the actual variation in angle of incidence and the fact that incident x-rays can strike different materials. It also treats the statistical variation in secondary electron yield with angle of incidence and for the variation of average channel gain with electron birth depth. End-spoiling effects from the channel input electrodes were quantified and included in the model. In comparison with preliminary experiments, the model accurately captures the range of pulse heights but appears to significantly over predict the number of pulses produced by the MCP glass. The end-spoiling effect appeared to be significant, but not large enough to reduce the MCP QE to a value similar to the experiment. The measured experimental MCP QE was 3 - 5 %, while the model yielded 20%. Future experiments should perhaps track the secondary electrons for the first several collisions to determine if a sizable electron bunch will develop or if the bunch dies out before exiting the MCP.

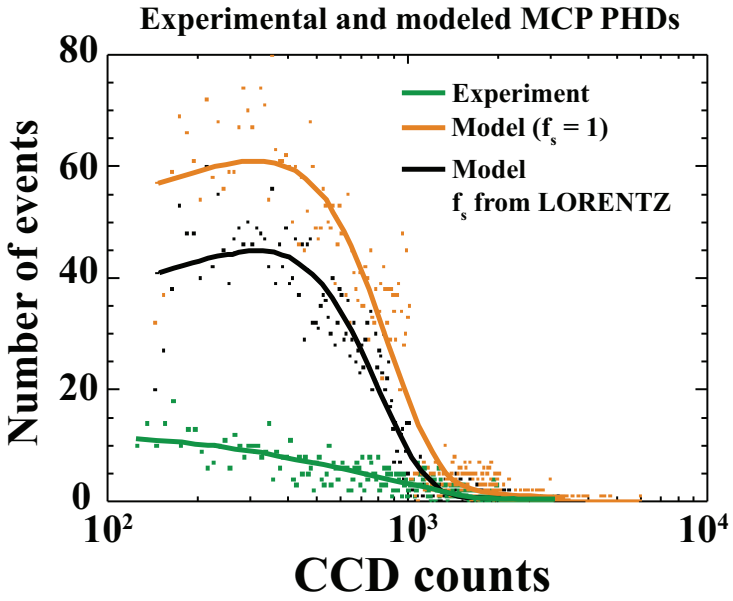

Figure A.7: A comparison of the PHD from our MCP channel model and experiment. The dots are the exact data from the experiment and model. The curves are analytical fits that are shown to help interrupt the results and compare different cases. From the photodiode measurement we estimated 8610 ± 400 photons strike the MCP open area in the CCD field of view. Thus the model simulates 8610 incident photons each with 1.49 keV. The experimental PHD was taken from the data in Fig. A.6. The gray curve shown in Fig. A.5b was used to determine f_s in one model while the other model used $f_s = 1$. The model output was scaled by a factor of 0.01 to account for the conversion of electrons to visible light at the phosphor screen, scattering losses in the fiber optic and CCD coupling lens, and CCD digitization. Model SEY values are taken from Fig. A.3 and $V_0 =$ 500 V for the gain calculations.

APPENDIX B

Additional Nike Data Images

Presented here in this appendix are all of the remaining radiographic images that were not shown in the chapters of this thesis. The data displayed here was collected over the course of three experimental campaigns. The campaigns took place in June 2007, September 2007, and September 2008. Each figure is labeled with one of these dates. For the duration of each campaign, the magnification of the spherical imager remained constant. So even though some images do not have grids, the distance scale can be inferred from other images in the same campaign. All of the grids have a bar-to-bar spacing equal to 63.5 μm.

In June 2007 all of the targets used the 300 x 300 μm W aperture, along with the semi-circular foam grooves that are shown in Fig. 2.4. These targets also used 10 μm Al foils coated with 20 μm Parylene-C. The Al foils were cold rolled and thus had large surface perturbations. In September 2007, the slotted Au knife-edges were introduced. Much larger vacuum gaps were also tried. The same Al foils used in June 2007 were tried again, but this time they were coated with 10 μm Parylene-N. The semi-circular grooves were again used for these targets. In September 2008, we began using smooth Al foils and sinusoidal foam patterns. For these targets the Al foil was 10 μm thick and coated with 20 μm of Parylene-N.

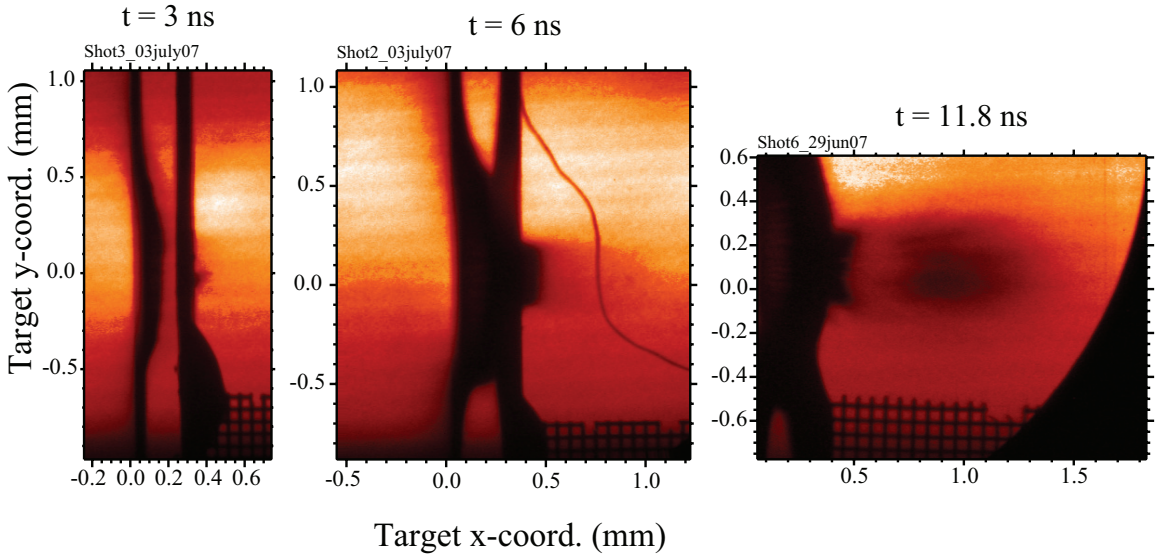

Figure B.1: Nike June 2007. These targets were used to characterize the Al flow when no foam was present. The vacuum gap for each target was 200 μm.

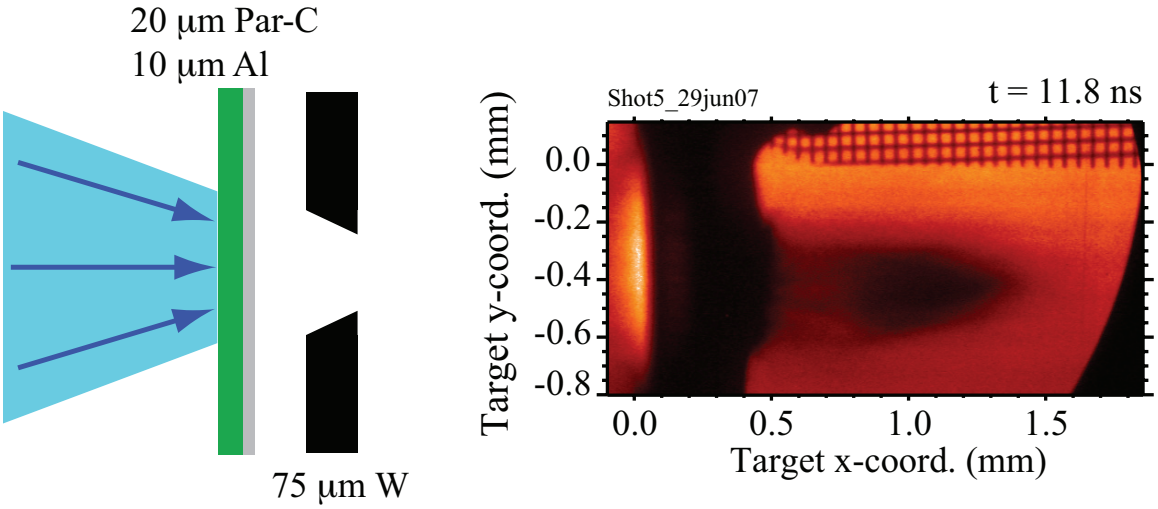

Figure B.2: Nike June 2007. This target used a W foil that was orientated such that the tapered aperture was opened toward the laser as shown in the diagram above. This was the only target that used this orientation. All other targets orientated the foil so that the tapered aperture opened away from the laser. This image shows that the orientation of the taper affected the shape of the Al plasma. Here the Al plasma appears bullet shaped, while the reverse direction (shown in Fig. B.1) produced a flow that appears less collimated.

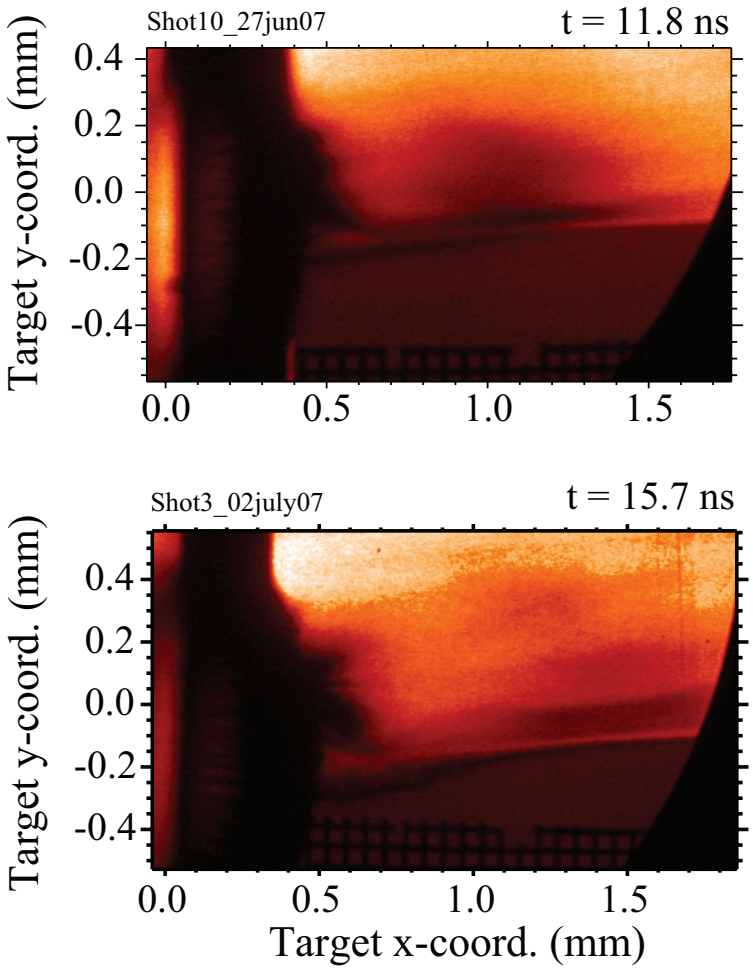

Figure B.3: Nike June 2007. These foams were machined flat. The vacuum gap was 200 μm for each target.

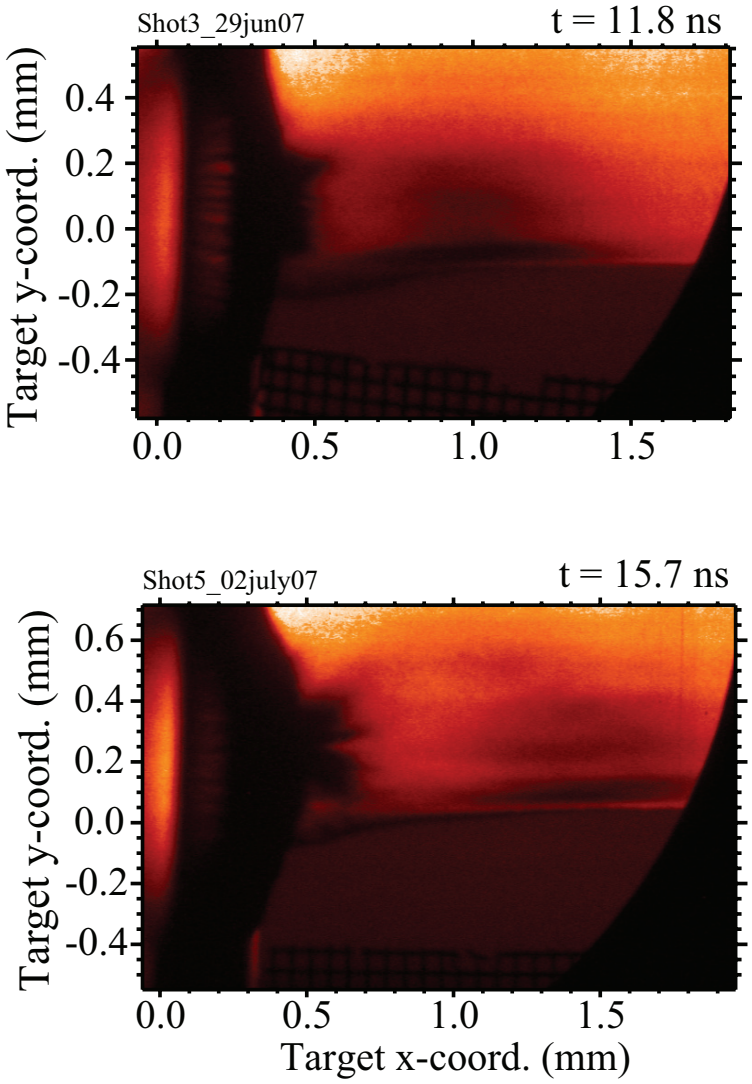

Figure B.4: Nike June 2007. These foams were machined with perturbations that had $\lambda = 100$ μm and peak-to-valley amplitudes equal to 5 μm. The vacuum gap was 200 μm for each target.

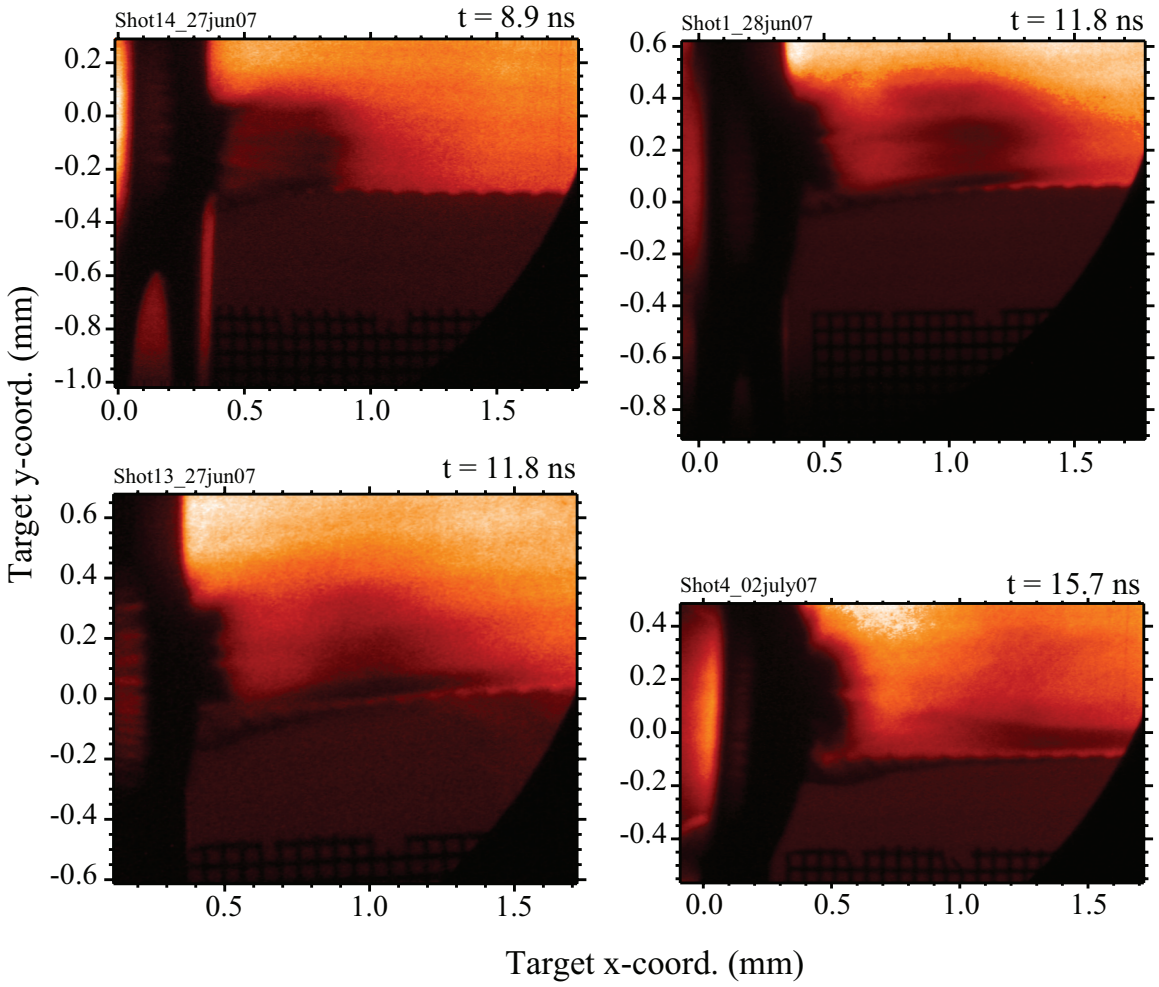

Figure B.5: Nike June 2007. These foams were machined with perturbations that had $\lambda = 100$ μm and peak-to-valley amplitudes equal to 13 μm. The vacuum gap was 200 μm for each target.

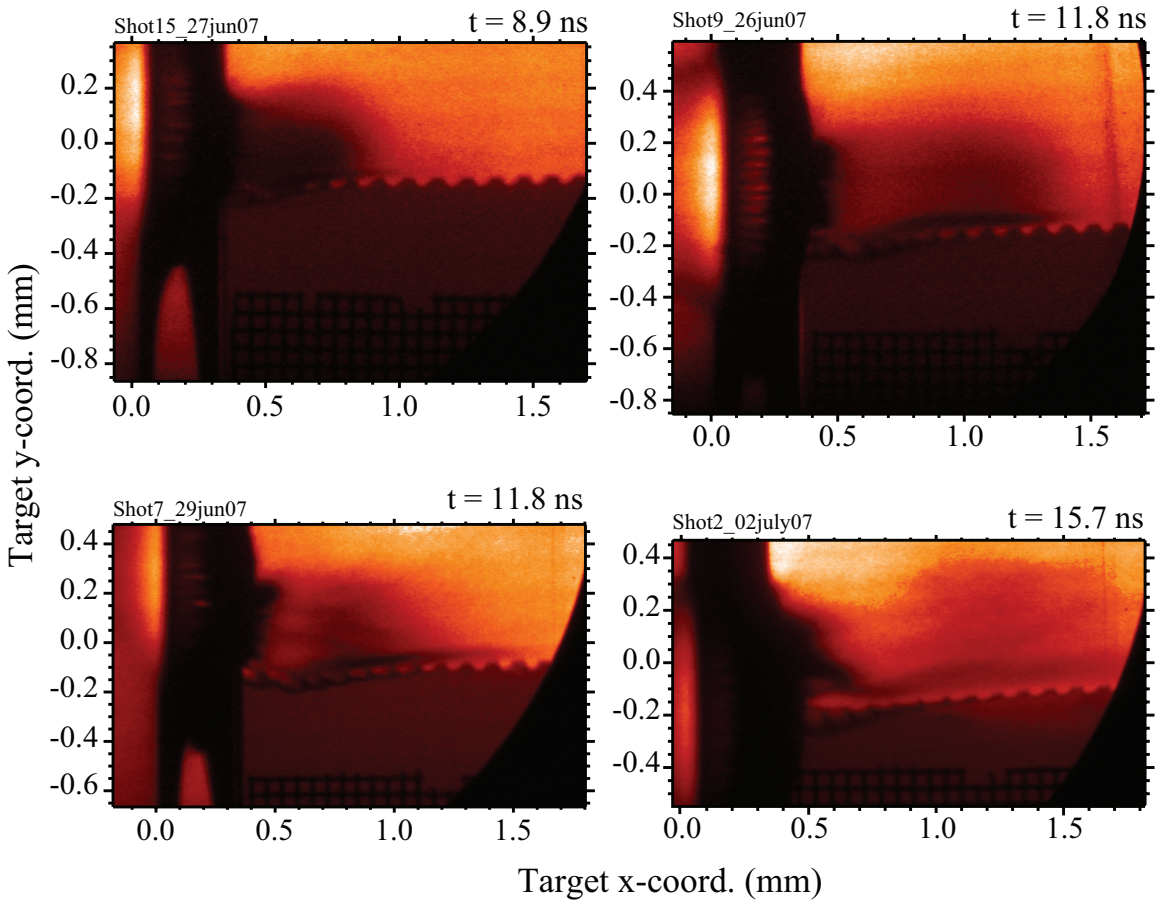

Figure B.6: Nike June 2007. These foams were machined with perturbations that had $\lambda = 100$ μm and peak-to-valley amplitudes equal to 30 μm. The vacuum gap was 200 μm for each target.

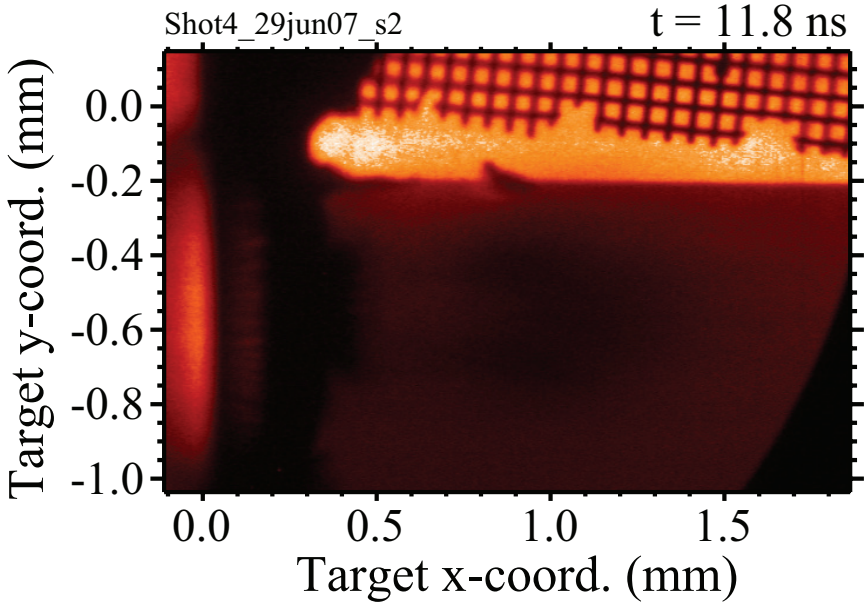

Figure B.7: Nike June 2007. This target used a flat foam with a face-on diagnostic line of sight. The aperture of this target was positioned along the side of the foam. Normally it is positioned along the top of the foam, which is located directly below the grid in this image. From this perspective we are looking through the Al plasma and the foam. This target geometry generated an orthogonal line of sight without moving the spherical crystal diagnostic.

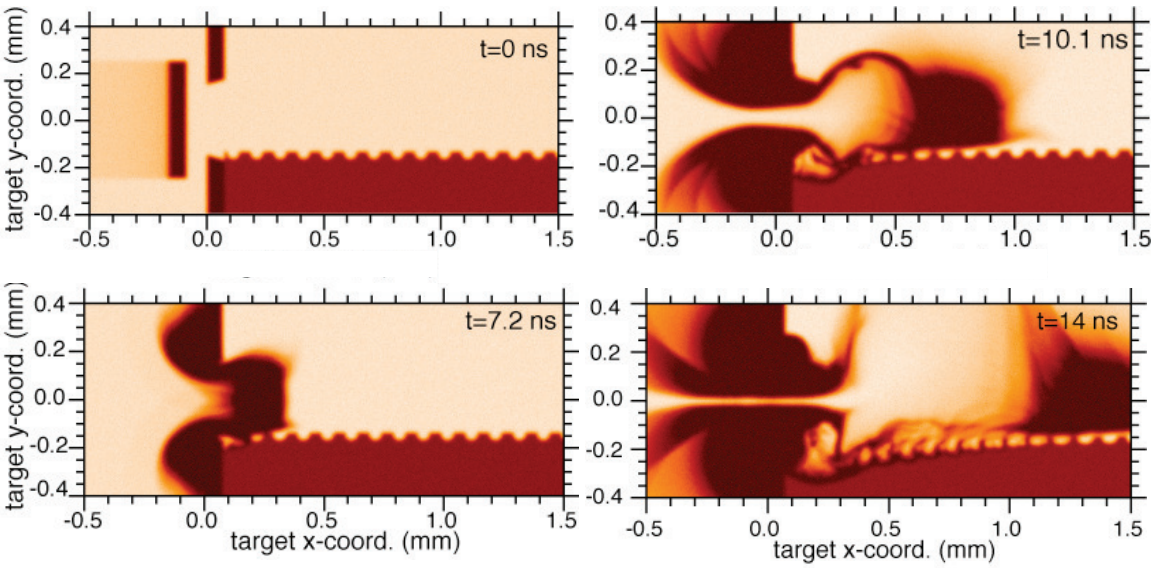

Figure B.8: Nike June 2007. Simulated radiographs from 2D FLASH simulations. The perturbations have $\lambda = 100$ μm and peak-to-valley amplitudes equal to 30 μm. The simulations were initialized using the pressure, velocity, and density output from 1D Hyades.

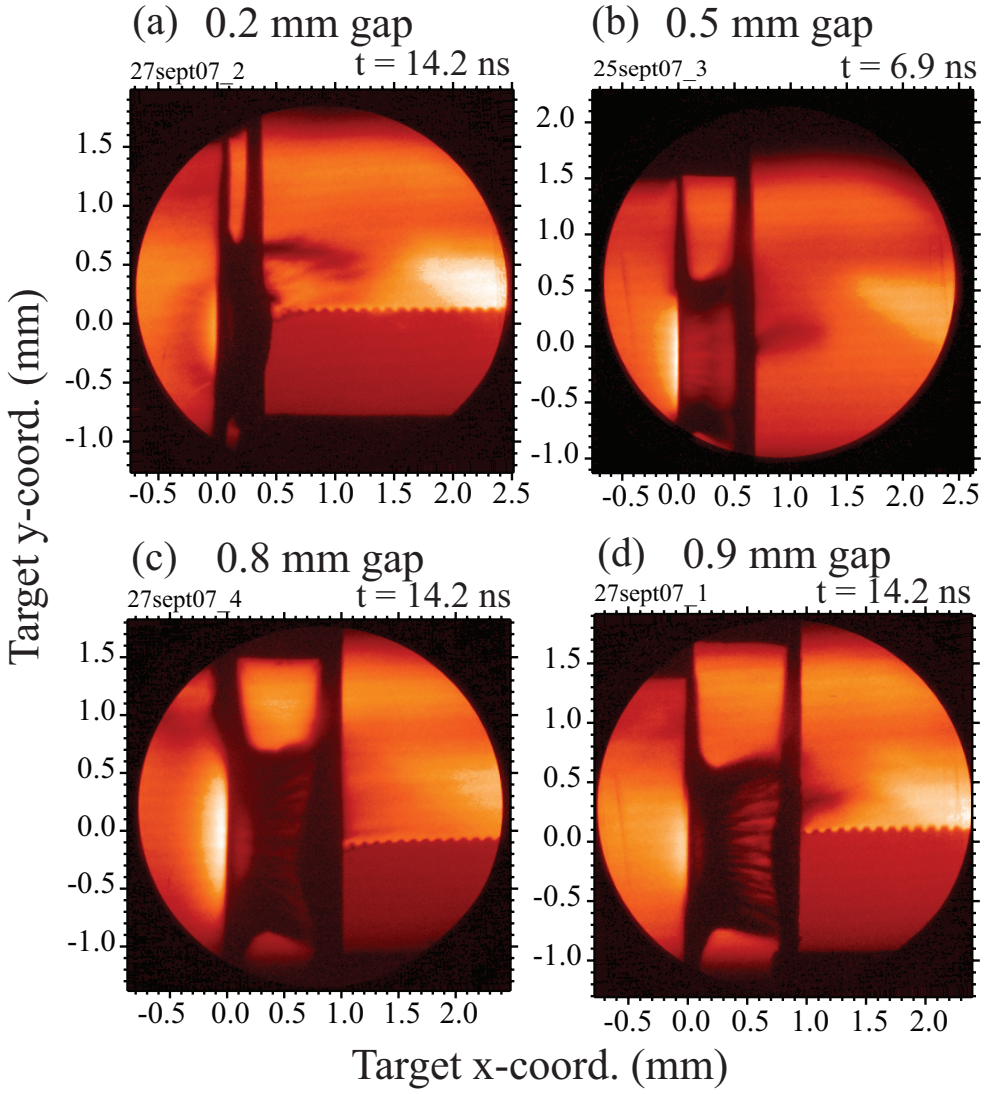

Figure B.9: Nike September 2007. These targets used slotted Au knife-edges that had a slot width equal to 400 μm. The gap between the rear of the Al foil and the front of the Au knife-edge was varied. All of the foams had perturbations with $\lambda = 100$ μm and peak-to-valley amplitudes equal to 30 μm. (a) and (d) These targets used a 10 μm Al foil coated with 20 μm Par-C. This was the same foil used for the June experiments. The clumping of the Al flow seen in the gap of image (d) was caused by the initial surface roughness of the Al foil. (b) Here a 10 μm Al foil coated with 10 μm Par-N was used. (c) Here a bare 13 μm Al foil with no coating was used. The direct irradiation of the Al foil resulted in more Al self-emission, which can be seen in the image on the laser side of the foil.

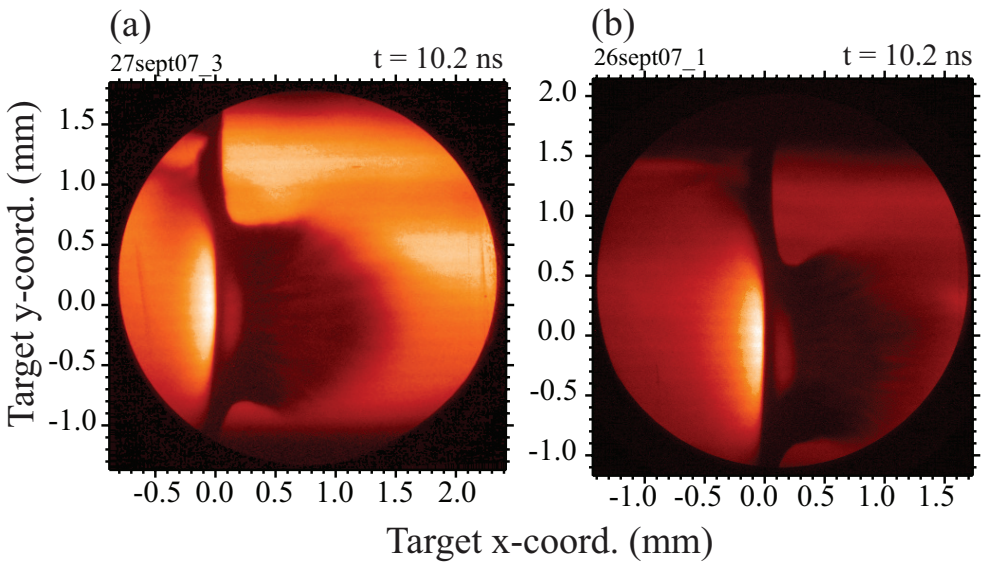

Figure B.10: Nike September 2007. (a) Image of an irradiated, bare Al foil that was initially 13 μm thick. (b) This target used a 10 μm thick Al foil coated with 10 μm Par-N. There is substantial Al self-emission which suggests that the plastic layer needed to be thicker in order to prevent the laser from irradiating the Al foil.

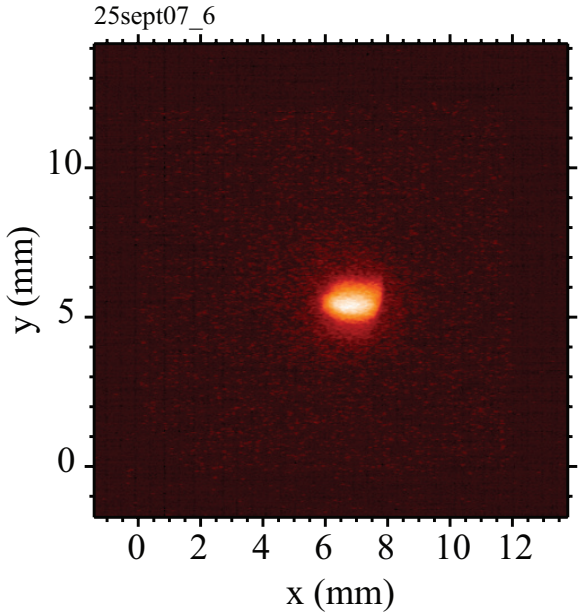

Figure B.11: Nike September 2007. This is an image of the backlighter x-ray source. The Fuji image plate was positioned in the image plane of the backlighter, which is at different location than the image plane of the target. The exact magnification of this image is not known, but it is greater than unity. We expect the x-ray source size to be approximately 0.5 mm.

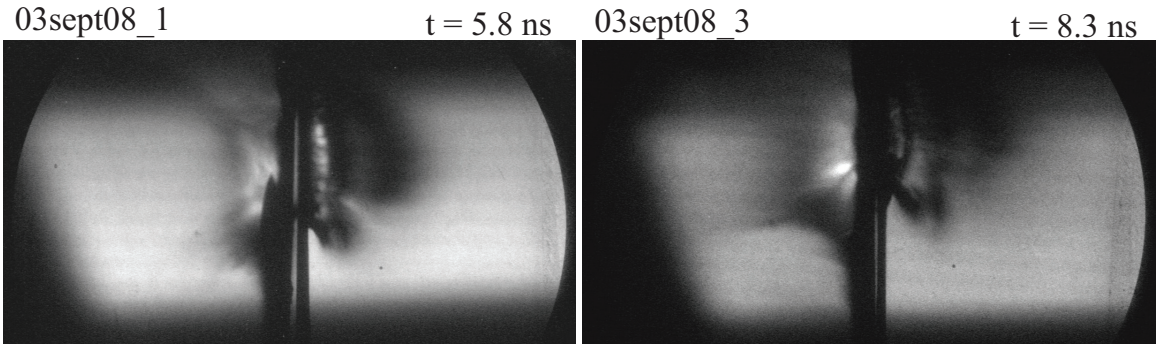

Figure B.12: Nike September 2008. In these two experiments the slotted Au knife-edge was located in front of the Al foil so that the laser first struck the Au. The Au was attached directly to the Al foil in order to minimize the size of the vacuum gap. A small gap can still be seen in these images.

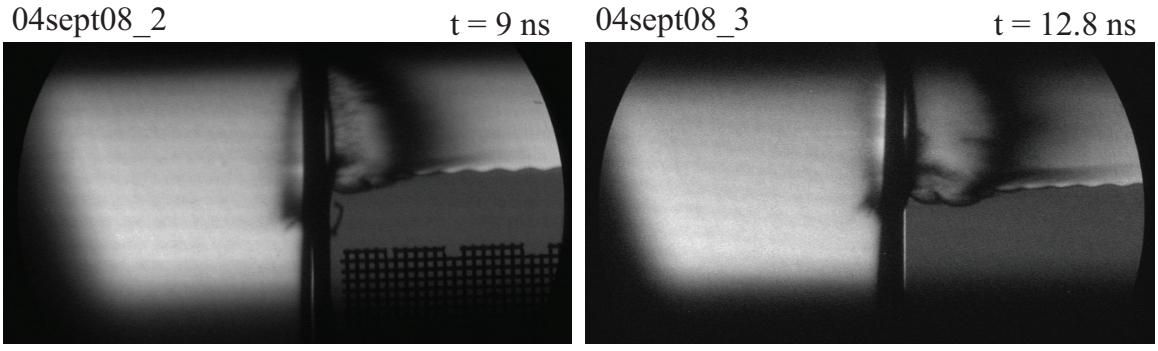

Figure B.13: Nike September 2008. In these two experiments the laser first struck the Al foil, which was attached directly to the slotted Au knife-edge so that there was no vacuum gap. The foam perturbations had $\lambda = 200$ μm and peak-to-valley amplitudes equal to 20 μm.

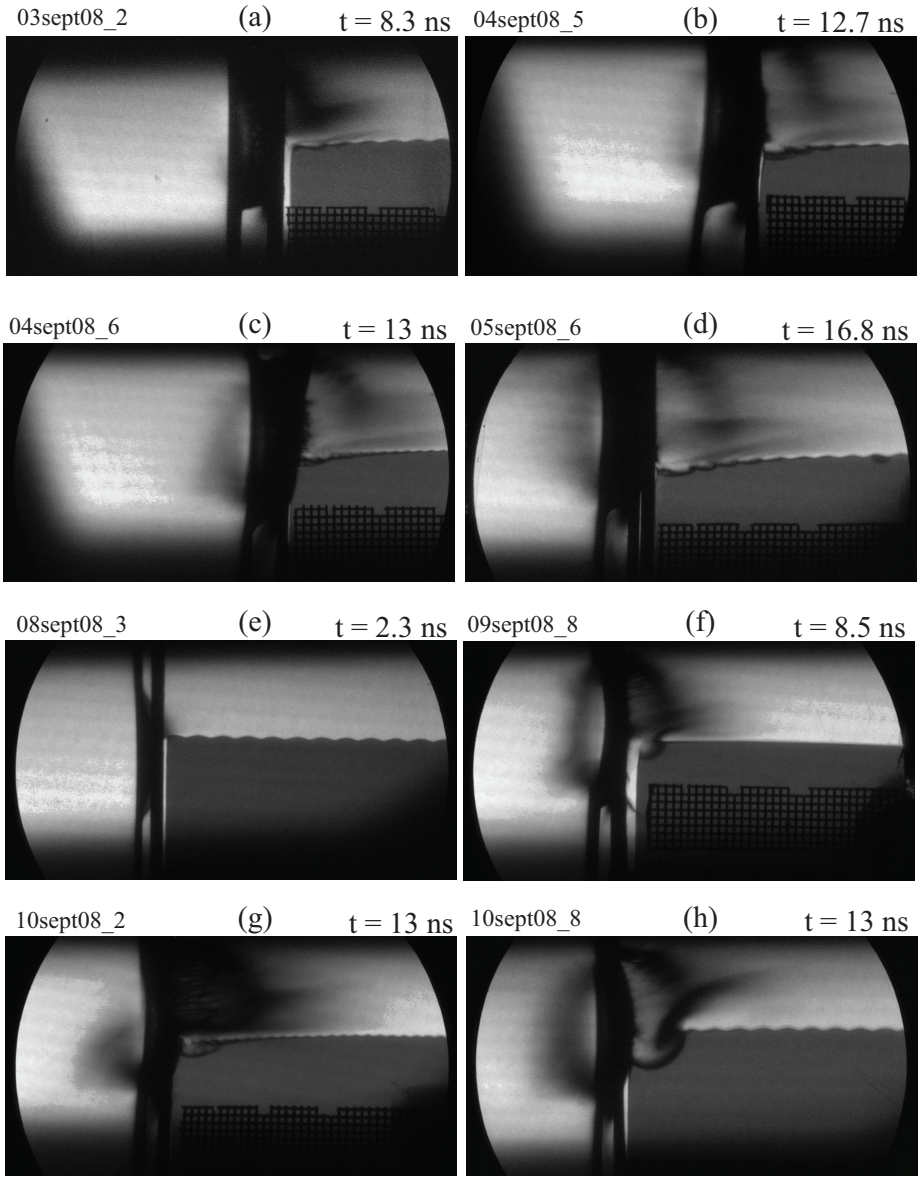

Figure B.14: Nike September 2008. Here are a variety of experiments. All of these experiments placed the Al in front of the knife-edge. (a) 300 μm vacuum gap and $\lambda = 200$ μm foam. (b) 300 μm vacuum gap and $\lambda = 200$ μm foam. (c) 300 μm vacuum gap and $\lambda = 100$ μm foam. (d) 150 μm vacuum gap and $\lambda = 200$ μm foam. Two knife-edge pieces were glued together in order to double the thickness. This prevented the shock in the knife-edge from breaking out before the image was captured. (e) 100 μm vacuum gap and $\lambda = 300$ μm foam. (f) 150 μm vacuum gap and flat foam. Knife-edge was misaligned. (g) 100 μm vacuum gap and $\lambda = 100$ μm foam. A knife-edge with no slot was used. The edge of a 75 μm Au foil was place at the perturbation position. Thus, the Al flow was not collimated. (h) 100 μm vacuum gap and $\lambda = 200$ μm foam. Slotted knife-edge was attached 100 μm below the nominal position. This is the same image that was shown in Fig. 2.3.

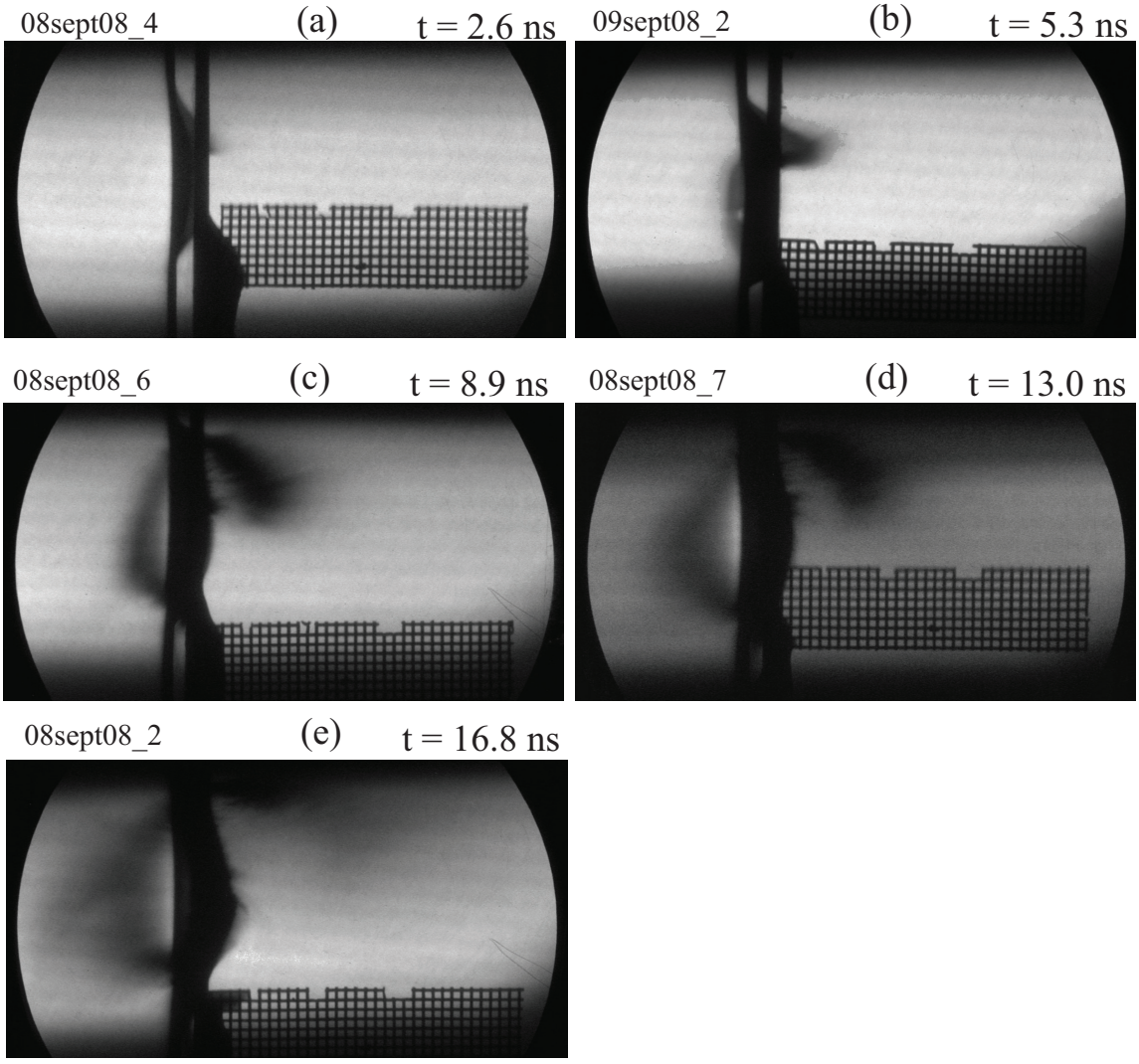

Figure B.15: Nike September 2008. Here is a series of experiments that was carried out to understand the behavior of the Al flow with no foam present. The vacuum gap was ~ 100 μm for each target.

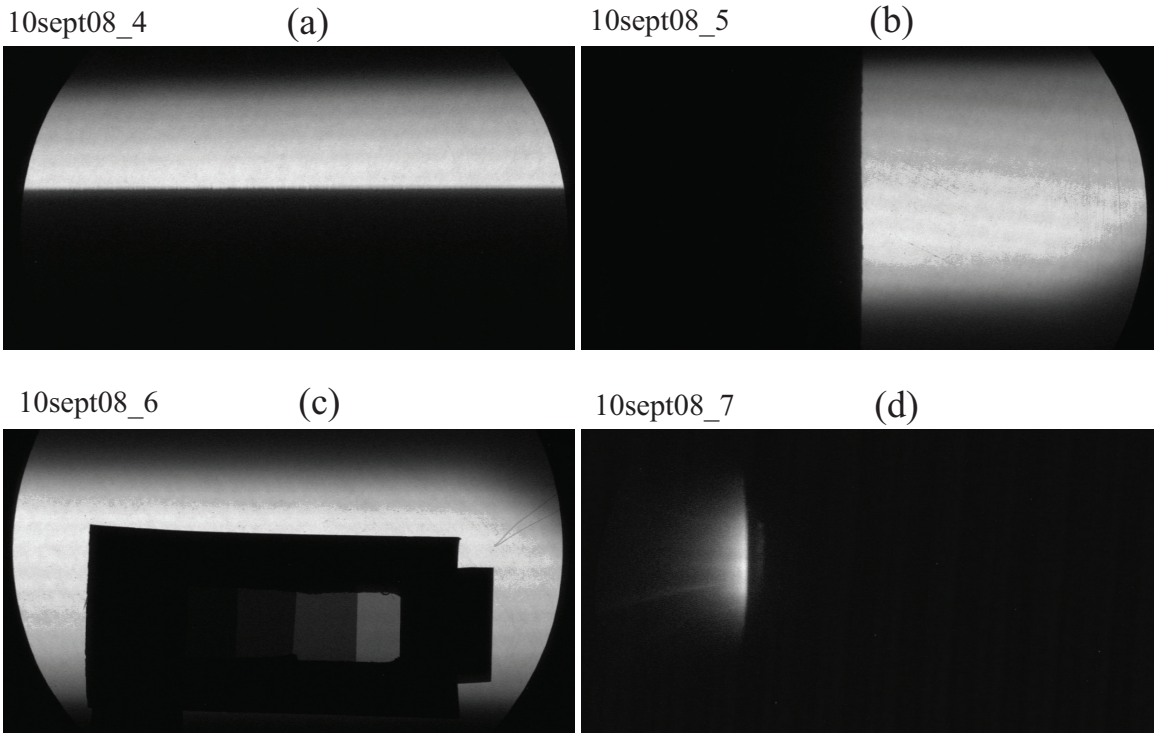

Figure B.16: Nike September 2008. (a) Radiograph of a horizontal razor blade that was located in the target plane. This was used to determine the vertical MTF. Only the backlighter beams were fired. (b) Radiograph of a vertical razor blade used to determine the horizontal MTF. Again only the backlighter beams were fired. (c) A polyimide step target was attached directly to the image plate in order to check the scaling of the values readout by the image plate scanner. The polyimide thicknesses, from left to right, were 100, 75, 50, and 25 μm. The tab on the far right was a 50 μm thick Au foil. (d) Here only the main beams were fired. Therefore, this is an image of the self emission from the laser driven surface and the ablated plasma.

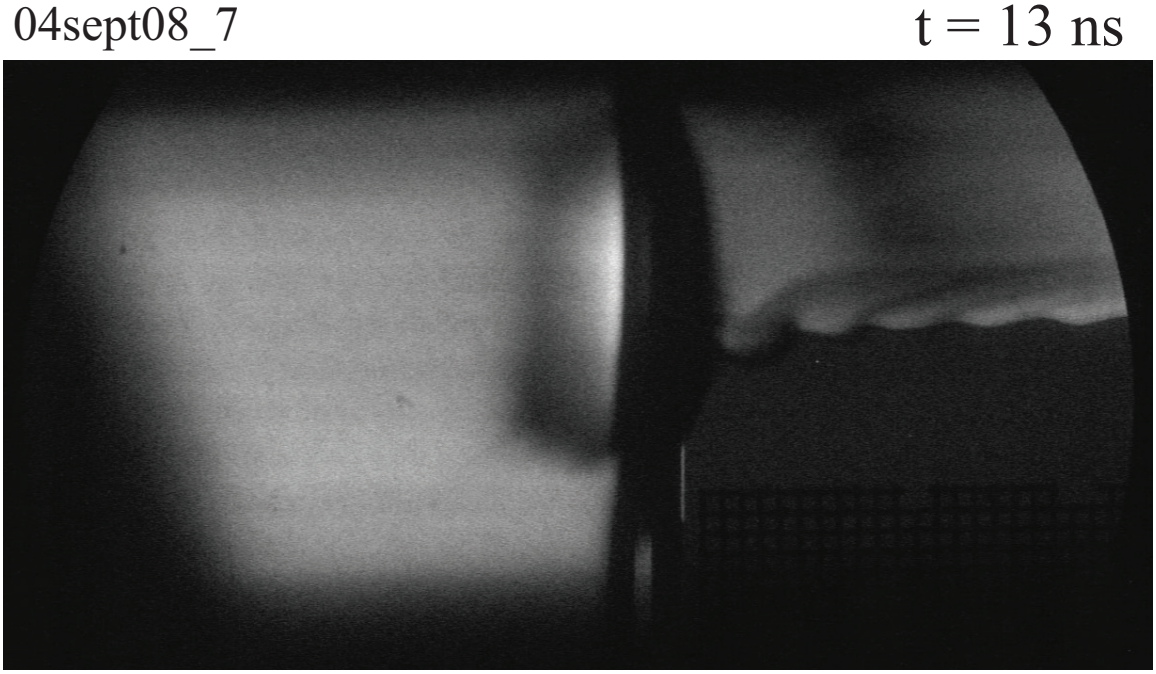

Figure B.17: Nike September 2008. This targets had foam perturbations with $\lambda = 300$ μm and peak-to-valley amplitudes equal to 30 μm. The vacuum gap was 100 μm. For this shot the backlighter energy was low.

APPENDIX C

Omega Shot Log and Additional Data from the KH Experiments on May 1, 2008

Below is the shot log for the Omega experiments that took place on May 1, 2008. This was an extended day that started at 8 am and ended at Midnight. A total of 16 targets were successfully shot. Twelve of these were the Supernova Rayleigh Taylor (SNRT) targets designed and shot by Carolyn Kuranz, while the remaining four targets were the KH type discussed in Chapter 4. The image shown in Fig. C.1 is a radiograph of the fourth KH target, which was not previously shown in Chapter 4. The design of the fourth target as well as the overall experimental setup was the same as discussed in Chapter 4, except that a Ti backlighter was used instead of the V backlighter. In addition, the 13 μm V filter located in front of the film was replaced with a 13 μm Ti filter as noted in the shot log. After two successful shots with the V backlighter we attempted to use the Ti backlighter because it had a smaller tapered aperture (10 and 20 μm diameters instead of 20 and 35 μm) that we hoped would increase the resolution. During the shot day the Ti backlighters were continually used for the SNRT experiments, and the PI's of that experiment graciously let us "borrow" one of their spares. The results were not as impressive as those that used the V backlighters. The bright spot seen in Fig. C.1 was present in

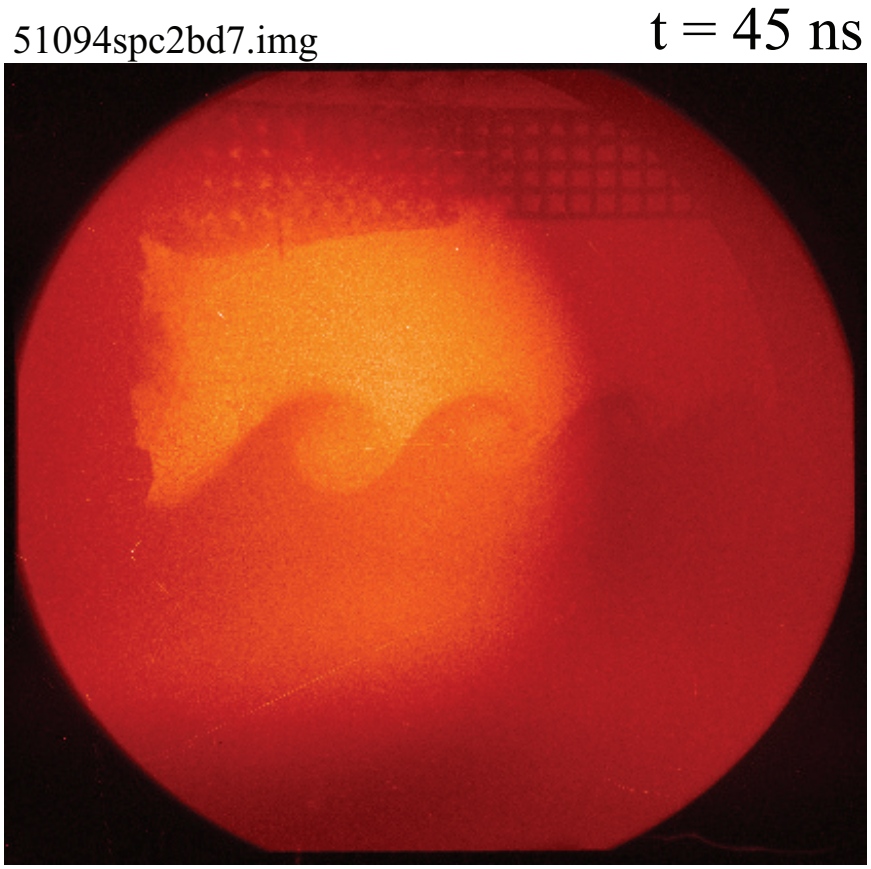

Figure C.1: This experiment used the same target and experimental setup that was presented in Chapter 4, except the V backlighter was replaced with a Ti backlighter. The energies associated the Ti He-α transitions are around 4.7 keV. The Ti backlighter was fabricated by our group at the University of Michigan. The pinhole was constructed from a 50 μm thick Ta foil and had diameters that were tapered from 10 to 20 μm.

many other radiographs that used the same Ti backlighter design. Its origin is not well understood, but it most likely resulted from the detection of high-energy x-rays that are generated somewhere on the backlighter target. Image processing techniques have been developed to minimize its effect on the data [107]. The grid in the upper right corner of the image appears fairly sharp suggesting the resolution was increased.

Shot Summary for Thursday, May 1, 2008

Targets:

Target1: Main targets, 3 types: SNRT51, SNRT424, KH
SNRT51- GA machined CHBr plug
SNRT424- Older 2-mode CHBr plug (2nd lamda=424μm)
KH- LLNL Be boxes w/Umich mounted acrylic shields
Inserted in to Tim1/P3

Target2: Ti backlighter, inserted in H2/TPS#2, BL2 pointing (10.717, 30.26, 145.88). Pinhole is 0.6mm towards Tim3c. Beams 55,56,58

Target3: Sc backlighter, inserted in H2/TPS#2, BL1 pointing (12666, 63.59, 348.88) Pinhole 0.7mm towards Tim6. Beams 20,21,28.

Target4: V backlighter, inserted in H2/TPS#2, BL2 pointing (10.717, 30.26, 145.88). Pinhole is 0.6mm towards Tim3c. Beams 55, 56,58.

Primary TIM Diagnostics :

TIM1: TIM TPS#1: to hold main target

TIM3: SPCA cranked
Pointing: (1581, 98.13, 88.60)
V or Ti Pinhole at ~10 mm opposite cranked TIM3

H2/ Tim TPS#2: to hold V,Ti, or Sc BL

TIM6: Straight
Pointing: (1300, 90, 72)
Sc Pinhole at ~12 mm to TIM4

Drive Group :	SG8 DPPs	33, 34, 36, 38, 41, 43, 48, 49, 63, 60
BL Group 1 (Sc BL):	-1000 um spot	21, 28, 20 (pointed at Sc BL, ((12666, 63.59,348.88))
BL Group 2 (Ti BL) :	1000 um spot	55, 56, 58 (pointed at Ti or V BL,(10.717, 30.26, 145.88))
Optional BL2 beams	1000 um spot	22,26,52,55,56,58 (pointed at V BL, (10.717,30.26,145.88))

If additional BL2 beams are needed turn them on in the following order: 22, 52, 26.

Secondary TIM Diagnostics : **HENEX linTIM4 Channel 1 not in use. 2-5 are in use**

Shot #	RID #	Target ID	Target type	Beamlines	Timing	Energy (J/beam)	<— r(μm)	Pointing θ(deg)	—> φ(deg)	Spot Size (μm)	TIM data	Other info
												Delay in beam alignment due to last night H2 TPS problem Base plan change: put B in TIM3 and leave there unless directed Dropped DANTE until KH shot-- concern about damage XRFC2 in TIM5 is looking at drive with 2x mag
1	**25036** 9:36 AM shot 51081	SNRT11 PH1	SNRT51	Drive group BL Group 1	-21ns t0	450 200	TCC 12666	TCC 63.59	TCC 348.88	SG8 DPP -1000		TIM6 good data, perhaps a bit dim
2	**25512** 10:33 AM shot 51082	SNRT8 PH2	SNRT51	Drive group BL Group 1	-25ns t0	450 300	TCC 12666	TCC 63.59	TCC 348.88	SG8 DPP -1000		Dropped HENEX -- pumping problem **Increased BL energy to 300 J** TIM6 better data, seem to see structure
3	**25449** 11:28 shot 51083	SNRT14 PH3	SNRT51	Drive group BL Group 1	-33ns t0	450 350	TCC 12666	TCC 63.59	TCC 348.88	SG8 DPP -1000		**Increased BL energy to 350 J** HENEX got dropped
4	25510 12:42 shot 51086	KH2 JFH_OSNRT4BL-30	KH	Drive group BL Group 2	-45ns t0	450 425	TCC 10717	TCC 30.26	TCC 145.88	SG8 DPP 1000		Dropped HENEX Confirmed V filter in TIM3 Target aligned with up to 200 μm error in box corner vs reticle Spectacular data
5	**25513** **13:41** **SHOT 51087**	SNRT10 PH4	SNRT51	Drive group BL Group 1	-29ns t0	450 350	TCC 12666	TCC 63.59	TCC 348.88	SG8 DPP -1000		Switched to D8 film Excellent data on TIM6 HENEX got data
6	**25514** 14:37 shot 51088	SNRT12 PH5	SNRT51	Drive group BL Group 1	-17ns t0	450 350	TCC 12666	TCC 63.59	TCC 348.88	SG8 DPP -1000		D8 film: excellent data TIM6 Target almost fell off HENEX acquired but did not see much
7	**25515** 13:37 shot 51089	SNRT16 PH6	SNRT51	Drive group BL Group 1	-13ns t0	450 400	TCC 12666	TCC 63.59	TCC 348.88	SG8 DPP -1000		D8 film: very good TIM6 data/ apparent bleedover HENEX got good data: no sign of signal above He alpha region Film in TIM6 was loaded with notch rotated 180 degrees from standard orientation but there was some other ofsetting rotation BL energy to 400
8	25037 16:44 shot 51090	KH1 JFH-OSNRT4BL-29	KH	Drive group BL Group 2	-45ns t0	450 425	TCC 10717	TCC 30.26	TCC 145.88	SG8 DPP 1000		Dropped HENEX D7 film
9	**25516** 17:43 shot 51091	SNRT36B PH7	424	Drive group BL Group 1	**-25 ns** t0	450 425	TCC 12666	TCC 63.59	TCC 348.88	SG8 DPP -1000		BL energy to 425 J D8 Excellent TIM6
10	25519 18:43 shot 51092	SNRT18 PH9	SNRT51	Drive group BL Group 1	**-21 ns** t0	450 **425**	TCC 12666	TCC 63.55	TCC 357.58	SG8 DPP -1000		Excellent TIM6 data: again apparent light leaks
11	25520 19:39 shot 51093	SNRT13 ~~PH13~~ **PH10**	SNRT51	Drive group BL Group 1	**-25 ns** t0	450 **425**	TCC 12666	TCC 63.55	TCC 357.58	SG8 DPP -1000		D8; excellent TIM6 data
12	25500 20:50 shot 51094	KH3 PHTi2	KH	Drive group BL Group 2	**-75 ns** t0	450 425	TCC 10717	TCC 26.99	TCC 150.95	SG8 DPP 1000		Dropped HENEX D7 1/2 mil Ti filter in TIM3 Drop BL 22, 26, 52 from SRF Retracted TIM2 Went to Ti BL and moved Ti filter to TIM3 Ti rear filter/ No rear filter Be SRF logbooks were updated after shot to be accurate Data had "spot", but was otherwise good. Hot spot existed in spite of having withdrawn the TIM behind the BL
13	25518 21:42 shot 51095	SNRT4 PH11	SNRT51	Drive group BL Group 1	**-33 ns** t0	450 425	TCC 12666	TCC 63.55	TCC 357.58	SG8 DPP -1000		D8 Excellent TIM6 data
14	25604 22:26 shot 51096	SNRT3 PH13 (Ti)	SNRT51	Drive group BL Group 1	**-21 ns** t0	450 **425**	TCC 12666	TCC 63.55	TCC 357.58	SG8 DPP -1000		Shot director had problem copying SRF D8: Good data but much fainter with Ti BL (TIM6)
												Shots 13 and 14 and 15 targets came in much earlier. **If this could happen every time, we would get more shots.**
15	25501 23:11 shot 51097	KH4 JFH-OSNRT4-31	KH	Drive group BL Group 2	-25ns t0	450 425	TCC 10717	TCC 30.26	TCC 145.88	SG8 DPP 1000		Dropped HENEX TIM 3 20 mil Be+ 1/2 mil V Dropped XRFC/ kept SPCA Targets were aligned at 36 min. Best KH target alignment of day Excellent TIM3 data
16	**25517** 23:57 shot 51098	SNRT6 PH8		Drive group BL Group 1	**-37 ns** t=0	450 425	TCC 12666	TCC 63.55	TCC 357.58	SG8 DPP -1000		D8 Aligned 41 min. after shot
		SNRT36A Not used JFH-OSNRT4-32 PH14 (Ti)	424									
~~10~~	~~25509~~	~~SNRT3~~ PHTi1	~~SNRT51~~	~~Drive group~~ BL Group 2	~~-33 ns~~ t0	~~450~~ 425	~~TCC~~ 10717	~~TCC~~ 30.26	~~TCC~~ 145.88	~~SG8 DPP~~ -1000		Delayed for now

BIBLIOGRAPHY

BIBLIOGRAPHY

[1] M. D. Cable, S. P. Hatchett, J. A. Caird, J. D. Kilkenny, H. N. Kornblum, S. M. Lane, C. Laumann, R. A. Lerche, T. J. Murphy, J. Murray, M. B. Nelson, D. W. Phillion, H. Powell, and D. B. Ress. Indirectly driven, high convergence inertial confinement fusion implosions. *Physical Review Letters*, 73(17):2316–2319, 1994.

[2] J. M. Soures, R. L. McCrory, C. P. Verdon, A. Babushkin, R. E. Bahr, T. R. Boehly, R. Boni, D. K. Bradley, D. L. Brown, R. S. Craxton, J. A. Delettrez, W. R. Donaldson, R. Epstein, P. A. Jaanimagi, S. D. Jacobs, K. Kearney, R. L. Keck, J. H. Kelly, T. J. Kessler, R. L. Kremens, J. P. Knauer, S. A. Kumpan, S. A. Letzring, D. J. Lonobile, S. J. Loucks, L. D. Lund, F. J. Marshall, P. W. McKenty, D. D. Meyerhofer, S. F. B. Morse, A. Okishev, S. Papernov, G. Pien, W. Seka, R. Short, M. J. Shoup, M. Skeldon, S. Skupsky, A. W. Schmid, D. J. Smith, S. Swales, M. Wittman, and B. Yaakobi. Direct-drive laser-fusion experiments with the omega, 60-beam, >40 kj, ultraviolet laser system. *Physics of Plasmas*, 3(5):2108–2112, 1996.

[3] C. L. Ruiz, G. W. Cooper, S. A. Slutz, J. E. Bailey, G. A. Chandler, T. J. Nash, T. A. Mehlhorn, R. J. Leeper, D. Fehl, A. J. Nelson, J. Franklin, and L. Ziegler. Production of thermonuclear neutrons from deuterium-filled capsule implosions driven by z-pinch dynamic hohlraums. *Physical Review Letters*, 93(1):4, 2004.

[4] J.D. Lindl, P. Amendt, R.L. Berger, S.G. Glendinning, S.H. Glenzer, S.W. Haan, R.L. Kauffman, O.L. Landen, and L.J. Suter. The physics basis for ignition using indirect-drive targets on the national ignition facility. *Physics of Plasmas*, 11(2):339–491, FEB 2004.

[5] W. A. Stygar, M. E. Cuneo, D. I. Headley, H. C. Ives, R. J. Leeper, M. G. Mazarakis, C. L. Olson, J. L. Porter, T. C. Wagoner, and J. R. Woodworth. Architecture of petawatt-class z-pinch accelerators. *Physical Review Special Topics-Accelerators And Beams*, 10(3), MAR 2007.

[6] S.P. Obenschain, D.G. Colombant, A.J. Schmitt, J.D. Sethian, and M.W. McGeoch. Pathway to a lower cost high repetition rate ignition facility. *Physics of Plasmas*, 13(5), MAY 2006.

[7] Jonathan Medalia. Comprehensive nuclear-test-ban treaty: Background and current developments. *Congressal Research Service Report for Congress*, page 47, 2008.

[8] J. Nuckolls, L. Wood, A. Thiessen, and G. Zimmerman. Laser compression of matter to super-high densities: Thermonuclear (CTR) applications. *Nature*, 239:139–142, September 1972.

[9] D. Ryutov, R.P. Drake, J. Kane, E. Liang, B.A. Remington, and W.M. Wood-Vasey. Similarity criteria for the laboratory simulation of supernova hydrodynamics. *Astrophysical Journal*, 518:821–832, JUN 20 1999.

[10] B.A. Remington, D. Arnett, R.P. Drake, and H. Takabe. Experimental astrophysics - modeling astrophysical phenomena in the laboratory with intense lasers. *Science*, 284(5419):1488–1493, MAY 28 1999.

[11] B. A. Remington, R. P. Drake, and D. D. Ryutov. Experimental astrophysics with high power lasers and z pinches. *Reviews of Modern Physics*, 78(3):755–807, 2006.

[12] H. F. Robey, J. O. Kane, B. A. Remington, R. P. Drake, O. A. Hurricane, H. Louis, R. J. Wallace, J. Knauer, P. Keiter, D. Arnett, and D. D. Ryutov. An experimental testbed for the study of hydrodynamic issues in supernovae. *Physics of Plasmas*, 8(5):2446–2453, 2001.

[13] P. Hartigan, J. M. Foster, B. H. Wilde, R. F. Coker, P. A. Rosen, J. F. Hansen, B. E. Blue, R. J. R. Williams, R. Carver, and A. Frank. Laboratory experiments, numerical simulations, and astronomical observations of deflected supersonic jets: Application to hh 110. *Astrophysical Journal*, 705(1):1073–1094, NOV 1 2009.

[14] A. B. Reighard, R. P. Drake, K. K. Dannenberg, D.J. Kremer, M. Grosskopf, E. C. Harding, D. R. Leibrandt, S. G. Glendinning, T. S. Perry, B. A. Remington, J. Greenough, J. Knauer, T. Boehly, S. Bouquet, L. Boireau, M. Koenig, and T. Vinci. Observation of collapsing radiative shocks in laboratory experiments. *Physics of Plasmas*, 13(8), AUG 2006.

[15] G.W. Collins, L.B. Da Silva, P. Celliers, D.M. Gold, M.E. Foord, R.J. Wallace, A. Ng, S.V. Weber, K.S. Budil, and R. Cauble. Measurements of the equation of state of deuterium at the fluid insulator-metal transition. *Science*, 281(5380):1178–1181, AUG 21 1998.

[16] J. E. Bailey, G. A. Rochau, R. C. Mancini, C. A. Iglesias, J. J. MacFarlane, I. E. Golovkin, C. Blancard, P.H. Cosse, and G. Faussurier. Experimental investigation of opacity models for stellar interior, inertial fusion, and high energy density plasmas. *Physics of Plasmas*, 16(5), May 2009.

[17] J. Guzman and T. Plewa. Non-spherical core-collapse supernovae: evolution towards homologous expansion. *Nonlinearity*, 22:2775–2797, 2009.

[18] C. C. Kuranz, R. P. Drake, M. J. Grosskopf, A. Budde, C. Krauland, D. C. Marion, A. J. Visco, J. R. Ditmar, H. F. Robey, B. A. Remington, A. R. Miles,

A. B. R. Cooper, C. Sorce, T. Plewa, N. C. Hearn, K. L. Killebrew, J. P. Knauer, D. Arnett, and T. Donajkowski. Three-dimensional blast-wave-driven rayleigh-taylor instability and the effects of long-wavelength modes. *Physics of Plasmas*, 16(5), MAY 2009.

[19] J. H. Eggert, D. G. Hicks, P. M. Celliers, D. K. Bradley, R. S. McWilliams, R. Jeanloz, J. E. Miller, T. R. Boehly, and G. W. Collins. Melting temperature of diamond at ultrahigh pressure. *Nature Physics*, 6(1):40–43, Jan 2010.

[20] W.T. Chu, B.A. Ludewigt, and T.R. Renner. Instrumentation for treatment of cancer using proton and light-ion beams. *Review of Scientific Instruments*, 64(8):2055–2122, AUG 1993.

[21] Lord Kelvin. Influence of wind and capillarity on waves in water supposed frictionless. *Mathematical and Physical Papers*, 4:76–85, 1871.

[22] H. Helmholtz. On discontinuous movements of fluids. *Philosophical Magazine*, 36(244):337–346, 1868.

[23] Lord Rayleigh. Investigation of the character of the equilibrium of an incompressible heavy fluid of variable density. *Proc. London Math Soc.*, 14:170, 1882.

[24] G.I. Taylor. The instability of liquid surfaces when accelerated in a direction perpendicular to their planes. *Proc. Roy. Soc. A*, 201:192–196, 1950.

[25] R. D. Richtmyer. Taylor instability in shock acceleration of compressible fluids. *Communications on Pure and Applied Mathematics*, 13(2):297–319, 1960.

[26] E.E. Meshkov. Instability of the interface of two gases accelerated by a shock wave. *Fluid Dyanmics*, 4(5):101, 1969.

[27] Stefano Atzeni and Jürgen Meyer-ter Vehn. *The physics of inertial fusion : beam plasma interaction, hydrodynamics, hot dense matter*. Oxford University Press, Oxford, 2004.

[28] P. Diamond, D. Eardley, J. Katz, S. Koonin, C. Max, D. Meiron, F. Perkins, and M. Rosenbluth. Shock obliquity and stability in inertial confinement fusion. JASON Report No. JSR-92-325, MITRE Corporation, 1993.

[29] K. O. Mikaelian. Oblique shocks and the combined Rayleigh-Taylor, Kelvin-Helmholtz, and Richtmyer-Meshkov instabilities. *Physics of Fluids*, 6(6):1943–1945, 1994.

[30] K. Kifonidis, T. Plewa, H. T. Janka, and E. Muller. Non-spherical core collapse supernovae - I. neutrino-driven convection, rayleigh-taylor instabilities, and the formation and propagation of metal clumps. *Astronomy & Astrophysics*, 408(2):621–649, 2003.

[31] J. C. Wheeler, J. R. Maund, and S. M. Couch. The shape of Cas A. *Astrophysical Journal*, 677(2):1091–1099, 2008.

[32] MP Ciamarra, A Coniglio, and M Nicodemi. Shear instabilities in granular mixtures. *Physical Review Letters*, 94(18), MAY 13 2005.

[33] B. A. Hammel, J. D. Kilkenny, D. Munro, B. A. Remington, H. N. Kornblum, T. S. Perry, D. W. Phillion, and R. J. Wallace. X-ray radiographic imaging of hydrodynamic phenomena in radiation-driven materials - shock propagation, material compression, and shear-flow. *Physics of Plasmas*, 1(5):1662–1668, 1994.

[34] L. K. Ang, Y. Y. Lau, R. M. Gilgenbach, H. L. Spindler, J. S. Lash, and S. D. Kovaleski. Surface instability of multipulse laser ablation on a metallic target. *Journal of Applied Physics*, 83(8):4466–4471, 1998.

[35] J. Kane, D. Arnett, B.A. Remington, S.G. Glendinning, J. Castor, R. Wallace, A. Rubenchik, and B.A. Fryxell. Supernova-relevant hydrodynamic instability experiments on the nova laser. *Astrophysical Journal*, 478(2, Part 2), APR 1 1997.

[36] C. C. Kuranz, R. P. Drake, E. C. Harding, M. J. Grosskopf, H. F. Robey, B. A. Remington, M. J. Edwards, A. R. Miles, T. S. Perry, B. E. Blue, T. Plewa, N. C. Hearn, J. P. Knauer, D. Arnett, and D. R. Leibrandt. Two-dimensional blast-wave-driven rayleigh-taylor instability: Experiment and simulation. *Astrophysical Journal*, 696(1):749–759, 2009.

[37] P. Ramaprabhu, G. Dimonte, Y. Young, A. C. Calder, and B. Fryxell. Limits of the potential flow approach to the single-mode rayleigh-taylor problem. *Physical Review E*, 74(6, Part 2), DEC 2006.

[38] C. C. Kuranz, R. P. Drake, M. J. Grosskopf, B. Fryxell, A. Budde, J. F. Hansen, A. R. Miles, T. Plewa, N. Hearn, and J. Knauer. Spike morphology in blast-wave-driven instability experiments. *Physics of Plasmas*, 17(1), (in press) 2010.

[39] E. Gutmark, T. P. Parr, D. M. Hansonparr, and K. C. Schadow. On the role of large and small-scale structures in combustion control. *Combustion Science and Technology*, 66(1-3):107–126, 1989.

[40] S. A. Thorpe. Transitional phenomena and the development of turbulence in stratified fluids - a review. *Journal of Geophysical Research-Oceans*, 92(C5):5231–5248, 1987.

[41] I. P. D. DeSilva, H. J. S. Fernando, F. Eaton, and D. Hebert. Evolution of Kelvin-Helmholtz billows in nature and laboratory. *Earth and Planetary Science Letters*, 143(1-4):217–231, 1996.

[42] R. G. Jahn. The refraction of shock waves at a gaseous interface. *Journal of Fluid Mechanics*, 1(5):457–489, 1956.

[43] A.M. Abdelfattah and L.F. Henderson. Shock-waves at a fast-slow gas interface. *Journal of Fluid Mechanics*, 86(MAY):15–32, 1978.

[44] A.M. Abdelfattah and L.F. Henderson. Shock-waves at a slow-fast gas interface. *Journal of Fluid Mechanics*, 89(NOV):79–95, 1978.

[45] J.F. Hawley and N.J. Zabusky. Vortex paradigm for shock-accelerated density-stratified interfaces. *Physical Review Letters*, 63(12):1241–1244, SEP 18 1989.

[46] L. F. Henderson, E.I. Vasilev, G. Ben-Dor, and T. Elperin. The wall-jetting effect in mach reflection: theoretical consideration and numerical investigation. *Journal of Fluid Mechanics*, 479:259–286, MAR 25 2003.

[47] G.L. Brown and Roshko A. Density effects and large structure in turbulent mixing layers. *Journal of Fluid Mechanics*, 64(JUL24):775–816, 1974.

[48] S.A. Thorpe. Experiments on instability of stratified shear flows - miscible fluids. *Journal of Fluid Mechanics*, 46(MAR29):299–319, 1971.

[49] D.W. Bogdanoff. Compressibility effects in turbulent shear layers. *AIAA Journal*, 21(6):926–927, 1983.

[50] D. Papamoschou and A. Roshko. The compressible turbulent shear-layer - an experimental-study. *Journal of Fluid Mechanics*, 197:453–477, 1988.

[51] T. R. Boehly, D. L. Brown, R. S. Craxton, R. L. Keck, J. P. Knauer, J. H. Kelly, T. J. Kessler, S. A. Kumpan, S. J. Loucks, S. A. Letzring, F. J. Marshall, R. L. McCrory, S. F. B. Morse, W. Seka, J. M. Soures, and C. P. Verdon. Initial performance results of the omega laser system. *Optics Communications*, 133(1-6):495–506, 1997.

[52] S. P. Obenschain, S. E. Bodner, D. Colombant, K. Gerber, R. H. Lehmberg, E. A. McLean, A. N. Mostovych, M. S. Pronko, C. J. Pawley, A. J. Schmitt, J. D. Sethian, V. Serlin, J. A. Stamper, C. A. Sullivan, J. P. Dahlburg, J. H. Gardner, Y. Chan, A. V. Deniz, J. Hardgrove, T. Lehecka, and M. Klapisch. The nike krf laser facility: Performance and initial target experiments. *Physics of Plasmas*, 3(5):2098–2107, 1995.

[53] J. L. Weaver, J. Oh, B. Afeyan, L. Phillips, J. Seely, U. Feldman, C. Brown, M. Karasik, V. Serlin, Y. Aglitskiy, A. N. Mostovych, G. Holland, S. Obenschain, L-Y. Chan, D. Kehne, R. H. Lehmberg, A. J. Schmitt, D. Colombant, and A. Velikovich. Laser plasma instability experiments with krf lasers. *Physics of Plasmas*, 14(5), MAY 2007.

[54] E. C. Harding, R. P. Drake, Y. Aglitskiy, R. S. Gillespie, M. J. Grosskopf, J.L. Weaver, A. Velikovich, A. Visco, and J.R. Ditmar. Experimental design to generate strong shear layers in a high-energy-density plasma. *High Energy Density Physics*, in press (2010).

[55] E. C. Harding, R. P. Drake, Y. Aglitskiy, T. Plewa, R. S. Gillespie, M. J. Grosskopf, J.L. Weaver, A. Velikovich, A. Visco, and J.R. Ditmar. Laser driven supersonic flow over a compressible foam surface on the nike laser. *Physics of Plamas*, in press (2010).

[56] E. C. Harding, J. F. Hansen, O. A. Hurricane, R. P. Drake, H. F. Robey, C. C. Kuranz, B. A. Remington, M. J. Bono, M. J. Grosskopf, and R. S. Gillespie. Observation of a kelvin-helmholtz instability in a high-energy-density plasma on the omega laser. *Physical Review Letters*, 103(4):045005–4, 2009.

[57] O. A. Hurricane. Design for a high energy density Kelvin-Helmholtz experiment. *High Energy Density Physics*, 4(3-4):97–102, 2008.

[58] O. A. Hurricane, J. F. Hansen, H. F. Robey, B. A. Remington, M. J. Bono, E. C. Harding, R. P. Drake, and C. C. Kuranz. A high energy density shock driven Kelvin-Helmholtz shear layer experiment. *Physics of Plasmas*, 16(5):056305, 2009.

[59] E. C. Harding and R. P. Drake. Three-dimensional model of x-ray induced microchannel plate output. *Review of Scientific Instruments*, 77(10), OCT 2006. 16th Topical Conference on High-Temperature Plasma Diagnostics, Williamsburg, VA, MAY 07-11, 2006.

[60] D. Martinez, R. Presura, S. Wright, C. Plechaty, S. Neff, L. Wanex, and D. J. Ampleford. Generation of shear flow in conical wire arrays with a center wire. *Astrophysics and Space Science*, 322(1-4):205–208, 2009.

[61] S. Wright, R. Presura, A. Esaulov, S. Neff, C. Plechaty, D. Martinez, and A. Haboub. Kelvin-helmholtz instabilities actuated by an external magnetic field. *Astrophysics and Space Science*, 322(1-4):201–204, 2009.

[62] Y. Aglitskiy, T. Lehecka, S. Obenschain, S. Bodner, C. Pawley, K. Gerber, J. Sethian, C. M. Brown, J. Seely, U. Feldman, and G. Holland. High-resolution monochromatic x-ray imaging system based on spherically bent crystals. *Applied Optics*, 37(22):5253–5261, 1998.

[63] S. Chandrasekhar. *Hydrodynamic and Hydromagnetic Stability.* Dover, New York, 1961.

[64] A. Rikanati, U. Alon, and D. Shvarts. Vortex-merger statistical-mechanics model for the late time self-similar evolution of the kelvin-helmholtz instability. *Physics of Fluids*, 15(12):3776–3785, 2003.

[65] J. T. Larsen and S. M. Lane. Hyades - a plasma hydrodynamics code for dense-plasma studies. In *Radiative Properties of Hot Dense Matter*, pages 179–186, Santa Barbara, Ca, 1992. Pergamon-Elsevier Science Ltd.

[66] B. Fryxell, K. Olson, P. Ricker, F. X. Timmes, M. Zingale, D. Q. Lamb, P. MacNeice, R. Rosner, J. W. Truran, and H. Tufo. Flash: An adaptive mesh hydrodynamics code for modeling astrophysical thermonuclear flashes. *Astrophysical Journal Supplement Series*, 131(1):273–334, 2000.

[67] J. M. Foster, B. H. Wilde, P. A. Rosen, R. J. R. Williams, B. E. Blue, R. F. Coker, R. P. Drake, A. Frank, P. A. Keiter, A. M. Khokhlov, J. P. Knauer, and T. S. Perry. High-energy-density laboratory astrophysics studies of jets and bow shocks. *Astrophysical Journal*, 634(1):L77–L80, 2005.

[68] B. E. Blue, H. F. Robey, S. G. Glendinning, M. J. Bono, S. C. Burkhart, J. R. Celeste, R. F. Coker, R. L. Costa, S. N. Dixit, J. M. Foster, J. F. Hansen, C. A. Haynam, M. R. Hermann, J. P. Holder, W. W. Hsing, D. H. Kalantar, N. E. Lanier, D. A. Latray, H. Louis, B. J. MacGowan, G. R. Maggelssen, C. D. Marshall, E. I. Moses, A. J. Nikitin, D. W. O'Brien, T. S. Perry, M. W. Poole, V. V. Rekow, P. A. Rosen, M. B. Schneider, P. E. Stry, B. M. Van Wonterghem, R. Wallace, S. V. Weber, B. H. Wilde, D. T. Woods, and B. K. Young. Three-dimensional hydrodynamic experiments on the national ignition facility. *Physics of Plasmas*, 12, 2005.

[69] R. F. Coker, B. H. Wilde, J. M. Foster, B. E. Blue, P. A. Rosen, R. J. R. Williams, P. Hartigan, A. Frank, and C. A. Back. Numerical simulations and astrophysical applications of laboratory jets at Omega. *Astrophysics and Space Science*, 307(1-3):57–62, 2007.

[70] S. V. Lebedev, J. P. Chittenden, F. N. Beg, S. N. Bland, A. Ciardi, D. Ampleford, S. Hughes, M. G. Haines, A. Frank, E. G. Blackman, and T. Gardiner. Laboratory astrophysics and collimated stellar outflows: The production of radiatively cooled hypersonic plasma jets. *Astrophysical Journal*, 564(1):113–119, 2002.

[71] J. F. Hansen, H. F. Robey, R. I. Klein, and A. R. Miles. Experiment on the mass-stripping of an interstellar cloud in a high mach number post-shock flow. *Physics of Plasmas*, 14(5):056505, 2007.

[72] L. Landau. Stability of tangential discontinuities in compressible fluid. *Comptes Rendus (Doklady) de l'Academie des Sciences de l'URSS*, 44(4):139–141, 1944.

[73] L. D. Landau and E. M. Lifshitz. *Fluid Mechanics*. Pergamon Press, Oxford, England, 1987.

[74] R. A. Gerwin. Stability of interface between 2 fluids in relative motion. *Reviews of Modern Physics*, 40(3):652, 1968.

[75] W. Blumen, P. G. Drazin, and D. F. Billings. Shear layer instability of an inviscid compressible fluid. Part 2. *Journal of Fluid Mechanics*, 71(SEP23):305–316, 1975.

[76] A. L. Velikovich. Analytic theory of richtmyer-meshkov instability for the case of reflected rarefaction wave. *Physics of Fluids*, 8(6):1666–1679, 1996.

[77] D. Salzmann. *Atomic physics in hot plasmas*. International series of monographs on physics. Oxford University Press, New York, 1998.

[78] R. P. Drake. *High-Energy-Density Physics: Fundamentals, Inertial Fusion and Experimental Astrophysics*. Shock wave and high pressure phenomena. Springer, New York, 2006.

[79] J.D. Anderson. *Modern compressible flow, with historical perspective*. McGraw-Hill series in mechanical engineering. McGraw-Hill, New York, 1981.

[80] H. W. Liepmann and A. Roshko. *Elements of gasdynamics*. Galcit aeronautical series. Wiley, New York, 1957.

[81] A. M. Abdelfattah and L. F. Henderson. Shock-waves at a fast-slow gas interface. *Journal of Fluid Mechanics*, 86(May):15, 1978.

[82] L.F. Henderson. Refraction of a plane shock wave at a gas interface. *Journal of Fluid Mechanics*, 26:607, 1966.

[83] Ia B. Zeldovich and Iu P. Raizer. *Physics of shock waves and high-temperature hydrodynamics*. Fizika udarnykh voln i vysoktemperaturnykh gidrod. Academic Press, New York, 1966.

[84] P. E. Dimotakis. The mixing transition in turbulent flows. *Journal of Fluid Mechanics*, 409:69–98, 2000.

[85] H. F. Robey, Y. Zhou, A. C. Buckingham, P. Keiter, B. A. Remington, and R. P. Drake. The time scale for the transition to turbulence in a high reynolds number, accelerated flow. *Physics of Plasmas*, 10(3):614–622, 2003.

[86] J. G. Clerouin, M. H. Cherfi, and G. Zerah. The viscosity of dense plasmas mixtures. *Europhysics Letters*, 42(1):37–42, 1998.

[87] P. E. Dimotakis. Turbulent free shear layer mixing and combustion. In S. N. B. Murthy and E.T. Curran, editors, *Progress in Astronautics and Aeronautics*, volume 137, pages 265–340. AIAA, Washington, DC, 1991.

[88] L.P. Bernal and A. Roshko. Streamwise vortex structure in plane mixing layers. *Journal of Fluid Mechanics*, 170:499–525, SEP 1986.

[89] R.P. Drake. Design of flyer-plate-driven compressible turbulent mix experiments using z. *Physics of Plasmas*, 9(8):3545–3551, AUG 2002.

[90] H.S. Park, D.M. Chambers, H.K. Chung, R.J. Clarke, R. Eagleton, E. Giraldez, T. Goldsack, R. Heathcote, N. Izumi, M.H. Key, J.A. King, J.A. Koch, O.L. Landen, A. Nikroo, P.K. Patel, D.F. Price, B.A. Remington, H.F. Robey,

R.A. Snavely, D.A. Steinman, R.B. Stephens, C. Stoeckl, M. Storm, M. Tabak, W. Theobald, R.P.J. Town, J.E. Wickersham, and B.B. Zhang. High-energy k alpha radiography using high-intensity, short-pulse lasers. *Physics of Plasmas*, 13(5), MAY 2006. 47th Annual Meeting of the Division of Plasma Physics of the American-Physical-Society, Denver, CO, OCT 24-28, 2005.

[91] M. P. Kowalski, G. G. Fritz, R. G. Cruddace, A. E. Unzicker, and N. Swanson. Quantum efficiency of cesium iodide photocathodes at soft-x-ray and extreme ultraviolet wavelengths. *Applied Optics*, 25(14):2440–2446, Jul 1986.

[92] M. E. Lowenstern, E. C. Harding, C. M. Huntington, A. J. Visco, G. Rathore, and R. P. Drake. Performance of au transmission photocathode on a microchannel plate detector. *Review of Scientific Instruments*, 79(10), OCT 2008. 17th Topical Conference on High-Temperature Plasma Diagnostics, Albuquerque, NM, 2008.

[93] O.L. Landen, D.R. Farley, S.G. Glendinning, L.M. Logory, P.M. Bell, J.A. Koch, F.D. Lee, D.K. Bradley, D.H. Kalantar, C.A. Back, and R.E. Turner. X-ray backlighting for the national ignition facility (invited). *Review of Scientific Instruments*, 72(1, Part 2):627–634, JAN 2001. 13th Topical Conference on High-Temperature Plasma diagnostics, Tucson, AZ, JUN 18-22, 2000.

[94] J.D. Carpenter, G.W. Fraser, N.P. Bannister, and R. Fairbend. An analysis of microchannel plate composition and its effect on extreme ultraviolet quantum efficiency. *Nuclear Instruments & Methods In Physics Research Section A-Accelerators Spectrometers Detectors And Associated Equipment*, 573(1-2):232–235, APR 1 2007. 7th International Conference on Position-Senstive Detectors, Liverpool, England, SEP 09-13, 2005.

[95] B. L. Henke, E. M. Gullikson, and J. C. Davis. X-ray interactions - photoabsorption, scattering, transmission and reflection at e=50-30,000 ev, z=1-92. *Atomic Data And Nuclear Data Tables*, 55(2):349–349, Nov 1993.

[96] B. L. Henke, J. Liesegang, and S. D. Smith. Soft-x-ray-induced secondary-electron emission from semiconductors and insulators: Models and measurements. *Physical Review B*, 19(6):3004–3021, MAR 1979.

[97] B.L. Henke, J.P. Knauer, and K Premaratne. The characterization of x-ray photo-cathodes in the 0.1-10 keV photon energy region. *Journal of Applied Physics*, 52(3):1509–1520, 1981.

[98] G.W. Fraser. The characterization of soft-x-ray photo-cathodes in the wavelength band 1-300 Angstroms Part 1: Lead glass, lithium-fluoride and magnesium fluoride. *Nuclear Instruments & Methods in Physics Research*, 206(1-2):251–263, 1983.

[99] G.W. Fraser, M.T. Pain, J.E. Lees, C.R. Binns, J.F. Pearsin, and P.R. Houghton. The characterization of gold x-ray photocathodes. *Nuclear Instruments & Methods In Physics Research Section A-Accelerators Spectrometers Detectors And Associated Equipment*, 321(1-2):385–391, SEP 15 1992.

[100] G.W. Fraser. The characterization of soft x-ray photo-cathodes in the wavelength band 1-300 Angstroms Part 2: Cesium iodide and other insulators of high photoelectric yield. *Nuclear Instruments & Methods In Physics Research*, 206(1-2):265–279, 1983.

[101] G.W. Fraser. The soft-x-ray quantum detection efficiency of microchannel plates. *Nuclear Instruments & Methods In Physics Research*, 195(3):523–538, 1982.

[102] D.G. Smith and K.A. Pounds. Soft x-ray photon detection and image dissection using channel multipliers. *IEEE Transaction of Nuclear Science*, NS15(3):541, 1968.

[103] E.H. Eberhardt. Gain model for microchannel plates. *Applied Optics*, 18(9):1418–1423, 1979.

[104] W.B. Feller. The dynodized microchannel plate model and secondary-electron emission. *IEEE Transactions on Electron Devices*, 32(11):2479–2481, 1985.

[105] M.A. Furman and M.T.F. Pivi. Probabilistic model for the simulation of secondary electron emission. *Physical Review Special Topics-Accelerators And Beams*, 5(12), DEC 2002.

[106] R.L. Bell. Noise figure of MCP image intensifier tube. *IEEE Transactions on Electron Devices*, 22(10):821–829, 1975.

[107] C. C. Kuranz, R. P. Drake, M. J. Grosskopf, H. F. Robey, B. A. Remington, J. F. Hansen, B. E. Blue, and J. Knauer. Image processing of radiographs in 3D Rayleigh-Taylor decelerating interface experiments. *ASTROPHYSICS AND SPACE SCIENCE*, 322(1-4):49–55, AUG 2009. 7th International Conference on High Energy Density Laboratory Astrophysics, St Louis, MO, APR 11-15, 2008.